Tampere University

PAULI MUSTALAHTI

Improving Automated Operations of Heavy-Duty Manipulators with Modular Model-Based Control Design

Tampere University Dissertations 772

Tampere University Dissertations 772

PAULI MUSTALAHTI

Improving Automated Operations of Heavy-Duty Manipulators with Modular Model-Based Control Design

ACADEMIC DISSERTATION
To be presented, with the permission of
the Faculty of Engineering and Natural Sciences
of Tampere University,
for public discussion in the auditorium K1702
of the Konetalo building, Korkeakoulunkatu 6, Tampere,
on 21 April 2023, at 12 o’clock.

ACADEMIC DISSERTATION
Tampere University, Faculty of Engineering and Natural Sciences
Finland

Responsible supervisor and Custos	Prof. Jouni Mattila Tampere University Finland	
Pre-examiners	Prof. Shahin Sirouspour McMaster University Canada	Prof. Radoslav Radulović University of Belgrade Serbia
Opponents	Prof. Radoslav Radulović University of Belgrade Serbia	Dr. Victor Barasuol Istituto Italiano di Tecnologia Italy

The originality of this thesis has been checked using the Turnitin OriginalityCheck service.

Cover design: Roihu Inc.

ISBN 978-952-03-2829-0 (print)
ISBN 978-952-03-2830-6 (pdf)
ISSN 2489-9860 (print)
ISSN 2490-0028 (pdf)
http://urn.fi/URN:ISBN:978-952-03-2830-6

HIILINEUTRAALI PAINOTUOTE
ClimateCalc CC-000025/FI
PunaMusta Printing

Carbon dioxide emissions from printing Tampere University dissertations have been compensated.

PunaMusta Oy – Yliopistopaino
Joensuu 2023

PREFACE

The study presented in this thesis was carried out from 2017 to 2022 within the Automation Technology and Mechanical Engineering Unit of Faculty of Engineering and Natural Sciences at Tampere University. I would thanks EUROfusion and the Faculty of Engineering and Natural Sciences for funding this thesis.

I would like to express deepest gratitude to my supervisor Prof. Jouni Mattila, for his encouragement and for providing the opportunity to work on this dissertation. I wish to thanks my preliminary examiners Prof. Shahin Sirouspour and Prof. Radoslav Ralulović for their constructive feedback.

I also wish thanks Dr. Janne Koivumäki, M.Sc. Petri Mäkinen, Dr. Santeri Lampinen, M.Sc. Lionel Hulttinen, and M.Sc Jyrki Tammisto good working atmosphere and many discussions over the years.

Finally, I wish to thanks my parents Hannu and Tarja, and my siblings Satu, Kati and Anni for their support throughout this process.

Pauli Mustalahti
Tampere, January 2023.

ABSTRACT

The rapid development of robotization and automation in mobile working machines aims to increase productivity and safety in many industrial sectors. In heavy-duty applications, hydraulically actuated manipulators are the common solution due to their large power-to-weight ratio. As hydraulic systems can exhibit nonlinear dynamic behavior, automated operations with closed-loop control become challenging. In industrial applications, the dexterity of operations for manipulators is ensured by providing interfaces to equip product variants with different tool attachments. By considering these domain-specific tool attachments for heavy-duty hydraulic manipulators (HHMs), the autonomous robotic operating development for all product variants might be a time-consuming process.

This thesis aims to develop a modular nonlinear model-based (NMB) control method for HHMs to enable systematic NMB model reuse and control system modularity across different HHM product variants with actuators and tool attachments. Equally importantly, the properties of NMB control are used to improve the high-performance control for multi degrees-of-freedom robotic HHMs, as rigorously stability-guaranteed control systems have been shown to provide superior performance. To achieve these objectives, four research problems (RPs) on HHM controls are addressed. The RPs are focused on damping control methods in underactuated tool attachments, compensating for static actuator nonlinearities, and, equally significantly, improving overall control performance. The fourth RP is introduced for hydraulic series elastic actuators (HSEAs) in HHM applications, which can be regarded as supplementing NMB control with the aim of improving force controllability.

Six publications are presented to investigate the RPs in this thesis. The control development focus was on modular NMB control design for HHMs equipped with different actuators and tool attachments consisting of passive and actuated joints. The designed control methods were demonstrated on a full-size HHM and a novel HSEA concept in a heavy-duty experimental setup. The results verified that modular control design for HHM systems can be used to decrease the modifications required to use the manipulator with different tool attachments and floating-base environments.

CONTENTS

List of Figures

ABBREVIATIONS

ARC	adaptive robust control
DH	Denavit-Hartenberg
DOF	degrees of freedom
HHM	heavy-duty hydraulic manipulator
HSEA	hydraulic series elastic actuator
IMU	inertial measurement unit
LWA	lightweight arm
MPC	model predictive control
NMB	nonlinear model-based
OEM	original equipment manufacturer
PBIC	position-based impedance controller
RP	research problem
SEA	series elastic actuator
TCP	tool center point
VDC	virtual decomposition control
VPF	virtual power flow

ORIGINAL PUBLICATIONS

Publication I	P. Mustalahti, J. Koivumäki, and J. Mattila, "Stability-Guaranteed Anti-Sway Controller Design for a Redundant Articulated Hydraulic Manipulator in the Vertical Plane," in *ASME/BATH 2017 Symposium on Fluid Power and Motion Control*, ASME, Oct. 2017. DOI: 10.1115/FPMC2017-4263.
Publication II	P. Mustalahti and J. Mattila, "Nonlinear Model-Based Controller Design for a Hydraulic Rack and Pinion Gear Actuator," in *BATH/ASME 2018 Symposium on Fluid Power and Motion Control*, ASME, Sep. 2018. DOI: 10.1115/FPMC2018-8841.
Publication III	P. Mustalahti and J. Mattila, "Cartesian Damping Controller with Nonlinear Control for a Floating-Base Hydraulic Manipulator," in *2022 Global Fluid Power Society PhD Symposium (GFPS)*, IEEE, Oct. 2022, Accepted.
Publication IV	P. Mustalahti and J. Mattila, "Nonlinear Model-Based Control Design for a Hydraulically Actuated Spherical Wrist," in *ASME/BATH 2019 Symposium on Fluid Power and Motion Control*, ASME, Oct. 2019. DOI: 10.1115/FPMC2019-1663.
Publication V	P. Mustalahti and J. Mattila, "Position-Based Impedance Control Design for a Hydraulically Actuated Series Elastic Actuator," *Energies*, vol. 15, no. 7, 2022, ISSN: 1996-1073. DOI: 10.3390/en15072503.
Publication VI	P. Mustalahti and J. Mattila, "Impedance Control of Hydraulic Series Elastic Actuator with a Model-Based Control Design," in *2020 IEEE/ASME International Conference on Ad-*

vanced Intelligent Mechatronics (AIM), IEEE, Jul. 2020. DOI: 10.1109/AIM43001.2020.9158817.

1 INTRODUCTION

Robotization is a rapidly growing trend in the heavy-duty mobile working machine industry [1]. While progress in autonomous car-like driving in heavy machinery has been swift [2], the automation process in their manipulators and tool attachments has been much slower. This is partly because wheeled vehicle drivelines have only a few major components, which enables high production volumes with dominant suppliers. However, working machine manipulators and tool attachments are much more domain specific, leading to a more heterogeneous set of devices with lower production volumes. Moreover, these manipulators are most often driven by hydraulic actuators that are known to be difficult to control with high performance [3].

Some commercial solutions for robot-assisted systems have recently been introduced in heavy-duty hydraulic manipulators (HHMs) in sectors like forestry [4], mining and construction [5], and material handling [6]. The aim of these solutions is to use closed-loop robotic control to lessen the work burden on human operators and improve productivity and safety. To further increase the automation level, human operators does not continuously need to make command decisions for the system. However, many of these semi-autonomous systems solutions remain at the conceptual research stage [2]. The difficulties in achieving high performance control in these heterogeneous systems have undermined the automation process.

The main focus of this thesis is to improve the modularity of robotic control design methods and provide more systematic methods to handle different HHM variants with their different types of actuators and tool attachments. Moreover, the state-of-the-art robotic control methods in [7], [8] were developed for stationary base robotics and, therefore, need to be extended to mobile manipulator applications by introducing floating-base manipulator control modules.

1.1 Motivation

In industrial applications, many different types of manipulators are used, such as articulated HHMs, overhead gantry cranes, and tower cranes for moving heavy loads. Many of them have in common the feature that humans often work in the same area as these manipulators. Traditionally, a human operator controls manipulators in an open loop with visual feedback. Therefore, skilled human operators are needed [9] to ensure the required system productability. Robot-assisted system development has received significant interest for offering the possibility of decreasing demand for human operator skill levels and work burdens and achieving less deviation in HHM productivity and safety.

For original equipment manufacturers (OEMs) in HHM applications, a typical product portfolio consists of a large number of product variants. Therefore, developing high-performance robotized solutions with closed-loop control for these variants can be very time-consuming. These large product portfolios require systematic model-based design methods that enable control model reusability; modular connectivity with the existing software modules in the overall robot control system is also needed. As to HHMs in industrial applications relevant to Finland (see Figure 1.1), many commercial manipulators have a similar articulated link structure with a base rotation followed by 2 or 3 degrees of freedom (DOF) anthropomorphic arms [10]. A typical OEM product portfolio consists of a set of manipulator structures that differ only in their load capacity and arm length. However, differences come from the various tool attachments that usually consist of active or passive joints.

It is typical in lifting applications to use HHMs where the material handling or load-grasping tool introduces additional DOFs into the system. For example, a load-grasping tool typically consist of an additional grasping tool with rotation and yaw functions. However, in HHMs, unlike in industrial robotics, a set of passive joints is often employed between the manipulator arm tip and the load-grasping tool to reduce contact forces. Therefore, in robotized solutions these passive joints result in an underactuated robotics system that needs control methods to handle load-grasping tool swaying in free space motions.

It is known that commercial 6-DOF HHMs are quite rare. However, a few OEMs have had 5-DOF HHMs on the market over 30 years, such as underground tunnel drilling manipulators [2] and surface drilling machines used in open mines

[11]. In addition, construction sites often require HHMs with long-reach arms for concrete spraying applications [12], [13]. Moreover, there are significant production volumes of earth-moving excavators equipped with a so-called rototilt attachment that enables bucket tilt and rotation motions, making them fully 6-DOF HHMs.

In HHM robotic-type wrist mechanisms, a 360° range of motion is most often desirable, whereas the last tool center point (TCP) actuator often needs continuous rotation like an excavator rototilt mechanism. The two most common commercially available hydraulic rotational actuators providing wide ranges of motion are helical gear actuators and vane actuators. However, vane actuators are not commonly used in HHMs, as their internal leakage can result in low-velocity joint motion drift in the safe stop state. Helical gear actuators are operated by hydraulic cylinders pushing the gears that results in nearly 360° motion; hydraulic cylinder sealing is used to ensure the safe stop state.

Hydraulic rack and pinion actuators are quite widely used in HHM base rotation joints. They can be designed to provide a range of motion of over 360°. Their drawback, however, is their relatively large volumetric size. Both helical gear and hydraulic rack and pinion actuators are subject to gear backslash, which limits their control performance. In HHMs, this manipulator base joint is most often mounted on a non-stationary base platform such as a rough-terrain vehicle. In the robotics terms, this is called a robot on a floating-base platform that with up to 6-DOF base motions. Therefore, the manipulator's floating-base movements lead to an underactuated robotic system that is more complex to stabilize. The current state-of-the-art researches has mainly focused on stationary-base HHM controls, with the study of modular control systems for floating-base robots largely absent from the literature [7].

An interesting actuator alternative called a series elastic actuator (SEA) is widely used in human-robot interaction robotics, where it can provide high force fidelity. HHMs would also benefit from actuators with lower controllable impedance. However, in HHM applications, SEAs have not been studied widely, even though they have the interesting feature of built-in force feedback position-based estimation. Using force sensors for HHM applications is problematic as they are susceptible to shock loads and overloading, in addition to being an expensive component at high loads.

In robotic control system design, nonlinear model-based (NMB) control methods have become widely used [3] in the past decade. In terms of control design for HHMs, the higher number of DOFs leads to more complex behavior in their kinematics and dynamics. Combined with the highly nonlinear dynamics behavior of hydraulic systems, this makes high-performance control design a very challenging task.

In [14] have listed more than 30 different road-rail excavator mountable tool attachments for railway works such as track lifting jacks, compactors, and piling hammers. This is but one example of the diverse set of actively controlled robot wrist-like mechanisms used in HHMs tool attachments. Thus, for the more robotic HHM applications of the future, such as road-rail excavators, the need for a modular robotic control system framework is evident.

Figure 1.1 Heavy-duty manipulators in the construction, forestry, and mining industries.

1.2 Research Problems

The main focus of this thesis is on robotic NMB control design to enable model reusability and modularity by incorporating new modeling methods to enhance state-of-the-art control designs [7], [8] toward the achievement of real-world floating-base

6-DOF HHM robotic solutions. The research problems (RPs) address the modular control problems of floating-base HHM arms with their robotic wrist-type structures, including actuation dynamics with nonlinear hydraulic actuators and passive joints. The main target is the reuse of developed control modules as building blocks when composing new NMB robotic controllers for manipulator arms and their various robotic tool attachments, including both passive or actuated joints. Rigorous stability-guaranteed NMB robotic controls have been shown to support high-performance control [3].

RP-I Modular Nonlinear Control Design: Can subsystem-based design methods improve control system modularity in commercial heavy-duty hydraulic manipulators with different product variants?

RP-II Hydraulic Actuators with High Gear Ratios and Static Input Nonlinearities: Can nonlinear control design methods be used to provide modular high-performance control for hydraulic actuators with high gear ratios and static input nonlinearities?

RP-III Underactuated System with Anti-Sway and Damping Control Methods: Can model-based control methods improve underactuated heavy-duty system control?

RP-IV Hydraulic Series Elastic Actuators: Can series elastic actuators provide high force fidelity in heavy-duty hydraulic manipulators with enhanced contact force estimation?

These RPs are discussed in the publications. **RP-I** is addressed in P-I–P-IV, where the state-of-the-art NMB control equations for 2-DOF HHMs in [7] were used as a baseline for extension to both 3-DOF and 6-DOF HHMs. **RP-II** is discussed in publications P-II and P-IV, where the control performance of actuators with high gear ratios and static input nonlinearities improved with NMB control methods. **RP-III** is examined in publications P-I and P-III for improving NMB controllability in underactuated HHMs. **RP-IV** is discussed in publications P-V–P-VI, where hydraulic series elastic actuators (HSEAs) for HHM applications are proposed.

1.3 Requirements and Scope of the Research

The focus of this thesis is to study modular NMB control design methods for HHMs. The proposed control design method has been used to decrease the modifications required for existing and new control design with a variety of tool attachments and actuators. The aim of modular control design is to extend the reusability of the designed controllers so that system modeling and control equations for any new parts required by the system need only be designed once. At the same time, modular control enables minimizing the modifications required to control equations between different product variants by providing modular systematic methods to handle them. The focus is to study HHMs with their tool attachments and actuators.

In this thesis, a modular control design is demonstrated with a full-size commercial HHM. The manipulator arm structure is common in many industrial applications (see Figure 1.1). The experimental setup shown in Figure 1.2 consists of equipment in indoor laboratory conditions. Compared to many commercial HHMs, the test manipulator is controlled with high-bandwidth proportional valves. In laboratory conditions, the test environment is equipped with highly accurate joint sensors and pressure sensors, which are required measurements for implementation of NMB controller. Further, the reference sensors for some nonlinearities were added to verify the proposed control methods. The designed control methods are defined so that required sensor implementations are minimized.

In addition, the required sensors are selected so that the proposed solutions can be implemented and reused with robust commercial solutions for HHMs. The modular control design is evaluated with a Hiab 033 XS manipulator arm in a laboratory at Tampere University with a 3-DOF wrist composed of three helical gear actuators; the manipulator's horizontal reach is 3.6 m.

1.4 Thesis Contributions

As a compendium thesis, the main contributions of this research are closely related to its associated publications. The scientific contributions of the individual publications are as follows:

P-I This publication proposes a method to design a modular control for an HHM

Figure 1.2 Hiab 033 XS manipulator in laboratory of Tampere University.

with a load-grasping tool attachment subject to oscillations; its main contribution is the introduction of a modular NMB control design for underactuated HHMs, using the virtual decomposition control (VDC) approach as a framework and incorporating these equations into previously designed control equations for HHM arm. The properties of NMB control design are used to propose an anti-sway damping control method for an HHMs equipped with tool attachment that consist of passive joints. As a novelty, a stability-guaranteed NMB controller for the anti-sway damping control for HHM is presented.

P-II This publication studies an HHM with a rotating base; its main contribution is to propose a modular NMB control design for a hydraulic rack and pinion actuator. As a second novel contribution, it presents the stability-guaranteed adaptive backlash compensation methods that are incorporated into the NMB control design. The proposed compensation methods provide a solution to compensate for the static effects of backlash input nonlinearity. As an outcome of this publication, the overall control performance of 3-DOF HHMs is improved by providing NMB control design for a rotating base actuator.

P-III This publication presents an HHM with a floating-base platform; its main contribution is the introduction of control methods to compensate for floating-base movements in Cartesian space robotic control of HHMs. It provides a solution to compensate for the platform movements in Cartesian space control. As an outcome, this publication enabled the investigation of a robotic control for HHMs on mobile platforms such as rough-terrain vehicles.

P-IV This publication proposes a 3-DOF HHM arm equipped with a 3-DOF hydraulically actuated wrist configuration to construct a 6-DOF HHM; its main contribution is the introduction of a modular NMB control design in the context of a 3-DOF hydraulically actuated helical gear actuator. This publication also builds on P-II by investigating the proposed backlash compensation for a multi-DOF serial gear mechanism. As an outcome this publication enables an NMB control design for a 6-DOF HHM.

P-V This publication presents a HSEA for HHM applications; its main contribution is to introduce a novel linear full state feedback controller for a fifth-order actuator system. Second, it offers an impedance control design for HSEAs to enable contact space motion for these actuators. This publication provides preliminary results for a control design for HSEAs.

P-VI This publication extends the control design in P-V by presenting a novel modular NMB control design for HSEAs. This design is incorporated into an impedance control design that enables contact space motion for HSEAs. This publication provides the NMB control methods for HSEAs in HHM applications.

1.5 The Author's Contribution to the Publications

This section clarifies the author's contribution to each publication presented in this thesis.

P-I The author wrote the publication, developed the approach to handle control of a passive joint within the NMB control design of the VDC, and implemented the control system on the experimental setup. Dr. Janne Koivumäki helped with the mathematical derivations and aided in writing the publication. Professor Jouni Mattila, the author's academic supervisor, reviewed the publication and suggested improvements.

P-II The author wrote the publication and developed the control methods for the hydraulic rack and pinion actuator. The author also extended the NMB control design for backlash compensation; Professor Jouni Mattila reviewed the publication and proposed improvements.

P-III The author wrote the publication and developed a control method for HHMs on floating bases. The author also developed the simulation model for a 3-DOF manipulator on a floating base. Professor Jouni Mattila reviewed the publication and suggested improvements.

P-IV The author wrote the publication and developed the modular controller for a 3-DOF hydraulically actuated wrist configuration integrated with an existing 3-DOF HHM. Professor Jouni Mattila reviewed the publication and proposed improvements.

P-V The author wrote the publication and developed the linear full-state feedback controller and position-based impedance controller (PBIC) for a fifth-order HSEA system. Professor Jouni Mattila reviewed the publication and proposed improvements.

P-VI The author wrote the publication and developed the NMB control equations for the HSEA system. Professor Jouni Mattila reviewed the publication and suggested improvements.

1.6 Outline of the Thesis

This thesis is presented in six chapters. In this chapter, the topic and RPs of the thesis are introduced. In Chapter 2, the state-of-the-art related to NMB control design, backlash compensation, anti-sway compensation, and HSEAs are introduced. The proposed control design methods for HHMs with their actuators and a set of tool attachments are presented in Chapter 3. Chapter 4 discusses the RPs and how they are addressed. The conclusions of the overall thesis are provided in Chapter 5. Finally, the publications included in the thesis are summarized in Chapter 6. An outline of this thesis and the six publications is presented in Figure 1.3.

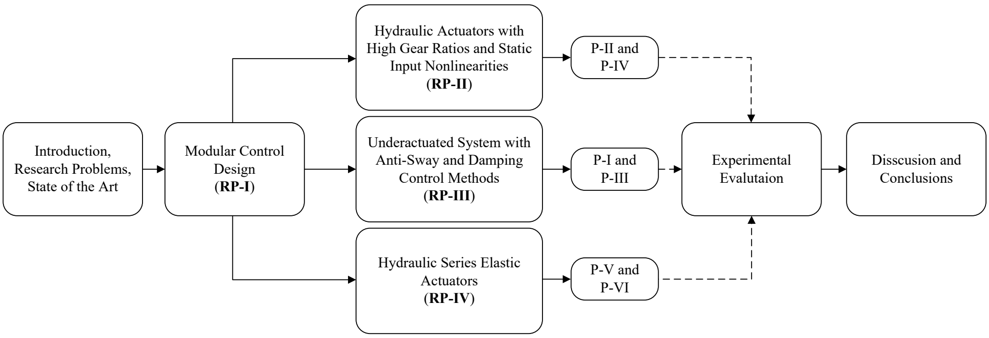

Figure 1.3 Outline of the thesis.

2 STATE OF THE ART

This thesis focuses on studying articulated HHMs that are used in industrial applications to provide high power-to-weight ratio, robustness, and low-cost components. However, due to highly nonlinear dynamics behavior, the high-performance control of these manipulators requires accurate modeling, measurements, and stability-guaranteed control for the entire system [3]. In this chapter, the state-of-the art solutions in the field of this thesis are reviewed. First, the solutions to improve the overall control performance of HHMs are reviewed. Second, the solutions to handle a common nonlinearities in HHMs are introduced. Third, the solutions to improve control performance of HHMs equipped with varying tool attachments are reviewed. Finally, the state-of-the-art for HSEAs in heavy-duty applications are reviewed.

2.1 High-Performance Control of Articulated Heavy-Duty Manipulators

In hydraulic systems, the linear output force of a cylinder or output torque of a rotary actuator is controlled by electro-hydraulic valves that control the hydraulic oil flow rate into actuator chambers. However, the highly nonlinear dynamics behavior of a hydraulic system makes designing a high-performance closed-loop control design for these systems challenging [15]. The major discontinuous and non-smooth nonlinearities in hydraulic systems are actuator friction, hysteresis, backlash, directional change of valve opening, valve input saturation, and valve dead-zone. Due to the nature of these nonlinearities, an accurate modeling for hydraulic systems must take into account many uncertain model parameters. In multi-DOF HHMs, high inertial loads and nonlinear system behavior combine to limit the control performance of the system. Linear control methods may lead to inaccurate control performance because of the system's nonlinearities [16].

NMB control methods for electro-hydraulic servo systems have been an active research area in recent decades [3]. A summary of the control methods for series HHMs in free space reviews indicates that the highest performance control for manipulators has been achieved with stability-guaranteed NMB control approaches. NMB methods usually provide parameter adaptation for uncertain model parameters, which improves control performance. Most widely used NMB method is backstepping [17], which provides methods to design nonlinear adaptive control with stability analysis. Adaptive robust control (ARC) for HHMs was presented in [18], while model predictive control (MPC) methods for HHMs were presented in [19], [20]. The VDC approach was originally presented in [21], and its capabilities in the context of hydraulic systems have been extensively verified [7], [22], [23]. In this NMB control method, the dynamics model of the entire system is used to provide a feedforward term to the control design to increase control performance. In addition, the energy efficiency of HHMs can be improved with high-performance control design and a separate meter-in and separate meter-out control valve setup [24].

In many books [10], [25], the dynamics modeling for the robotic systems is implemented using Lagrangian dynamics. However, as discussed in [26], these methods lead to complex modeling equations when the number of DOFs of robotic systems increases. Most proposed NMB methods are based on Lagrangian dynamics. As proposed in [27], the decentralized control of a multi-DOF requires that the entire system can be split into subsystems. Lagrangian dynamics-based decentralized control methods for robotic manipulators have been proposed by several authors [28]–[30]. The VDC approach is based on a Newton-Euler dynamics modeling that enables the model dynamics of the entire system to be a combination of subsystem dynamics. A decentralized observer for complex robotic systems was presented in [31], while an observer design for backstepping was proposed in [17] .

In industrial applications, HHMs are subject to contact space motion with the environment. Therefore, force control is necessary to handle contact space motion between the environment and the manipulator. Achieving force control for HHMs is challenging task in the context of the rigorous modeling requirements for the manipulator used. Most of the proposed force controllers for HHMs are based on impedance control methods. For example, an impedance controller for an excavator was proposed in [32]. Stability-guaranteed impedance control methods for HHMs using the VDC approach were presented in [8]. A hybrid position and force control were proposed in [33] and [34] for HHMs in subsea applications and for an HHM with a stationary base.

2.2 High Gear Ratios and Static Input Nonlinearities in Hydraulic Actuators

Typical HHMs (see Figure 1.1) can achieve an arbitrary position, whereas a 3-DOF arm with a 3-DOF wrist achieves both an arbitrary position and the orientation of the manipulator TCP in Cartesian space. Therefore, by equipping an HHM arm with an additional 3-DOF wrist configuration, the dexterity of the working envelope of the manipulator can be increased. However, 6-DOF HHMs are quite rare, and commercial multi-DOF HHMs are most often equipped with non-spherical wrist structures. This distinguishes them from industrial robots with spherical wrists. In robotics, the wrist often requires an actuator with a 360° range of motion. In addition, the hydraulically actuated wrist needs a compact volumetric size [35]. Three main rotary actuators are used in hydraulic systems. The first choice, the hydraulic rack and pinion actuator, is used to provide over 360° rotation movement in the manipulator base joint. However, the volumetric size of this actuator is relatively large, although the actuators are fairly inexpensive. The second choice, vane actuators, offer compact actuator size [36]. However, there is uncontrollable movement that leads to the lack of a safe stop state. The third choice, hydraulically actuated helical gear, also offers compact actuator size, but both helical gear and hydraulic rack and pinion actuators have high-speed gears that are subject to high frictions and gear backlash.

One of the most common non-smooth nonlinearities in mechanical gears is backlash, which describes the clearance of adjacent moving parts. This nonlinearity is typical of motor gears. With a closed-loop control design, backlash is one of the most common nonlinearities limiting control performance. The modeling and compensation methods for this common nonlinearity have been an active research area for decades [37]. As reviewed in [38], most of the proposed methods are implemented by using inverse model methods to compensate for the effects of backlash. Due to the nature of backlash, however, the model parameters are often uncertain. Therefore, adaptive inverse models have been used to compensate for the effects of backlash nonlinearity with limited initial conditions in [37], [39], [40]. Backlash compensation in feedback control systems by using a neural network [41] or fuzzy logic [42] has been proposed. The linearly parameterized adaptive backlash compensation incorporated into ARC [43] was proposed to ensure bounded adaptive compensation methods. An adaptive backlash incorporated with a nonlinear backstepping control design was proposed in [44].

High levels of gear friction requires an extremely accurate friction model for helical gear actuators to estimate actuator force. Adaptive friction models are commonly used to improve force control performance and improve the feedforward term in VDC. Friction models with parameter adaptation can be incorporated into model-based control, as has been demonstrated for the VDC approach [22], for ARC [45], and for backstepping control design [46].

In state-of-the-art industrial applications, hydraulic actuators are controlled with proportional valves with slow dynamics and valve overlap [47]; these valves are suitable for manual human operations. The valve overlaps are needed to ensure the safe stop state of the manipulator. However, for computer-controlled robotized solutions, a dead-zone inverse control proposed in [48] can be used for mobile hydraulic valves. As demonstrated with the VDC approach [47] and with ARC [49], adaptive dead-zone compensation can significantly improve the control performance of HHMs controlled by valves with high dead-zones.

2.3 Damping Control Methods for Underactuated Manipulators

Many commercial manipulator tool attachments use passive joints to increase task dexterity and high torque. Load anti-sway control methods for overhead cranes and articulated manipulators have been subject to research in recent decades. The payload anti-sway compensation used in overhead and rotary cranes is often implemented through an open-loop control called input command shaping [50]–[53]. In this control design, the operator control commands for the crane are filtered to minimize components, which leads to load oscillation. Closed-loop anti-sway control designs have been used to improve control performance and the robustness of anti-sway control for handling load disturbances in a closed-loop controller. As demonstrated in [54], the robustness of the input shaping method was improved by using optimization methods for a feedforward controller. Similarly, in [55], a disturbance observer with state feedback control was used to handle external disturbances for rotary cranes. In addition, anti-sway control for rotary cranes with fast crane dynamics but slower load dynamics was used to improve the control performance through a cascade control structure [56].

Nonlinear control methods can be used to improve control performance, as presented in [19] with MPC for rotary cranes. Using the crane and load dynamics of a linearized model-based feedforward control and linear quadratic regulator methods to improve anti-sway control for articulated HHMs was proposed in [57], [58]. Given the complex dynamics modeling of crane systems, an adaptive sliding mode control was used to handle uncertain dynamics modeling parameters for tower cranes in [59].

Most of the closed-loop anti-sway control methods were tested only through simulation results or with laboratory-scale manipulators. Successfully implemented anti-sway control systems with real industrial HHMs have been presented in only a few studies [20], [60]–[62]. In these studies, experimental verification with a large harbor manipulator was presented in [60] for linearized feedforward anti-sway control, while in [61], a 3-DOF HHM was used with a state feedback control design. Anti-sway control methods based on linearization control methods were proposed in [20], [62]. In [62], a flatness-based feedforward control for tower cranes was proposed to compensate for the effects of load motions and external disturbances. A nonlinear anti-sway control design for HHMs based on nonlinear MPC was presented in [20]. However, the multi-body dynamics and nonlinearities characteristic of hydraulic actuators have been neglected in previous research.

In implemented closed-loop anti-sway solutions, accurate estimates for unactuated joint angles and angular velocities or for load free space motions in all directions are required to stabilize the load. However, due to harsh outdoor conditions, accurately estimating these motions is challenging. Typically, incremental encoders or potentiometers are used to measure load motions. In addition, inertial measurement unit (IMU) sensors have been used to estimate passive joint motions during free space motions [61], [63], [64]. In [61] and [64], IMU sensors were used to estimate motion in suspended loads for closed-loop control. Further, in [63], a rotary gyroscope was used to estimate the 3-DOF motions of a passive load-grasping tool.

In many industrial applications, HHMs and tower cranes are placed on a stationary base during operations. However, in cases like marine operations and mobile robotic applications, the manipulator is mounted on a moving platform such as a rough-terrain vehicle. In moving platform applications, the entire system is also often underactuated due to the unactuated floating-base movements of the platform. Due to the strong coupling between the manipulator and the moving platform, developing closed-loop control of these robotic systems is difficult [65]. In view of the closed-loop control operations for floating-base manipulators, platform movements need to be compensated for by controlling the manipulator tip. As demonstrated in [59], [66], [67] for offshore cranes, model-based control methods can be used to damp floating-based movements of the TCP.

2.4 Hydraulic Series Elastic Actuators

SEAs have been widely used in industrial robotics to improve robot motion and force controllability in tasks requiring contact force compliance [68]. In lightweight arm (LWA) robots like the KUKA LBR [69] and the Franka robot arms [70], SEAs are used to increase safety and controllability in contexts with uncertain contact space motions. Compared to traditional robot actuators, SEAs can improve the system's high force fidelity, force sensing, and shock tolerance by adding a spring between the environment and the power output shaft of the actuator [71].

In torque-controlled electric robotic applications [72]–[75], SEAs are widely used. Electric SEAs have been used to provide rapid movement with low load mass in, for example, humanoid robots [76], walking robots [77], and teleoperation [78]. In LWA robotic applications, electric actuators limit the maximum payload for the robotic arm. Therefore, HSEAs were used to provide higher power-to-weight ratios for these applications and thus increase maximum system payload. HSEAs for lightweight robotic applications have been investigated by several authors [79]–[81]. Further, due to the nonlinear dynamic behavior of hydraulic systems, achieving a high-performance control design for an entire system is challenging.

In commercial HHMs, the required actuator output force is greater than in LWA applications. Control methods for HSEAs with higher payloads were investigated in [82]–[84], where the performance analyses and simulation results for HSEAs with payloads of approximately 20 kg were presented. An experimental verification for control of an HSEA with a 20 kg payload was presented in [85]. However, the required maximum payload for hydraulic actuators is much higher in full-sized HHMs.

As to control design for torque-controlled electric SEAs, the force control of these actuators has been an active research topic; impedance control is used to handle the uncertain contact force between the environment and the actuator. As presented in [86], a cascade control structure is a common approach to achieving impedance control in SEAs. This structure isolates the slower contact dynamics from the faster actuator dynamics by using the actuator controller as an inner-loop controller for outer-loop contact space motion control. In LWA robotic systems, impedance control for SEAs was implemented by applying a disturbance observer control design to the spring deflection feedback control [87]. SEAs control stability in different environments was analyzed in [88], and control design for a linear electric actuator was investigated in [89], where high motor voltage with a drivetrain was used to produce continuous actuator force.

A control design for linear HSEAs is presented in [83], [84], [90]. In these studies, a force-controllable HSEA was modeled as a linear second-order system that consists of a first-order time constant and an integrator. Thus, the nonlinear fluid dynamics are neglected. Due to the variable stiffness of the fluid and the inherent system dynamics, the entire HSEA system leads to a fifth-order model. In [83], [84], a disturbance observer was used to enable impedance control in these actuators. As presented in [10], the outer-loop controller was implemented using a cylinder position error to estimated the contact force between the environment and the cylinder. Due to the fast dynamics of the spring and the slower hydraulic system dynamics, a control system with a fast inner-loop controller and a slower outer-level controller is required to improve control of the HSEA [91].

3 PROPOSED SOLUTIONS

This chapter reviews the proposed solutions in the publications from the perspective of solving the RPs. While the solutions for each RP are discussed individually, the integration of these solutions in the robotic control of HHMs is the overarching theme.

3.1 Modular Nonlinear Model-Based Control Design

As Chapter 2 shows, the productivity of HHMs can be increased by improving the automation level of these systems. To achieve the requirements for system performance, a high-performance control is required. Attaining a high-performance robotic closed-loop control design for multi-DOF HHMs is challenging due to the highly nonlinear behavior of hydraulic systems. Typically, these nonlinearities (e.g., actuator frictions, backlash, and hysteresis) lead to many uncertain model parameters. Therefore, a full dynamics modeling process in NMB control design can lead to complex mathematical presentations for multi-DOF systems.

In industrial applications, the dexterity of HHMs is ensured by providing an interface to equip the manipulator arm with different tool attachments and actuators. Tool attachments, like robotic wrist-like mechanisms that consist of either active or passive joints, are connected to the HHM arm tip and the required tool attachment may also emerge during daily operations. Typically, tool attachment dynamics significantly affect the entire system dynamics. Redesigning the control equations for an entire system separately for every tool attachment variant can be time-consuming. Due to the different dynamics properties of the system variants, designing a universal solution for high-performance control of a manipulator is challenging.

In this thesis, an NMB control is designed by using the VDC approach as a framework to cover control design for multi-DOF HHMs with a variety of tool attachments, actuators, and floating-base conditions. A considerable advantage of the

VDC approach is that it provides modularity for control design. For instance, it is possible to replace subsystems or add new subsystems to the original system without changing the control equations or control tuning of existing subsystems. Therefore, the complexity of the NMB control can be greatly deceased for 6-DOF HHM. A modular control design minimizes the changes required in control design when a new tool attachment is connected to the manipulator and enables bringing an NMB control closer to commercial industrial applications by providing systematic methods to divide the entire system into functional subsystems, such as a 3-DOF HHM arm with different tool attachments. The modular control design also enables modifying tool attachment subsystems without any modifications to previously designed 2-DOF HHM arm subsystems. The principle of a modular subsystem model-based control is illustrated in Figure 3.1; its application to a typical HHM is shown in Figure 1.1. In Figure 3.1, the entire system is decomposed into subsystems by adding the virtual cutting points between each subsystems.

In the VDC approach, the dynamic interaction between two subsystems can be presented in scalar terms; namely, the virtual power flow (VPF). As defined in [26], the VPF in a fixed coordinate frame can be written as

$$p_{\mathbf{A}} = ({}^{\mathbf{A}}V_{\mathrm{r}} - {}^{\mathbf{A}}V)^T({}^{\mathbf{A}}F_{\mathrm{r}} - {}^{\mathbf{A}}F), \tag{3.1}$$

where $p_{\mathbf{A}}$ is the VPF term, and ${}^{\mathbf{A}}V_{\mathrm{r}} \in \mathbb{R}^6$ and ${}^{\mathbf{A}}F_{\mathrm{r}} \in \mathbb{R}^6$ represent the required vectors of ${}^{\mathbf{A}}V \in \mathbb{R}^6$ and ${}^{\mathbf{A}}F \in \mathbb{R}^6$, respectively. So, the VPF describes the inner product of the linear/angular velocity vector error and the force/moment vector error in a fixed coordinate frame. In the VDC approach, the rigorous stability analysis of the entire system can also be guaranteed locally, at the subsystem level. In this analysis, VPFs are stability connectors between the subsystems [26]. The rigorous stability analysis for the entire system is guaranteed by defining a negative VPF and its corresponding positive VPF to successive subsystems; they should cancel each other out.

In P-I and P-IV, the effectiveness of the proposed modular control design is presented with two different tool attachments. In each attachment studied, the modular control equations are connected to previously designed control equations for 2-DOF HHMs taken from a state-of-the-art paper [7]. As P-I and P-IV propose, the control design for these tool attachments requires only dynamics modeling for the subsystems studied. The Newton-Euler dynamics for these modular subsystems are presented in detail in P-I and P-IV. In the modular control design, each actuator can

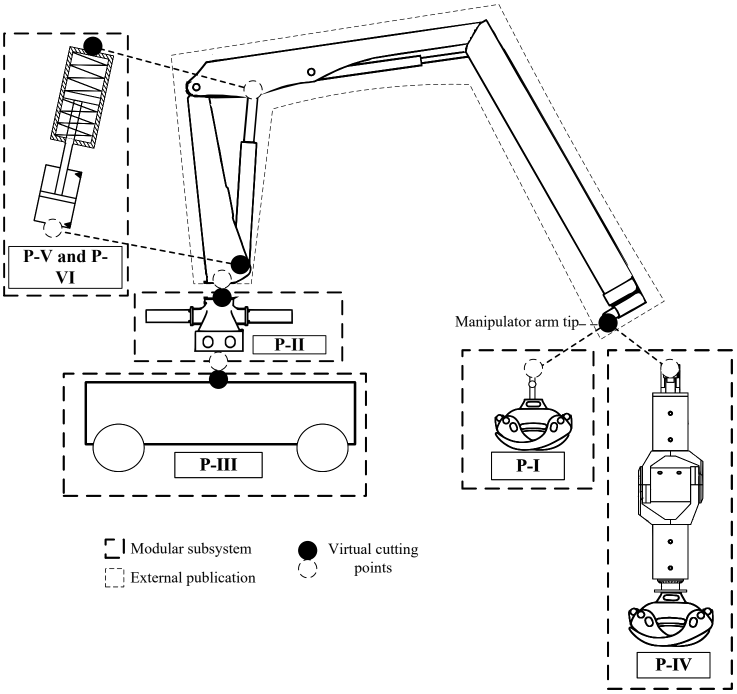

Figure 3.1 Modular control design for a multi degrees of freedom manipulator.

be decomposed into its own subsystem, and rigorous stability analysis for each subsystem is present locally, at each subsystem level. In P-II and P-VI, control equations for hydraulic rack and pinion actuators and HSEAs are proposed respectively.

In many industrial applications, like those in the forestry and mining industries, the working envelope is extended by placing manipulators on top of moving platforms called mobile manipulators that typically operate in rough-terrain conditions. Due to these conditions, the manipulator base is not stationary, which means that 6-DOF floating-base motions are possible for the manipulator base. As P-III shows, the mobile platform can be handled in its own subsystem that can be added to the VDC design with the required number of DOFs. In P-III, an NMB control design process for a multi-DOF HHM with a floating base is proposed. The modular control design enables extending NMB control for these manipulators without requiring any modifications to the control equations of the HHM at the top of the platform.

By dividing the entire system into modular subsystems as shown in Figure 3.1, the NMB control design can be brought closer to real-world industrial applications by decreasing the complexity of the NMB control design process. As the multi-DOF HHM in Figure 3.1 shows, modular subsystems enable handling NMB design in functional subsystems. This modularity also enables modifications to previously designed equations without the need to change the control equations of previously designed subsystems. Thus, the proposed method enables handling the control design for 6-DOF HHMs as a plug-and-play subsystem because the control design allows for the reuse of model connectivity between subsystems and improves the control design for the HHM portfolio with different tool attachments. The stability analysis for different product variants can be demonstrated.

3.2 Anti-Sway and Damping Control Methods for Articulated Heavy-Duty Manipulators

Underactuated manipulators are common in industrial applications, as discussed in Chapter 2. A system's underactuation follows from the fact that not all system joints are directly controllable because some are passive joints. Hence, the number of controllable DOFs is lower than the total number of DOFs in Cartesian space. In view of robotic control, it is typical for the desired motions for the TCP to be designed.

It is common in industrial areas for the working environment to change during operations, and rough-terrain conditions are typical. A rigid manipulator is mounted on a mobile platform to increase the machine's working environment. In these applications, the rough-terrain conditions lead to floating-base movements for a rigid manipulator base frame. Similarly, in offshore applications, sea conditions cause floating-base movements in the manipulator base. When considering manipulator operation in these conditions, the entire system is underactuated due to unactuated platform movements that may cause oscillation in manipulator tip motions during operations.

On the other hand, it is typical for HHM lifting tool attachments to include passive joints to enable both horizontal and vertical tool movements. In construction sites, for example, commercial HHMs are often equipped with a rotating load-grasping tool that is connected to the manipulator arm tip with a pair of passive revolution joints that are subject to sway motions during operation due to acceleration of the HHM arm tip.

For fluid and safe operations of these HHMs, skilled human operators are needed. As discussed in Chapter 2, the human operator work burden can be decreased and operational safety improved by increasing the level of automation. Today, a commercial robotic function that assists solutions for HHMs enables the direct control of the HHM arm tip, replacing the traditional joystick control for joints. However, these solutions do not yet address damping control for these passive joint configurations.

In P-I and P-III, two cases with underactuated manipulators are studied. In P-III, a Cartesian damping control for a floating-base manipulator is proposed, using the VDC approach as a framework, while an anti-sway damping control design for a load-grasping tool with passive joints is studied in P-I.

3.2.1 Cartesian Space Damping Control for Floating-Base Manipulator

In the context of Cartesian space control for HHMs, a floating manipulator base directly affects TCP movements. The common structure for a mobile manipulator is composed of an HHM mounted rigidly on top of a moving platform, as illustrated in Figure 3.2, where the TCP is located on the HHM arm tip. In Cartesian space control design, the TCP movements are designed by using the manipulator base frame as a reference. However, due to the floating base, the fixed inertial frame needs to be defined as a reference frame for the control design. The underactuated nature of the system means that the desired reference velocities for TCP position and velocity can be defined as a reference, but the velocities for floating-base linear or angular velocities are directly controllable.

In robotics, a common method to define a manipulator's forward kinematics is to use Denavit-Hartenberg (DH) parameters to define the transformation between successive coordinate frames [10]. The fixed coordinate frames used to describe manipulator kinematics are presented in Figure 3.2, and the corresponding DH parameters for a 3-DOF HHM are presented in Table 3.1. In the VDC approach, these coordinate frames can be used to model the manipulator's kinematics and dynamics. In view of the VDC, the force/moment transformation between two fixed coordinate frames can be defined by using the transformation matrix ${}^{\mathbf{A}}\mathbf{U}_{\mathbf{B}} \in \mathbb{R}^{6\times 6}$ [26]. Now, by using the DH parameters to define the transformation between two coordinate frames, the linear/angular velocity vector in each coordinate frame can be defined. Therefore, the forward differential kinematics for the manipulator in Figure 3.2 can be written as

$$\mathbf{J}_q = \begin{bmatrix} {}^{\mathbf{B}_0}\mathbf{U}_{\mathbf{B}_3}^T\mathbf{z} & {}^{\mathbf{B}_1}\mathbf{U}_{\mathbf{B}_3}^T\mathbf{z} & {}^{\mathbf{B}_2}\mathbf{U}_{\mathbf{B}_3}^T\mathbf{z} \end{bmatrix}, \tag{3.2}$$

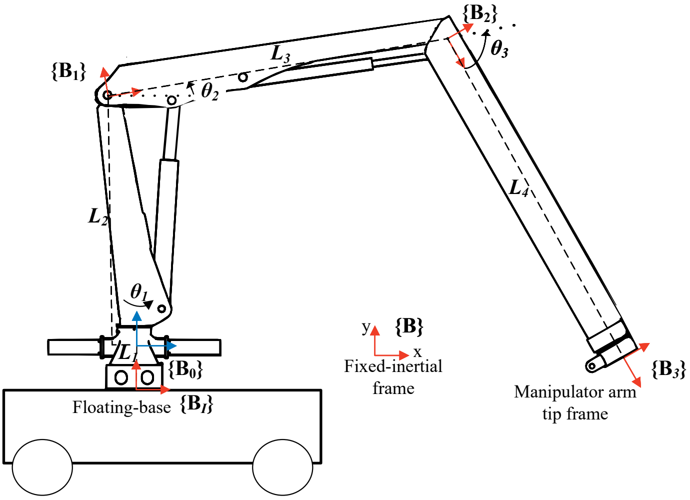

Figure 3.2 Heavy-duty manipulator with floating base.

Table 3.1 Denavit-Hartenberg parameters for a heavy-duty hydraulic manipulator.

a	d	α	θ
0	L_0	$-\pi/2$	0
L_1	L_2	$\pi/2$	θ_1
L_3	0	0	θ_2
L_4	0	0	θ_3

where $\mathbf{z} = [0\ 0\ 0\ 0\ 0\ 1]^T$, and $\mathbf{J}_q \in \mathbb{R}^{6\times3}$ is the Jacobian matrix for the manipulator. Further, by considering the floating-base movements of the manipulator base frame $\{\mathbf{B}_I\}$, the forward kinematics for the entire system can be defined in matrix form as

$$\begin{bmatrix} {}^{\mathbf{B}_3}V \\ {}^{\mathbf{B}_I}V \end{bmatrix} = \begin{bmatrix} \mathbf{J}_q & {}^{\mathbf{B}_I}\mathbf{U}_{\mathbf{B}_3}^T \\ 0 & I_6 \end{bmatrix} \begin{bmatrix} \dot{\mathbf{q}} \\ {}^{\mathbf{B}_I}V \end{bmatrix}, \tag{3.3}$$

where $\dot{\mathbf{q}} = \left[\dot{\theta}_1\ \dot{\theta}_2\ \dot{\theta}_3\right]^T$ is the joint velocity vector, ${}^{\mathbf{B}_I}V \in \mathbb{R}^6$ is the platform floating-base velocity vector, and ${}^{\mathbf{B}_3}V \in \mathbb{R}^6$ is the velocity vector of the TCP.

Equation (3.3) describes the forward kinematics of a TCP movement as a function of joint movements. However, in Cartesian space robotic control, the desired joint movements are defined as a function of TCP movements in Cartesian space. Therefore, the inverse solution for forward kinematics in equation (3.3) can be written as

$$\dot{\mathbf{q}}_r = \mathbf{J}_x^{-1} v_{3r} - \mathbf{J}_q^{*\mathbf{B}_I} \mathbf{U}_{\mathbf{B}_3}^{T\ \mathbf{B}_I} V_r, \tag{3.4}$$

where ${}^{\mathbf{B}_I}V_r$ is the required platform velocity, v_{3r} is the required linear velocity of the TCP, $\dot{\mathbf{q}}_r$ is the required joint velocity vector, and $\mathbf{J}_x \in \mathbb{R}^{3\times 3}$ is the displacement Jacobian. Given the redundant nature of a floating-base system, the weighted pseudoinverse solution for the Jacobian inverse $\mathbf{J}_q^* \in \mathbb{R}^{3\times 6}$ is used to provide the inverse solution for the Jacobian matrix. In this study, the inverse solution is calculated by using Moore-Penrose pseudoinverse solution in Matlab. If the floating-base movements are not compensated for with actuators, the platform velocities cannot be controlled during base movements. As to the floating-base motions that result from rough-terrain conditions, it can be assumed that the required base velocities are the same as the estimated base velocities. In industrial applications, the 6-DOF motions of the platform can be estimated by using IMU sensors with global navigation satellite systems. The VDC control design for manipulator in Figure 3.2 requires that velocity and acceleration estimates for the base and manipulator are available. These signals can be defined by differentiating velocity measurement signals in industrial cases, which typically result in delays to and noise in signals. This may cause phase shift to model and limit control performance.

As to the VDC, the control objective is to make the controlled actual velocities track with the required velocities. The general format of a required velocity includes the desired velocity, which is used as a reference, and one or more terms that are related to control tracking errors. The manipulator's required velocities are defined in Cartesian space. Given the floating-base platform movements, the required velocity can be used to compensate for them in the HHM arm tip frame. Now, the required linear velocity vector v_{3r} for the TCP in equation (3.4) can be defined as

$$v_{3r} = v_{3d} + \lambda(X_d - X), \tag{3.5}$$

where $\lambda \in \mathbb{R}^{3\times 3}$ is the position feedback gain matrix with diagonal for the Cartesian position, $X_d \in \mathbb{R}^3$ and $X \in \mathbb{R}^3$ are the desired and measured Cartesian position values for the TCP, respectively, and v_{3d} is the desired linear velocity for the TCP. Typically, the desired positions and linear velocities are provided as a reference trajectory or with joysticks for the TCP.

3.2.2 Anti-Sway Control for Passive Joints

By comparing the floating-base manipulator shown in Figure 3.2 to the HHM with passive joints in Figure 3.3, it can be noted that the passive joints in the latter are connected at the manipulator tip. These passive joints enable load-grasping movements in both vertical and horizontal space. Similarly to a floating-base manipulator, only the desired position and velocity references for the HHM arm tip can be defined so that the system is directly controllable. In this thesis, both of these angular movements are measured. In P-I, an NMB control design for the HHM with 2-DOF passive joints shown in Figure 3.3 is proposed by using the VDC approach to handle anti-sway damping control.

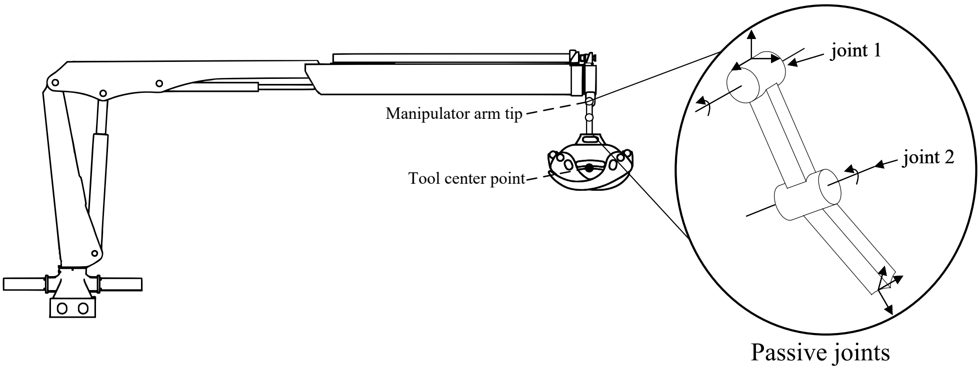

Figure 3.3 Heavy-duty manipulator with load-grasping tool connected with 2 degrees of freedom passive joints.

Like the manipulator in Figure 3.2, the forward and inverse kinematics for the manipulator with passive joints can be defined by using DH parameters. The more detailed dynamics modeling for the manipulator in Figure 3.3 is proposed in P-I. As is presented in equation (3.5), the Cartesian space position tracking error can be incorporated into the required velocity to compensate for oscillation in the load-grasping tool. The oscillation of the passive joints can be compensated for by defining the required velocities in joint space for passive joints. To minimize oscillation, the desired value for both the angular velocity and joint angles in the two joints is zero.

The required joint velocity for the passive joints can written as

$$\dot{q}_{i\mathrm{r}} = \dot{q}_{i\mathrm{d}} + \lambda_i(q_{i\mathrm{d}} - q_i), \tag{3.6}$$

where λ_i $\forall i \in \{1, 2\}$ is the position feedback gain for passive joints, $\dot{q}_{i\mathrm{r}}$ is the required velocity for the joint, $\dot{q}_{i\mathrm{d}}$ is the desired velocity for the passive joint, and $q_{i\mathrm{d}}$ and q_i are the desired and measured passive joint angles, respectively. The control gains are selected such that magnitudes are not subject to unstable behavior in the manipulator system. The torque requirements for passive joints are studied in dynamics modeling. These are specified in same authors external publication [92].

By using the required velocities in equation (3.6) for the passive joints' anti-sway functionality, the required force/moment terms at the TCP coordinate frame can be defined by using dynamics equations for the passive joints and the load-grasping tool. Ultimately, the swaying damping in this proposed control design is based on the force error in the hydraulic cylinder control equations. In P-I, the experimental results with a full-size HHM are presented to verify the performance of the proposed anti-sway controller.

3.3 Hydraulic Actuators with High Gear Ratios and Static Input Nonlinearities

Static and non-smooth nonlinearities typically limit the control performance of hydraulically actuated gears. In a commonly used control design, the effects of the specific nonlinearity are compensated for by using its nonlinear inverse model. Due to inaccurate estimates and missing manufacturer information, accurate modeling of these nonlinearities typically leads to uncertain model parameters. Therefore, adaptive control methods should be used to improve the model-based control of these nonlinear actuators.

As to HHMs, mechanical gears are typically used to actuate the joints, which are needed to provide the wide range of motion that is available with hydraulic cylinder driving joints. For the HHMs in Figure 1.1, hydraulic linear actuators integrated with gears are used to implement base rotation to provide a range of motion over 360°. A common method to implement this rotation is to use a hydraulic rack and pinion actuator, as shown in Figure 3.4. Other common methods are motors with gear rings and articulated steering. However, articulated steering leads to lower motion than the other options due to the cylinder stroke. This thesis focuses on studying a hydraulic rack and pinion actuator because it is widely used in state-of-the-art HHMs. However, the proposed nonlinearity compensations can also be extended to other actuators. Rapid accelerations of heavy loads with long reach produce significant torque on a rack and pinion actuator. In addition, this actuator has a significant backlash, which is acceptable in human operator open-loop systems. The control performance of this actuator directly affects the entire control system performance because the base rotation enables the horizontal movement.

On the other hand, in multi-DOF HHMs, wide actuator ranges of motion are required in hydraulically actuated 3-DOF wrist configurations. As presented in Chapter 2, this configuration consists of three helical gear actuators. The principle for these actuators is depicted in Figure 3.5. In this configuration, a nearly 360° range of motion for the first and last actuators is required, while the actuator in the middle requires a nearly 180° range of motion. Similarly, for the actuators in both Figure 3.4 and Figure 3.5, the hydraulic valve is used to control the symmetric hydraulic cylinder. In P-II and P-IV, the VDC approach is used as a framework to enable a control design for these actuators with high gear ratios and static input nonlinearities divided into modular subsystems. In addition, a stability analysis for a 3-DOF wrist and hydraulic rack and pinion actuator is proposed.

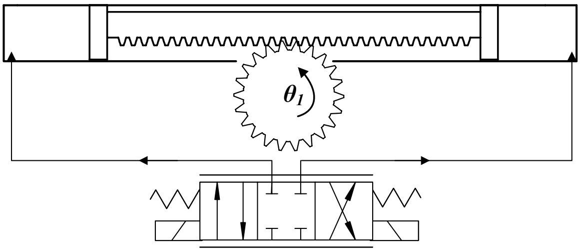

Figure 3.4 Hydraulic rack and pinion actuator.

3.3.1 Adaptive Backlash Compensation

Backlash is one of the most common non-smooth nonlinearities in mechanical gears; it describes the clearance of adjacent moving parts. A simplified model to describe backlash is presented in Figure 3.6a. This model consists of two parallel lines that

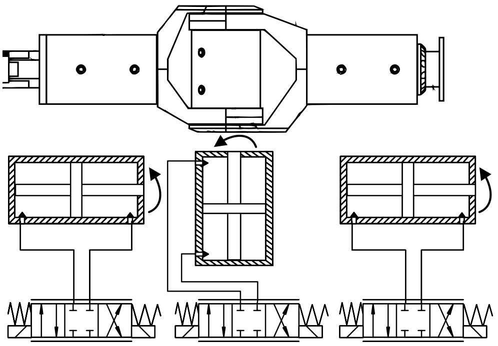

Figure 3.5 Hydraulically actuated wrist.

are connected to each other with a horizontal line to describe the effect of backlash. Due to the nature of backlash, the direction of motion affects the model output. When the downward line is active, the backlash model input v_{bc} and the output u_{bc} both decrease, as shown in Figure 3.6a. Conversely, when the upward line is active, then v_{bc} and u_{bc} both increase. In Figure 3.6a, $c_r > c_l$ holds for the model offsets. The principle of an inverse model for backlash is depicted in Figure 3.6b.

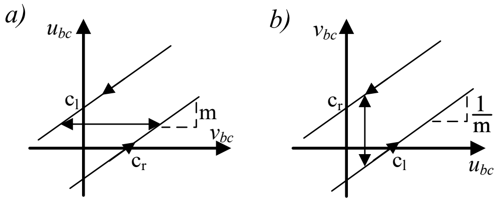

Figure 3.6 Backlash and inverse backlash models.

The mathematical model for backlash in Figure 3.6b can be defined with a continuous time model [37] as

$$\dot{u}_{bc} = \begin{cases} m\dot{v}_{bc} & \dot{u}_{bc} > 0 \text{ and } u_{bc} = m(v_{bc} - c_r) \\ m\dot{v}_{bc} & \dot{u}_{bc} < 0 \text{ and } u_{bc} = m(v_{bc} - c_l) \\ 0 & \text{otherwise} \end{cases}, \tag{3.7}$$

where $u_{tr} = u_{bc}$ and $\dot{u}_{tr} = \dot{u}_{bc}$ are the desired values for model outputs, respectively, and m is the slope gain. On the other hand, by assuming that the desired output signals generate unique input signals, the inverse model for backlash can be written

[37] as

$$v_{bc} = \begin{cases} \frac{u_{tr}}{m} + c_r & \text{if } \dot{u}_{tr} > 0 \\ \frac{u_{tr}}{m} + c_l & \text{if } \dot{u}_{tr} < 0 \\ \frac{u_{tr}}{m} & \text{if } \dot{u}_{tr} = 0 \end{cases}. \tag{3.8}$$

Given the mathematical model for backlash, the model is not continuously derivative due to discontinuous switching conditions. In the VDC approach, stability analysis requires that the modeling for the system should be differentiable. Therefore, before the inverse backlash can be incorporated into the control design, the discontinuous switching functions need to be replaced with smooth switching functions. In equations (3.7)–(3.8), two different discontinuous switching functions need to be replaced. First, the sign function needs to replace with a continuous switching function [24] as follows:

$$\eta_c(x) = \frac{\tanh([x - x_o]\,/c_{\eta c}) + 1}{2}, \tag{3.9}$$

where x_o is a sufficiently small offset constant parameter, and c_{η_c} is a sufficiently small constant. By selecting reasonable values for these offset parameters, the function provides smooth switching. Second, the discontinuous function in (3.8) can be replaced with

$$\eta_s(x) = 1 - \tanh(c_{\eta s}\,|x|), \tag{3.10}$$

where $c_{\eta s}$ is a sufficiently high constant value. As a result, equation (3.8) can be rewritten with VDC approach notations as follows:

$$\begin{aligned} v_{bc} &= \frac{u_{tr}}{\widehat{m}} + \widehat{c_r}\eta_c(\dot{u}_{tr}) + \widehat{c_l}\eta_c(-\dot{u}_{tr}) \\ &= \begin{bmatrix} u_{tr} \; \eta_c(\dot{u}_{tr}) \; \eta_c(-\dot{u}_{tr}) \end{bmatrix} \begin{bmatrix} \frac{1}{\widehat{m}} \; \widehat{c_r} \; \widehat{c_l} \end{bmatrix}^T \\ &= \mathbf{Y}_{bc}(\dot{u}_{tr})\widehat{\theta}_{bc} \;\in \mathbb{R}, \end{aligned} \tag{3.11}$$

where $\widehat{m}$, $\widehat{c_r}$, and $\widehat{c_l}$ are estimates for the backlash model parameters m, c_r, and c_l, respectively. Given that backlash parameters are usually uncertain, the parameter adaption for backlash slope and model offset parameters can be used. This parameter adaption is presented in P-II. The unique property of VDC is to provide stability analysis locally, at the subsystem level. The stability of the proposed adaptive backlash compensation is also given in P-II, with rigorous stability analysis.

The VDC approach is a velocity control-based method. Therefore, the backlash inverse velocity for equation (3.8) needs to be defined. Similarly, the velocity model can be written in view of VDC by using continuous switching functions in equations (3.9) and (3.10). So, the velocity model can be defined as

$$\dot{v}_{bc} = \mathbf{Y}_{bv}(\dot{u}_{tr})\widehat{\theta}_{bv}, \tag{3.12}$$

where

$$\mathbf{Y}_{bv}(\dot{u}_{tr}) = \begin{bmatrix} \dot{u}_{tr}\eta_c(\dot{u}_{tr}) & \dot{u}_{tr}\eta_c(-\dot{u}_{tr}) & c_k\eta_c(\dot{u}_{tr}) & -c_k\eta_c(-\dot{u}_{tr}) \end{bmatrix} \in \mathbb{R}^4, \tag{3.13}$$

and

$$\widehat{\theta}_{bv} = \begin{bmatrix} \frac{1}{\widehat{m}}\eta_s(v_{bc} - \frac{u_{tr}}{\widehat{m}} - \widehat{c}_r) \\ \frac{1}{\widehat{m}}\eta_s(v_{bc} - \frac{u_{tr}}{\widehat{m}} - \widehat{c}_l) \\ \eta_s(v_{bc} - \frac{u_{tr}}{\widehat{m}} - \widehat{c}_l) \\ \eta_s(v_{bc} - \frac{u_{tr}}{\widehat{m}} - \widehat{c}_r) \end{bmatrix} \in \mathbb{R}^4. \tag{3.14}$$

In equation (3.14), c_k is the boundary gain for the vertical jump. Now, the backlash inverse model can be incorporated into the control design by using the required velocity property (see equation (3.5)):

$$\dot{\theta}_r = \mathbf{Y}_{bv}(\dot{u}_{tr})\widehat{\theta}_{bv} + \lambda(\mathbf{Y}_{bc}(\dot{u}_{tr})\widehat{\theta}_{bc} - \theta_1), \tag{3.15}$$

where $\dot{\theta}_r$, λ is the feedback gain for the angular position tracking error, and θ_1 is the measured joint angle. As the equation (3.15), the implementation of the proposed backlash adaptation required measured value for manipulator base rotation joint. For the base rotation cylinder, also the cylinder chamber pressures are required.

In P-II, the backlash model is incorporated into the VDC design for a hydraulic rack and pinion actuator (see Figure 3.4) to improve the HHM plane motion control horizontally. Further, in P-IV, the proposed backlash compensation is incorporated into the control design for a hydraulically actuated helical gear actuator (see Figure 3.5). Helical gear actuators are compact, but the high-speed gears create significant friction. In NMB control, the feedforward control term also requires an accurate friction model for gear friction estimation. The VDC approach provides an adaptive friction model that is incorporated into the control design developed in [26]. The experimental verification presented in P-II and P-IV shows that VDC improves the control performance of hydraulic actuators with static input nonlinearities and high gear ratios by using adaptive control.

3.4 Model-Based Control of Hydraulic Series Elastic Actuators

SEAs are common in torque-controlled electric LWA robotic applications to produce high force fidelity, shock tolerance, and force sensing for contact space motions. Traditionally, robot actuators are designed for high stiffness to increase system position accuracy. High-performance force control is needed to improve system safety by decreasing interaction stiffness. However, HSEAs for linear actuators with high payloads are investigated in only a few studies, and HSEA experimental verification does not exist for high payloads. P-V and P-VI focus on providing control methods for HSEAs in HHMs. In the context of HHMs, HSEAs are required to provide high power-to-weight ratios. The inherent system dynamics and variable stiffness of the fluid lead to a fifth-order dynamics system. For this reason, high-performance control design for HSEAs is challenging.

The proposed HSEA has a mechanical spring to decouple the cylinder power shaft from the environment. The designed HSEA consists of a hydraulic cylinder that is connected in series with a spring attached to the load. The principle of the HSEA is illustrated in Figure 3.7. In this system, spring stiffness is symmetrical in both directions to enable force sensing in both directions. In this thesis, the hydraulic cylinders are driven with a servo valve to enable high bandwidth for control. The real-time control setup in Figure 3.8 with a load mass of 200 kg was implemented with a Beckhoff Industrial PC CX2030 and a sampling rate of 1000 Hz. In this setup, sensors for both cylinder position and spring compression were used. In addition, the actuator chamber pressures and supply pressure were measured.

In P-V, a spring stiffness design for HSEAs is considered. By increasing the equivalent spring stiffness of the actuator, the force controllability also increases, which in turn minimizes the actuator nonlinearities that need low spring stiffness. Concurrently, increasing spring stiffness raises the natural frequency of the system. The aim of the SEA is to improve the force controllability of the system. Therefore, the spring stiffness should be lower than the system's hydraulic oil stiffness. As to

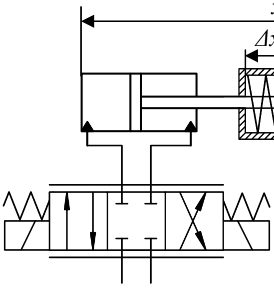

Figure 3.7 Hydraulic series elastic actuator principle.

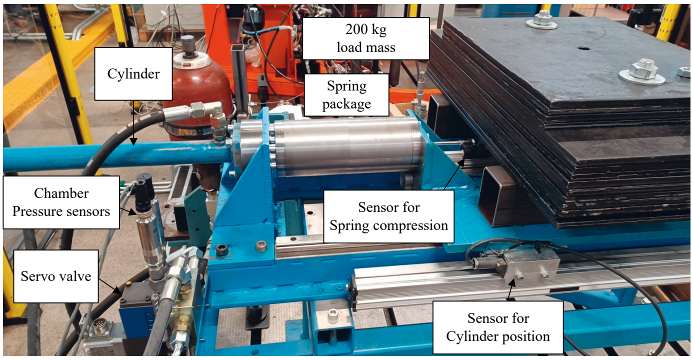

Figure 3.8 Hydraulic series elastic actuator experimental setup.

HHMs, the hydraulic resonance frequency is about 0.5 Hz–5 Hz. The spring stiffness design is a compromise between force controllability and smooth response.

The objective of an SEA is to provide force sensing in contact space motions. Typically, the hydraulic actuator force is estimated by using cylinder chamber pressures. Therefore, an accurate force estimation requires an accurate friction force estimation. The estimation for actuator contact force can be obtained by using the spring compression and stiffness in HSEAs.

3.4.1 Impedance Control Design for Hydraulic Series Elastic Actuators

The impedance control design for the HSEA shown in Figure 3.7 needs to be used an outer-loop controller to handle the dynamics of contact space motion. Thus, the control design for the valve and hydraulic dynamics needs to be defined to serve as an inner-loop controller. The block diagram for the controller structure is presented in Figure 3.9. In P-V and P-VI, two different control designs for HSEAs are presented.

First, a PBIC with linear full-state feedback control is described. Second, an NMB control design for HSEAs is proposed to handle impedance control. In both publications, the dynamic modeling for the HSEA is investigated first, after which the proposed model-based controller is incorporated into impedance control designs.

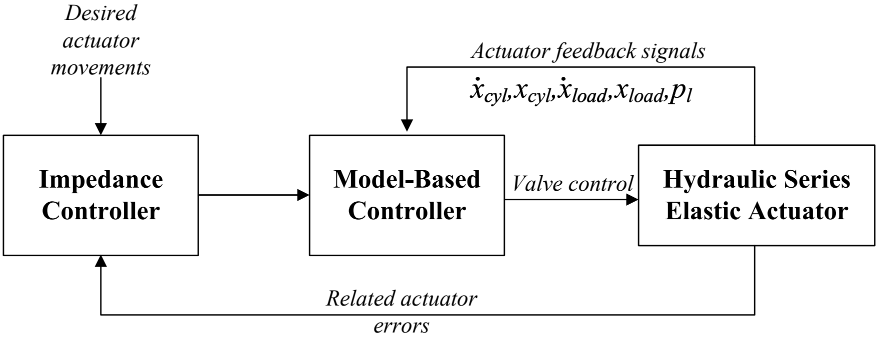

Figure 3.9 Impedance controller block diagram for hydraulic series elastic actuator.

In P-V, a full-state feedback controller is designed by using linear control methods to investigate the dynamics properties of HSEA. As an outcome, a full-state feedback control is designed, in which the state variables used are all measurements found in Figure 3.9: position and velocity signals for load and cylinder position and actuator pressure difference. The linearized control design for the hydraulic system assumes linear behavior for the cylinder and flow continuity equations. These measurements are required for implementation of the impedance controller for the HSEA. One method to implement the outer-loop controller is to use a PBIC, where the cylinder position error is used to define the contact force between the actuator and the environment. The block diagram for proposed PBIC is presented in Figure 3.10. In that figure, inverse dynamics control is used to handle the dynamics of contact space motion. As an output, this impedance controller gives an estimate of contact compression, which limits the actual reference for the cylinder position, as presented in Figure 3.10.

Linear control of the hydraulic dynamics can lead to limited control performance. Therefore, in P-VI, a NMB control design for the hydraulic system is proposed. The NMB control design enables the division of the HSEA into two subsystems so that the dynamics modeling for the hydraulic actuator side and the load-side dynamics can be handled separately. Compared to state feedback control in P-V, the NMB control design also enables the incorporation of a nonlinear friction model into the

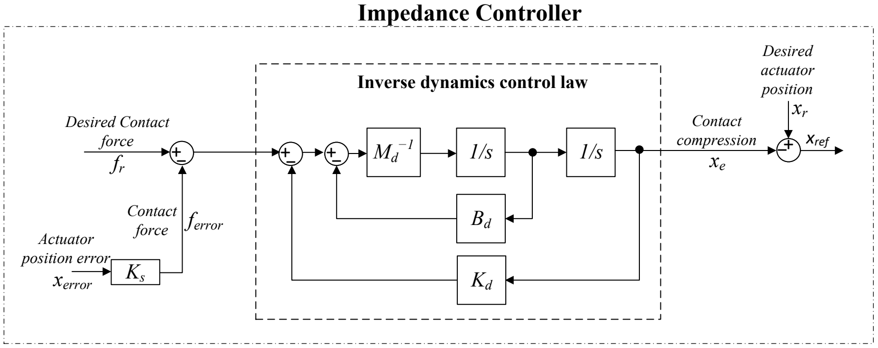

Figure 3.10 Position-based impedance controller for hydraulic series elastic actuator.

actuator control design. Now, the NMB control design for HSEAs can be made without assumptions regarding hydraulic system dynamics.

As noted above, the required velocity property of the VDC approach consists of the desired velocity and other terms to control error. Therefore, the inverse impedance control law in Figure 3.10 can be rewritten as

$$\dot{x}_r = \dot{x}_{dl} + K_x B_d^{-1}(x_{dl} - x_l) + B_d^{-1}(f_r - f_{error}), \tag{3.16}$$

where $\dot{x}_r$ is the required velocity, f_r is the desired contact force, f_{error} is the contact force, x_{dl} is the desired load position, x_l is the measured load position, and K_x and B_d are the contact dynamics damping and stiffness parameters, respectively. In equation (3.16), the effect of inertia matrix M_d is neglected. Thus, the impedance controller in equation (3.16) limits the actuator's required velocity.

Both P-V and P-VI provide solutions to design control methods for HSEAs in HHMs. The effectiveness of the proposed control methods was verified in a linear test setup with a 200 kg payload. In P-VI, the NMB control design for HSEAs is provided to enable adding an actuator to HHMs to improve force controllability in industrial applications requiring contact with the environment and for specific tools that make contact with the environment.

4 DISCUSSION

This chapter discusses the RPs defined at the beginning of the thesis and summarizes how they have been addressed. After the RPs are discussed, conclusions are presented.

4.1 Modular Nonlinear Control Design (RP-I)

Can subsystem-based design methods improve control system modularity in commercial heavy-duty hydraulic manipulators with different product variants?

The first RP involves the modular control design for HHMs with various tool attachments and actuators. The tool attachments studied in P-I and P-IV are connected to the HHM arm tip. The publication demonstrates that with a modular control design, the required modifications for previously designed control equations can be decreased and the reusability of the designed control equations can be increased. Similarly, modular control designs for a hydraulic rack and pinion actuator and an HSEA are proposed in P-II and P-VI. P-III demonstrates the suitability of the modular control design to handle floating-base movements, as in the control design for HHMs, by incorporating base movements into the NMB control design.

Compared to industrial applications, advanced modular design verification in laboratory conditions has certain drawbacks. First, NMB control requires an angular measurement for each manipulator joint. Second, the modeling also requires that velocity and acceleration estimates for each manipulator joint be available. These signals can be defined by differentiating angular measurement signals in industrial cases, which typically result in delays to and noise in signals. Third, dynamics modeling requires accurate model parameters to describe the target system. This issue may be handled with parameter adaptation. The NMB design for hydraulic actuators requires chamber pressure measurements for each actuator to supplement dynamics modeling.

The results in P-I–P-IV and P-VI demonstrate that the NMB control design provides control system design modularity for HHMs with different tool attachments and actuator variants.

4.2 Hydraulic Actuators with High Gear Ratios and Static Input Nonlinearities (RP-II)

Can nonlinear control design methods be used to provide modular high-performance control for hydraulic actuators with high gear ratios and static input nonlinearities?

Hydraulic actuators with high gear ratios and static input nonlinearities are studied in P-II and P-IV. First, a hydraulic rack and pinion actuator in manipulator base rotation is examined in P-II, the main focus of which is to improve the control performance of a low-damped base rotation actuator. Inertial load results in low damping in hydraulic actuators, and gear nonlinearities also limit control performance. One of the most common static nonlinearities in mechanical gears is backlash. In P-II, adaptive backlash compensation is incorporated into the VDC design to improve the control performance of these actuators. Under laboratory conditions, the effectiveness of the proposed adaptive compensation was verified by comparing control results to actual measured gear backlash. In addition, the effects of the backlash compensation for the control performance are addressed in this publication.

Second, the helical gear actuators are explored in P-IV to enable robotic control for a 3-DOF HHM equipped with a 3-DOF wrist configuration. While helical gear actuators are compact, the high speed of the gears causes significant friction. The NMB controller for the hydraulically actuated wrist using the VDC approach as a framework is studied in this publication to improve the control performance of the robotic control of a 6-DOF HHM. The effectiveness of the proposed NMB control for helical gear actuators was verified in a full-size hydraulically actuated wrist configuration.

4.3 Underactuated System with Anti-Sway and Damping Control Methods (RP-III)

Can model-based control methods be used for underactuated heavy-duty system control?

P-I and P-III explore anti-sway and damping control methods for underactuated HHMs. The underactuated nature of manipulators often follows from the passive joints in the system. Very commonly, HHMs are equipped with a rotating load-grasping tool connected to the HHM arm tip with a pair of passive joints to enable both horizontal and vertical movements for the tool. These passive joints are subject to sway in free space motions due to HHM arm tip accelerations. To increase system controllability, an NMB design based on anti-sway control is incorporated into the dynamics modeling of the HHM in P-I. The experimental results with accurate estimates for passive joint angles and velocities show that the proposed method improves the controllability of the underactuated manipulator.

Further, manipulator underactuation may also follow from floating-base movements in the entire system. In common applications, floating-base movements are caused be rough-terrain conditions for the mobile manipulator. These manipulator floating-base movements during operations need to be considered in the control design for the TCP. In P-III, the floating-base movements in Cartesian space are incorporated into the NMB control design for HHMs. Using simulation results, the effectiveness of the proposed method was verified with multi-DOF floating-base movements.

P-I and P-III provide a modular NMB control method to compensate for oscillations in underactuated HHMs.

4.4 Hydraulic Series Elastic Actuators (RP-IV)

Can series elastic actuators provide high force fidelity in heavy-duty hydraulic manipulators with enhanced contact force estimation?

HSEAs for HHM applications are explored in P-V and P-VI. In these publications, the modeling and control design for HSEAs are studied in both free space motion and in contact space motion. The control design in contact space motion is investigated by designing an impedance control model for the prototype HSEA. First, in P-VI, the modeling and control design for a fifth-order HSEA system are proposed by using a linear control design with associated approximations in dynamics modeling. This publication also explores methods to improve contact force estimation for HSEAs by using spring compression and spring stiffness. The proper selection of spring stiffness for actuators is also discussed.

In P-VI, the results from P-V are extended by using the VDC approach to HSEA impedance control design. Compared to the linear control design in P-V, the NMB control design enables the design of control equations without approximations. The effectiveness of the proposed control equations was verified under a variety of contact conditions. The proposed control methods provide a solution to control HSEAs in HHM applications during contact space motion.

5 CONCLUSIONS AND FUTURE WORK

This thesis has developed methods to increase the modularity of NMB control design by providing systematic methods that can handle HHMs. In the attached publications, a modular control design for HHMs with different actuators and tool attachments is proposed to improve the reusability of the designed control equations. Further, the NMB control method is extended to handle the floating-base movements of HHMs. Experiments with a full-size commercial HHM under indoor laboratory conditions were used to verify the effectiveness of the proposed control methods in the attached publications. As Chapter 4 summarizes, all the RPs are successfully addressed in those publications.

5.1 Modular Nonlinear Model-Based Control Design for Heavy-Duty Manipulators

P-I and P-IV propose a modular NMB control design method for HHMs with a variety of tool attachments. Further, floating-base motions of manipulator bases in HHMs are investigated in P-III. These publications verify that an NMB control design can be used to decrease the number of modifications for existing HHM arm control design with various tool attachments, which directly answers **RP-I**. With systematic control design methods, it is possible to increase the reusability of the designed control equations for functional subsystems in an HHM. In addition, a rigorous stability analysis for the entire system is presented with tool attachment variants locally at the subsystem level to complement the modular high-performance control design.

In hydraulic actuators, static input nonlinearities and high gear ratios affect control performance. P-II and P-IV focus on improving the control performance of these actuators by incorporating model-based compensation for common nonlinearities. In these publications, an adaptive backlash compensation is proposed for the

NMB control design, supported by a rigorous stability analysis of the actuator configuration. The experimental results in these publications indicate that NMB control methods can be used to improve the control performance of these actuators. Further, the effectiveness of the proposed parameter adaptation has been demonstrated through experimental results. These publications speak to **RP-II**.

The NMB control for underactuated HHMs is examined in P-I and P-III, where the damping methods for passive joints and floating-base movements are investigated. P-I focuses on studying an HHM equipped with passive joints and a load-grasping tool and providing anti-sway control for this underactuated manipulator system. P-III, meanwhile, focuses on studying damping control for HHMs with a floating base by compensating for platform movements in Cartesian space control. These publications directly answer **RP-III**.

P-V and P-VI investigate the suitability of HSEAs for HHM applications. The main focus is to improve force fidelity and shock tolerance for fifth-order HSEA systems in HHM applications. In addition, an HSEA is used to estimate the actuator contact force during contact space motion. These publications answer **RP-IV**.

5.2 Future Work

As to industrial applications, a few challenges remain with the proposed control methods. As summarized in Chapter 3, high-performance control design requires accurate modeling of the system. Hence, an accurate position and joint angle measurements are also needed. Most actuators and joint angles can be directly equipped with a robust sensor system. However, in many industrial applications, the estimates for passive joints are not directly measurable due to challenging working conditions. Therefore, estimates for these passive joint angles need to be defined for industrial applications. Second, for the SEA measurement methods, all required measurements need to improve. Finally, servo valves should be replaced with mobile valves in industrial applications.

In the attached publications, the control methods for HHMs were verified in free space motion. In future studies, the proposed control methods need to be verified for 6-DOF HHMs in contact space motion. In future research, the NMB control for HSEAs will need to be added to a full-size multi-DOF manipulator; it is likely that an HSEA can be most useful when equipped with a tool attachment as a linear actuator that needs contact control with the environment while environmental stiffness varies. In addition, future studies should investigate the gravitational force effects for HSEAs with high loads. Further, the proposed control methods for HSEAs can be studied with electrical linear actuators in HHM applications to improve shock tolerance.

6 SUMMARY OF PUBLICATIONS

This chapter summarizes each publication associated with this thesis and clarifies how each publication addresses one or more RPs. The modular control design for the HHM with various tool attachments and actuators is discussed in P-I–P-VI. Anti-sway and damping control methods for underactuated manipulators are presented in P-I and P-III. Hydraulic actuators with high gear ratios and static input nonlinearities are discussed in P-II and P-IV. Finally, HSEAs for HHM applications are investigated in P-V and P-VI. The effectiveness of the proposed control design methods was verified under laboratory conditions with the full-size experimental setups shown in Figure 1.2 and Figure 3.8 for all proposed control methods, except the control design in P-III, which was verified through simulation results.

6.1 Stability-Guaranteed Anti-Sway Controller Design for a Redundant Articulated Hydraulic Manipulator in the Vertical Plane

This publication discusses applying the modular NMB control design to HHMs with load-grasping tools. The passive joint connection of the load-grasping tool to the HHM arm tip leads to an underactuated system. These passive joints are subject to sway in free space motions due to arm tip accelerations. The aim of the paper is to explore the applicability of state-of-the-art control methods for underactuated HHMs. The main focus is an extended NMB controller to address the anti-sway damping control of passive joints.

The experimental results with a full-size HHM indicate that a proposed novel stability-guaranteed anti-sway control can be used to dampen the load swaying more than twice as fast as the situation without anti-sway control. This result answers **RP-III**. At the same time, the modular control design enables incorporating the proposed control into previously designed control equations without any modifications, which speaks directly to **RP-I**.

6.2 Nonlinear Model-Based Controller Design for a Hydraulic Rack and Pinion Actuator

This publication is focused on studying HHMs with hydraulic rack and pinion actuators. This kind of actuator is commonly used in base rotation for the manipulator to enable a range of motion over 360° on the horizontal plane. Due to very low damping, the gear is subject to high inertial loads. The actuator also introduces significant nonlinearities into the hydraulic dynamic behavior, including gear backlash. The publication discusses a modular control design for the rack and pinion actuator to improve control performance.

In a novel effort, this publication presents an adaptive backlash compensation that is incorporated into an NMB control design. As a novelty, the stability of the proposed controller with adaptive backlash compensation was guaranteed by rigorous stability analysis. The experimental results with a full-size commercial manipulator indicate that the steady state error with the proposed adaptive compensation was 0.01°, whereas the steady state error without backlash compensation was 0.1°. The effectiveness of the proposed rapid parameter adaptation for backlash was also verified experimentally by measuring the actual gear backlash. These results directly answer **RP-II**. The modular control equations can be added in plug-and-play form to the previously presented modular control design, which directly answers **RP-I**.

6.3 Cartesian Damping Controller with Nonlinear Control for a Floating-Base Hydraulic Manipulator

This publication discusses a rigid manipulator with floating-base motions, which are common in mobile manipulators, where a rigid HHM is mounted on a moving platform to extend the working area. Due to stiff connections, platform movements affect the control of the HHM. The main contribution of this publication is to study the effects of the floating base on Cartesian space control. In the rough-terrain conditions faced by a mobile manipulator, floating-base movements follow from the movements of the mobile platform. In this publication, it is assumed that there are no actuators to compensate for the manipulator's floating-base movements. As a novelty, the NMB control design for a manipulator with a floating base was built by using the VDC approach as a framework. According to the kinematics of the entire system, platform movements can be compensated in TCP movements by using properties of the proposed NMB control design. The Cartesian space control in the previously designed controller for HHMs in P-II is incorporated into the control design without any modifications to previously designed control equations.

Simulation results with a full-size HHM were used to verify the effectiveness of the proposed control methods. In those results, the floating-base platform motions are considered and speak to **RP-III**.

6.4 Nonlinear Model-Based Control Design for a Hydraulically Actuated Spherical Wrist

This publication discusses an HHM equipped with a hydraulically actuated wrist, which extends the entire system into 6-DOF. The spherical wrist is a common structure in robotics to increase the manipulator's dexterity and work envelope. In this publication, the novel contribution is to propose a modular control design for the wrist configuration by using the modular VDC approach as a framework. The modular control design enables the incorporation of the proposed controller into the previously designed controller in P-II without modifications to the manipulator arm control design. The main contribution in this publication is to design a novel modular control equations for the helical gear hydraulic actuators in the wrist configuration. The actuators introduce significant nonlinearities in dynamics behaviors, including gear backlash and actuator friction. Therefore, the previously designed adaptive backlash compensation is included in the control design.

Experimental results with a full-size setup under laboratory conditions verified that the proposed control methods decrease position tracking error during motion. This result speaks to **RP-II**.

6.5 Position-Based Impedance Control Design for a Hydraulically Actuated Series Elastic Actuator

This publication acts as a preliminary study for the HSEAs. Compared to traditional stiff actuators, HSEAs can provide high force fidelity, shock tolerance, and force sensing for interaction control in HHM applications. By considering the inherent system dynamics and the fluid's variable stiffness, the control design for HSEAs leads to a fifth-order system. The main contribution of this publication is to study the design control architecture for HSEAs in heavy-duty applications. Further, spring stiffness selection for HSEAs in HHM applications is discussed. The designed control architecture consists of a full-state feedback controller as an inner-loop controller and the PBIC as an outer-loop controller.

In the results, performance analyses and experimental results with an HSEA for heavy loads are discussed. The results indicate that the proposed control architecture can effectively control a fifth-order system with a payload of 200 kg. In general, the experimental results verified that the proposed controller structure can handle control of a highly nonlinear HSEA system with a heavy load in both free space and contact space motions by decreasing the contact force of the HSEA. These results directly answer **RP-IV**.

6.6 Impedance Control of Hydraulic Series Elastic Actuator with a Model-Based Control Design

This publication extends the work in P-V to propose a novel NMB control design for HSEAs. Further, an impedance control for HSEAs is proposed by incorporating the designed controller as an inner-loop controller with a previously designed impedance control. Due to the highly nonlinear dynamics behavior of hydraulic systems, NMB control methods are needed to improve control performance.

The experimental results were used to verify that proposed impedance control design can be efficient at damping the contact between the HSEA in both stiff and flexible environments. As an outcome, the modular VDC design for the subsystem model controller enables the designed subsystem block to be connected using a plug-and-play approach into an existing multi-link controller structure. This publication speaks to **RP-IV**.

REFERENCES

[1] EU, *EU Robotics*. 2018, accessed 23.8.2022, [Online]. Available: Strategic research agenda for robotics in europe 2014–2020.

[2] Sandvik, *Automine*. 2021, accessed 24.8.2022, [Online]. Available: www.rocktechnology.sandvik/en/campaigns/nextgenautomation/.

[3] J. Mattila, J. Koivumäki, D. G. Caldwell, and C. Semini, "A survey on control of hydraulic robotic manipulators with projection to future trends," *IEEE/ASME Transactions on Mechatronics*, vol. 22, no. 2, pp. 669–680, 2017. DOI: 10.1109/TMECH.2017.2668604.

[4] Ponsse, *Active Crane*. 2021, accessed 24.8.2022, [Online]. Available: www.ponsse.com/en/web/guest/products/tailored-solutions/product/-/p/activecranebisonbuffaloelephant.

[5] Sandvik, *Automine*. 2021, accessed 24.8.2022, [Online]. Available: https://www.rocktechnology.sandvik/en/products/surface-drill-rigs/.

[6] HIAB, *Crane Tip Control*. 2021, accessed 24.8.2022, [Online]. Available: www.hiab.com/en/media/news/hiab-crane-tip-control.

[7] J. Koivumäki and J. Mattila, "High performance nonlinear motion/force controller design for redundant hydraulic construction crane automation," *Automation in Construction*, vol. 51, pp. 59–77, 2015, ISSN: 0926-5805. DOI: 10.1016/j.autcon.2014.12.014.

[8] J. Koivumäki and J. Mattila, "Stability-guaranteed impedance control of hydraulic robotic manipulators," *IEEE/ASME Transactions on Mechatronics*, vol. 22, no. 2, pp. 601–612, 2017. DOI: 10.1109/TMECH.2016.2618912.

[9] R. Lovgren, "Radical improvements in crane safety," *ISO focus*, vol. 1, no. 7, pp. 21–93, 2004.

[10] L. Sciavicco and B. Siciliano, *Modelling and control of robot manipulators*. Springer Science & Business Media, 2012. DOI: 10.1007/978-1-4471-0449-0.

[11] Epiroc, *Product portfolio*. 2022, accessed 24.8.2022, [Online]. Available: https://www.epiroc.com/en-fi/products.

[12] Normet, *Minimec 2*. 2022, accessed 24.6.2022, [Online]. Available: https://www.normet.com/product/minimec-2-2/.

[13] Normet, *Aliva*. 2022, accessed 24.6.2022, [Online]. Available: https://www.normet.com/product/aliva-520/.

[14] NetworkRail, *On-track Plant Attachment Handbook*. 2015, [Online]. Available: https://safety.networkrail.co.uk/safety/on-track-plant-safety/otp-attachments/otp-attachments-handbook/.

[15] J. Watton, *Fluid Power Systems: modelling, simulation, analog and microcomputer control*. New York: Prentice Hall, 1989, ISBN: 0133231976.

[16] M. M. Bech, T. O. Andersen, H. C. Pedersen, and L. Schmidt, "Experimental evaluation of control strategies for hydraulic servo robot," in *IEEE International Conference on Mechatronics and Automation*, 2013. DOI: 10.1109/ICMA.2013.6617942.

[17] M. Krstic, P. V. Kokotovic, and I. Kanellakopoulos, *Nonlinear and adaptive control design*. John Wiley & Sons, Inc., 1995, ISBN: 041127329.

[18] F. Bu and B. Yao, "Observer based coordinated adaptive robust control of robot manipulators driven by single-rod hydraulic actuators," in *Proceedings 2000 ICRA. Millennium Conference. IEEE International Conference on Robotics and Automation. Symposia Proceedings*, vol. 3, 2000, 3034–3039 vol.3. DOI: 10.1109/ROBOT.2000.846488.

[19] G. O. Tysse, A. Cibicik, L. Tingelstad, and O. Egeland, "Lyapunov-based damping controller with nonlinear mpc control of payload position for a knuckle boom crane," *Automatica*, vol. 140, p. 110 219, 2022, ISSN: 0005-1098. DOI: 10.1016/j.automatica.2022.110219.

[20] J. Kalmari, J. Backman, and A. Visala, "Nonlinear model predictive control of hydraulic forestry crane with automatic sway damping," *Computers and Electronics in Agriculture*, vol. 109, pp. 36–45, 2014, ISSN: 0168-1699. DOI: 10.1016/j.compag.2014.09.006.

[21] W.-H. Zhu, Y.-G. Xi, Z.-J. Zhang, Z. Bien, and J. De Schutter, "Virtual decomposition based control for generalized high dimensional robotic systems with complicated structure," *IEEE Transactions on Robotics and Automation*, vol. 13, no. 3, pp. 411–436, 1997. DOI: 10.1109/70.585903.

[22] W.-H. Zhu and J.-C. Piedboeuf, "Adaptive output force tracking control of hydraulic cylinders with applications to robot manipulators," *Journal of Dynamic Systems, Measurement, and Control*, vol. 127, no. 2, pp. 206–217, Jun. 2004. DOI: 10.1115/1.1898237.

[23] W.-H. Zhu and J.-C. Piedboeuf, "Adaptive output force tracking control of hydraulic cylinders with applications to robot manipulators," *Journal of Dynamic Systems, Measurement, and Control*, vol. 127, no. 2, pp. 206–217, Jun. 2004, ISSN: 0022-0434. DOI: 10.1115/1.1898237.

[24] J. Koivumäki, W.-H. Zhu, and J. Mattila, "Energy-efficient and high - precision control of hydraulic robots," *Control Engineering Practice*, vol. 85, pp. 176–193, 2019, ISSN: 0967-0661. DOI: 10.1016/j.conengprac.2018.12.013.

[25] R. N. Jazar, *Theory of Applied Robotics*. Springer Science & Business Media, 2010. DOI: 10.1007/978-1-4419-1750-8.

[26] W.-H. Zhu, *Virtual decomposition control: toward hyper degrees of freedom robots*. Springer Science & Business Media, 2010, vol. 60. DOI: 10.1007/978-3-642-10724-5.

[27] M. Liu, "Decentralized control of robot manipulators: Nonlinear and adaptive approaches," *IEEE Transactions on Automatic Control*, vol. 44, no. 2, pp. 357–363, 1999. DOI: 10.1109/9.746266.

[28] M. Liu, "Decentralized pd and robust nonlinear control for robot manipulators," *Journal of Intelligent and Robotic Systems*, vol. 20, no. 2, pp. 319–332, 1997. DOI: 10.1023/A:1007968513506.

[29] S.-H. Hsu and L.-C. Fu, "A fully adaptive decentralized control of robot manipulators," *Automatica*, vol. 42, no. 10, pp. 1761–1767, 2006. DOI: 10.1016/j.automatica.2006.05.012.

[30] Z. Li, W. W. Melek, and C. Clark, "Decentralized robust control of robot manipulators with harmonic drive transmission and application to modular and reconfigurable serial arms," *Robotica*, vol. 27, no. 2, pp. 291–302, 2009. DOI: 10.1017/S0263574708004712.

[31] J.-P. Humaloja, J. Koivumäki, L. Paunonen, and J. Mattila, "Decentralized observer design for virtual decomposition control," *IEEE Transactions on Automatic Control*, vol. 67, no. 5, pp. 2529–2536, 2022. DOI: 10.1109/TAC.2021.3083573.

[32] S. Tafazoli, S. Salcudean, K. Hashtrudi-Zaad, and P. Lawrence, "Impedance control of a teleoperated excavator," *IEEE Transactions on Control Systems Technology*, vol. 10, no. 3, pp. 355–367, 2002. DOI: 10.1109/87.998021.

[33] A. Clegg, M. Dunnigan, and D. Lane, "Self-tuning position and force control of an underwater hydraulic manipulator," in *Proceedings 2001 ICRA. IEEE International Conference on Robotics and Automation*, vol. 4, 2001, 3226–3231 vol.4. DOI: 10.1109/ROBOT.2001.933115.

[34] J. Koivumäki and J. Mattila, "Stability-guaranteed force-sensorless contact force/motion control of heavy-duty hydraulic manipulators," *IEEE Transactions on Robotics*, vol. 31, no. 4, pp. 918–935, 2015. DOI: 10.1109/TRO.2015.2441492.

[35] J. Yao, Z. Jiao, D. Ma, and L. Yan, "High-accuracy tracking control of hydraulic rotary actuators with modeling uncertainties," *IEEE/ASME Transactions on Mechatronics*, vol. 19, no. 2, pp. 633–641, 2014. DOI: 10.1109/TMECH.2013.2252360.

[36] J. Heintze, G. van Schothorst, A. van der Weiden, and P. Teerhuis, "Modeling and control of an industrial hydraulic rotary vane actuator," in *Proceedings of 32nd IEEE Conference on Decision and Control*, 1993, 1913–1918 vol.2. DOI: 10.1109/CDC.1993.325527.

[37] G. Tao and P. Kokotovic, "Continuous-time adaptive control of systems with unknown backlash," *IEEE Transactions on Automatic Control*, vol. 40, no. 6, pp. 1083–1087, 1995. DOI: 10.1109/9.388689.

[38] M. Nordin and P.-O. Gutman, "Controlling mechanical systems with backlash—a survey," *Automatica*, vol. 38, no. 10, pp. 1633–1649, 2002, ISSN: 0005-1098. DOI: 10.1016/S0005-1098(02)00047-X.

[39] G. Tao and P. Kokotovic, "Adaptive control of system with unknown output backlash," *IEEE Transactions on Automatic Control*, vol. 40, no. 2, pp. 326–330, 1995. DOI: 10.1109/9.341803.

[40] K.-H. Han, G.-O. Koh, J.-M. Sung, and B.-S. Kim, "Adaptive control approach for improving control systems with unknown backlash," in *11th International Conference on Control, Automation and Systems*, IEEE, 2011.

[41] G. Lai, Z. Liu, Y. Zhang, C. L. P. Chen, and S. Xie, "Adaptive inversion-based fuzzy compensation control of uncertain pure-feedback systems with asymmetric actuator backlash," *IEEE Transactions on Fuzzy Systems*, vol. 25, no. 1, pp. 141–155, 2017. DOI: 10.1109/TFUZZ.2016.2551292.

[42] W. He, D. Ofosu Amoateng, C. Yang, and D. Gong, "Adaptive neural network control of a robotic manipulator with unknown backlash-like hysteresis," *IET Control Theory & Applications*, vol. 11, no. 4, pp. 567–575, 2017. DOI: 10.1049/iet-cta.2016.1058.

[43] J. Guo, B. Yao, Q. Chen, and X. Wu, "High performance adaptive robust control for nonlinear system with unknown input backlash," in *Proceedings of the 48h IEEE Conference on Decision and Control (CDC) held jointly with 2009 28th Chinese Control Conference*, 2009, pp. 7675–7679. DOI: 10.1109/CDC.2009.5399543.

[44] J. Zhou and C. Wen, *Adaptive backstepping control of uncertain systems: Nonsmooth nonlinearities, interactions or time-variations*. Springer, 2008. DOI: 10.1007/978-3-540-77807-3.

[45] L. Xu and B. Yao, "Adaptive robust control of mechanical systems with nonlinear dynamic friction compensation," in *Proceedings of the 2000 American Control Conference*, vol. 4, 2000, 2595–2599 vol.4. DOI: 10.1109/ACC.2000.878676.

[46] Y. Tan, J. Chang, and H. Tan, "Adaptive backstepping control and friction compensation for ac servo with inertia and load uncertainties," *IEEE Transactions on Industrial Electronics*, vol. 50, no. 5, pp. 944–952, 2003. DOI: 10.1109/TIE.2003.817574.

[47] S. Lampinen, J. Koivumäki, J. Mattila, and J. Niemi, “Model-based control of a pressure-compensated directional valve with significant dead-zone,” ser. Fluid Power Systems Technology, vol. ASME/BATH Symposium on Fluid Power and Motion Control, Oct. 2019. DOI: 10.1115/FPMC2019-1664.

[48] J. Nurmi, M. M. Aref, and J. Mattila, “A neural network strategy for learning of nonlinearities toward feed-forward control of pressure-compensated hydraulic valves with a significant dead zone,” ser. Fluid Power Systems Technology, vol. BATH/ASME 2018 Symposium on Fluid Power and Motion Control, Sep. 2018. DOI: 10.1115/FPMC2018-8847.

[49] L. Li, Z. Lin, Y. Jiang, C. Yu, and J. Yao, “Valve deadzone/backlash compensation for lifting motion control of hydraulic manipulators,” *Machines*, vol. 9, no. 3, 2021. DOI: 10.3390/machines9030057.

[50] D. Lewis, G. Parker, B. Driessen, and R. Robinett, “Command shaping control of an operator-in-the-loop boom crane,” in *Proceedings of the 1998 American Control Conference*, vol. 5, 1998, 2643–2647 vol.5. DOI: 10.1109/ACC.1998.688328.

[51] K. L. Sorensen, W. Singhose, and S. Dickerson, “A controller enabling precise positioning and sway reduction in bridge and gantry cranes,” *Control Engineering Practice*, vol. 15, no. 7, pp. 825–837, 2007, Special Issue on Award Winning Applications, ISSN: 0967-0661. DOI: 10.1016/j.conengprac.2006.03.005.

[52] S. Garrido, M. Abderrahim, A. Gimenez, R. Diez, and C. Balaguer, “Anti-swinging input shaping control of an automatic construction crane,” *IEEE Transactions on Automation Science and Engineering*, vol. 5, no. 3, pp. 549–557, 2008. DOI: 10.1109/TASE.2007.909631.

[53] M. A. Ahmad, R. M. T. R. Ismail, and M. S. Ramli, “Input shaping techniques for anti-sway control of a 3-d gantry crane system,” in *International Conference on Mechatronics and Automation*, 2009, pp. 2876–2881. DOI: 10.1109/ICMA.2009.5246433.

[54] H. Ouyang, G. Zhang, L. Mei, X. Deng, and D. Wang, “Load vibration reduction in rotary cranes using robust two-degree-of-freedom control ap-

proach," *Advances in Mechanical Engineering*, vol. 8, no. 3, 2016. DOI: 10.1177/1687814016641819.

[55] N. Uchiyama, "Robust control of rotary crane by partial-state feedback with integrator," *Mechatronics*, vol. 19, no. 8, pp. 1294–1302, 2009, ISSN: 0957-4158. DOI: 10.1016/j.mechatronics.2009.08.007.

[56] F. Palis and S. Palis, "Modelling and anti-sway control of rotary cranes," in *Proceedings of 14th International Power Electronics and Motion Control Conference*, 2010, T5-163-T5–167. DOI: 10.1109/EPEPEMC.2010.5606573.

[57] M. B. Kjelland, I. Tyapin, G. Hovland, and M. R. Hansen, "Tool-point control for a redundant heave compensated hydraulic manipulator," 8, 1st IFAC Workshop on Automatic Control in Offshore Oil and Gas Production, vol. 45, 2012, pp. 299–304. DOI: 10.3182/20120531-2-NO-4020.00034.

[58] M. B. Kjelland, M. R. Hansen, I. Tyapin, and G. Hovland, "Tool-point control of a planar hydraulically actuated manipulator with compensation of non-actuated degree of freedom," in *12th International Conference on Control, Automation and Systems*, 2012, pp. 672–677.

[59] T. Yang, N. Sun, H. Chen, and Y. Fang, "Neural network-based adaptive antiswing control of an underactuated ship-mounted crane with roll motions and input dead zones," *IEEE Transactions on Neural Networks and Learning Systems*, vol. 31, no. 3, pp. 901–914, 2020. DOI: 10.1109/TNNLS.2019.2910580.

[60] J. Neupert, E. Arnold, K. Schneider, and O. Sawodny, "Tracking and anti-sway control for boom cranes," *Control Engineering Practice*, vol. 18, no. 1, pp. 31–44, 2010, ISSN: 0967-0661. DOI: 10.1016/j.conengprac.2009.08.003.

[61] J. Honkakorpi, J. Vihonen, and J. Mattila, "Mems sensor network based anti-sway control system for articulated hydraulic crane," vol. ASME/-BATH 2013 Symposium on Fluid Power and Motion Control, Oct. 2013. DOI: 10.1115/FPMC2013-4439.

[62] F. Rauscher and O. Sawodny, “Modeling and control of tower cranes with elastic structure,” *IEEE Transactions on Control Systems Technology*, vol. 29, no. 1, pp. 64–79, 2021. DOI: 10.1109/TCST.2019.2961639.

[63] X. Zhang, P. Mustalahti, E. Peltola, and J. Mattila, “3d attitude calculation for the grasper of a crane system with a rotary gyroscope,” in *Ninth International Conference on Intelligent Control and Information Processing (ICICIP)*, 2018, pp. 229–235. DOI: 10.1109/ICICIP.2018.8606668.

[64] J. Kalmari, H. Hyyti, and A. Visala, “Sway estimation using inertial measurement units for cranes with a rotating tool,” *IFAC Proceedings Volumes*, vol. 46, no. 10, pp. 274–279, 2013, 8th IFAC Symposium on Intelligent Autonomous Vehicles, ISSN: 1474-6670. DOI: 10.3182/20130626-3-AU-2035.00050.

[65] R. Fareh, M. R. Saad, M. Saad, A. Brahmi, and M. Bettayeb, “Trajectory tracking and stability analysis for mobile manipulators based on decentralized control,” *Robotica*, vol. 37, no. 10, pp. 1732–1749, 2019. DOI: 10.1017/S0263574719000225.

[66] J. Neupert, T. Mahl, B. Haessig, O. Sawodny, and K. Schneider, “A heave compensation approach for offshore cranes,” in *American Control Conference*, 2008, pp. 538–543. DOI: 10.1109/ACC.2008.4586547.

[67] D. Kim and Y. Park, “Tracking control in x-y plane of an offshore container crane,” *Journal of Vibration and Control*, vol. 23, no. 3, pp. 469–483, 2017. DOI: 10.1177/1077546315581091.

[68] C. Lee, S. Kwak, J. Kwak, and S. Oh, “Generalization of series elastic actuator configurations and dynamic behavior comparison,” *Actuators*, vol. 6, no. 3, 2017, ISSN: 2076-0825. DOI: 10.3390/act6030026.

[69] KUKA, *KUKA LBR iiwa*. 2022, accessed 23.6.2022, [Online]. Available: www.kuka.com/en-de/products/robot-systems/industrial-robots.

[70] Franka World, *Franka products*. 2022, accessed 23.6.2022. [Online]. Available: www.franka.de/production.

[71] G. A. Pratt and M. M. Williamson, "Series elastic actuators," in *Proceedings 1995 IEEE/RSJ International Conference on Intelligent Robots and Systems. Human Robot Interaction and Cooperative Robots*, IEEE, vol. 1, 1995, pp. 399–406. DOI: 10.1109/IROS.1995.525827.

[72] A. Albu-Schäffer, C. Ott, and G. Hirzinger, "A unified passivity-based control framework for position, torque and impedance control of flexible joint robots," *The international journal of robotics research*, vol. 26, no. 1, pp. 23–39, 2007. DOI: 10.1177/0278364907073776.

[73] A. Albu-Schäeffer, S. Haddadin, C. Ott, A. Stemmer, T. Wimböck, and G. Hirzinger, "The dlr lightweight robot – design and control concepts for robots in human environments," *Industrial Robot: an international journal*, vol. 34, pp. 376–385, Aug. 2007. DOI: 10.1108/01439910710774386.

[74] A. Albu-Schäfer, C. Ott, U. Frese, and G. Hirzinger, "Cartesian impedance control of redundant robots: Recent results with the dlr-light-weight-arms," in *International Conference on Robotics and Automation*, IEEE, vol. 3, 2003. DOI: 10.1109/ROBOT.2003.1242165.

[75] T. Chen, R. Casas, and P. S. Lum, "An elbow exoskeleton for upper limb rehabilitation with series elastic actuator and cable-driven differential," *IEEE Transactions on Robotics*, vol. 35, no. 6, pp. 1464–1474, 2019. DOI: 10.1109/TRO.2019.2930915.

[76] B. Lee, C. Knabe, V. Orekhov, and D. Hong, "Design of a human-like range of motion hip joint for humanoid robots," in *International Design Engineering Technical Conferences and Computers and Information in Engineering Conference*, ASME, 2014. DOI: 10.1115/DETC2014-35214.

[77] D. W. Robinson, J. E. Pratt, D. J. Paluska, and G. A. Pratt, "Series elastic actuator development for a biomimetic walking robot," in *IEEE/ASME International Conference on Advanced Intelligent Mechatronics*, IEEE, 1999, pp. 561–568. DOI: 10.1109/AIM.1999.803231.

[78] D. Budolak and P. Ben-Tzvi, "Series elastic actuation for improved transparency in time delayed haptic teleoperation," *Mechatronics*, vol. 63, 2019. DOI: 10.1016/j.mechatronics.2019.102278.

[79] J. Pratt, B. Krupp, and C. Morse, "Series elastic actuators for high fidelity force control," *Industrial Robot: An International Journal*, 2002. DOI: 10.1108/01439910210425522.

[80] J. E. Pratt and B. T. Krupp, "Series elastic actuators for legged robots," in *Unmanned Ground Vehicle Technology Vi*, International Society for Optics and Photonics, vol. 5422, 2004, pp. 135–144. DOI: 10.1117/12.548000.

[81] H. Kaminaga, S. Otsuki, and Y. Nakamura, "Development of high-power and backdrivable linear electro-hydrostatic actuator," in *International Conference on Humanoid Robots*, IEEE, 2014. DOI: 10.1109/HUMANOIDS.2014.7041481.

[82] X. Cao, M. M. Aref, and J. Mattila, "Design and control of a flexible joint as a hydraulic series elastic actuator for manipulation applications," in *IEEE International Conference on Cybernetics and Intelligent Systems (CIS) and IEEE Conference on Robotics, Automation and Mechatronics (RAM)*, IEEE, 2019, pp. 553–558. DOI: 10.1109/CIS-RAM47153.2019.9095773.

[83] H. Zhong, X. Li, L. Gao, and H. Dong, "Position control of hydraulic series elastic actuator with parameter self-optimization," in *4th International Conference on Advanced Robotics and Mechatronics (ICARM)*, 2019, pp. 42–46. DOI: 10.1109/ICARM.2019.8834216.

[84] H. Zhong, X. Li, and L. Gao, "Adaptive delay compensation for admittance control of hydraulic series elastic actuator," in *IEEE 16th International Conference on Automation Science and Engineering (CASE)*, 2020, pp. 384–389. DOI: 10.1109/CASE48305.2020.9216780.

[85] H. Zhong, X. Li, L. Gao, and H. Dong, "Development of admittance control method with parameter self-optimization for hydraulic series elastic actuator," *International Journal of Control, Automation and Systems*, vol. 19, no. 7, pp. 2357–2372, 2021. DOI: 10.1007/s12555-020-0465-y.

[86] Y. Zhao, N. Paine, S. J. Jorgensen, and L. Sentis, "Impedance control and performance measure of series elastic actuators," *IEEE Transactions on Industrial Electronics*, vol. 65, no. 3, pp. 2817–2827, 2017. DOI: 10.1109/TIE.2017.2745407.

[87] S. Oh and K. Kong, “High-precision robust force control of a series elastic actuator,” *IEEE/ASME Transactions on Mechatronics*, vol. 22, no. 1, pp. 71–80, 2016. DOI: 10.1109/TMECH.2016.2614503.

[88] A. Calanca and P. Fiorini, “Understanding environment-adaptive force control of series elastic actuators,” *IEEE/ASME Transactions on Mechatronics*, vol. 23, no. 1, pp. 413–423, 2018. DOI: 10.1109/TMECH.2018.2790350.

[89] N. Paine, S. Oh, and L. Sentis, “Design and control considerations for high-performance series elastic actuators,” *IEEE/ASME Transactions on Mechatronics*, vol. 19, no. 3, pp. 1080–1091, 2013. DOI: 10.1109/TMECH.2013.2270435.

[90] D. W. Robinson and G. A. Pratt, “Force controllable hydro-elastic actuator,” in *Proceedings 2000 ICRA. Millennium Conference. IEEE International Conference on Robotics and Automation. Symposia Proceedings*, IEEE, vol. 2, 2000, pp. 1321–1327. DOI: 10.1109/ROBOT.2000.844781.

[91] S. Kaixin, Z. Cong, C. YueHua, W. Jing, W. Qing, and M. HongXu, “Impedance control of hydraulic series elastic actuation,” in *Chinese Automation Congress*, 2020, pp. 2393–2398. DOI: 10.1109/CAC51589.2020.9327162.

[92] P. Mustalahti and J. Mattila, “Nonlinear full-model-based controller for unactuated joints in vertical plane,” pp. 201–206, 2017. DOI: 10.1109/ICCIS.2017.8274774.

PUBLICATIONS

PUBLICATION
I

Stability-Guaranteed Anti-Sway Controller Design for a Redundant Articulated Hydraulic Manipulator in the Vertical Plane

P. Mustalahti, J. Koivumäki, and J. Mattila

In *ASME/BATH 2017 Symposium on Fluid Power and Motion Control*, ASME, Oct. 2017
DOI: 10.1115/FPMC2017-4263

Proceedings of the 2017 ASME/Bath Symposium on Fluid Power and Motion Control
FPMC2017
October 16-19, 2017, Sarasota, FL, USA

FPMC2017-4263

STABILITY-GUARANTEED ANTI-SWAY CONTROLLER DESIGN FOR A REDUNDANT ARTICULATED HYDRAULIC MANIPULATOR IN THE VERTICAL PLANE

Pauli Mustalahti*, **Janne Koivumäki and Jouni Mattila**
Laboratory of Automation and Hydraulic Engineering
Tampere University of Technology
Tampere, Finland FI-33101
firstname.lastname@tut.fi

ABSTRACT

Articulated hydraulic manipulators are widely used for moving heavy loads. Commercial manipulators are most often equipped with a rotating load-grasping tool connected at the end of the manipulator via a pair of passive (unactuated) revolute joints. In free-space motion, these passive joints are subject to swaying motions due to the manipulator tip accelerations. Because these passive joints are not directly controllable due to their passive nature, a skilled driver is needed to compensate for the load swaying. In this paper, we extend the nonlinear model-based Virtual Decomposition Control (VDC) theory to cover anti-sway control of underactuated multiple degrees-of-freedom (DOF) hydraulic redundant manipulators. The proposed nonlinear controller performs the control design and stability analysis of the hydraulic robotic manipulator at the subsystem level. Experiments are conducted in a full-scale loader manipulator to verify that the proposed controller can efficiently damp the load swaying in a case study of redundant vertical plane motion.

1 INTRODUCTION

Articulated hydraulic manipulators are widely used in industry (e.g., in offshore, construction and forestry) to move heavy loads, such as containers, building materials and logs. Many of these commercial manipulators are equipped 1) with a rotating load-grasping tool connected at the end of the manipulator via pair of passive (unactuated) revolute joints or 2) with a lifting hook connected at the end of the manipulator by which the load is hoisted and freighted using lifting slings. In both cases, these passive joints are subject to sway in free-space motions due to the manipulator tip accelerations. For fluent system motions, a skilled and trained operator is needed to ensure safe load motions to prevent material (or even human) damage. However, it has been reported that the majority (73%) of all crane accidents originate from operator error [1].

The human operator workload and hoist operations safety can be improved by using automated operations, such as anti-sway control. In the bigger picture, the advent of robotics is expected to revolutionize the heavy-duty working machine industry as is currently happening in the car industry; discussion in [2]. This demands the development of new advanced control solutions for hydraulic heavy-duty working machines. However, one of the major challenges in closed-loop control of hydraulic articulated systems is their highly nonlinear dynamic behavior, which make the control design and stability analysis an extremely challenging task [2]. These hydraulic systems may be subjected to non-smooth and discontinuous nonlinearities (e.g., actuator friction, hysteresis, control input saturation, directional change of valve opening or valve under/overlap), and typically, many model and parameter uncertainties exist [3–6]. The control design of hydraulic manipulators is further complicated by the nonlinear nature of the associated multibody dynamics.

As demonstrated in a survey of the control of hydraulic robotic manipulators [2], stability-guaranteed nonlinear model-based (NMB) control methods can provide a superior control perfor-

---

*Address all correspondence to this author

mance in relation to other control methods. The need for NMB methods originates from the highly nonlinear dynamic nature of hydraulic manipulators. However, the majority of the proposed anti-sway control methods in the literature, e.g, [7–13], are still based on linear/linearized control methods, leading to limited control performance. Further, only a few anti-sway control methods for hydraulic manipulators have been verified with a full-scale experimental set-up [12–14]. A large harbor crane was used in [12], and in [13], an articulated three degrees-of-freedom (DOF) hydraulic manipulator was used. The only implemented nonlinear control method for anti-sway control of hydraulic manipulators is presented in [14] for a 4-DOF forestry crane. The method uses a nonlinear model predictive control, but it neglects, e.g., the associated multibody dynamics and the controller stability analysis. Thus, a stability-guaranteed NMB anti-sway control for hydraulic manipulators has remained an open problem.

This paper provides a solution for the above open problem. The proposed controller is designed by exploiting the control design principles of the Virtual Decomposition Control (VDC) approach (see [15, 16]), for which a number of significant state-of-the-art control performance improvements have already been reported with hydraulically-driven manipulators [17–21]. The inherent properties of VDC (subsystem-dynamics-based control design, the concept of *virtual stability* and *virtual power flows*) are used to design the controller, providing for the first time a rigorous stability proof in the category of anti-sway control of hydraulic manipulators. Experiments with a full-scale 5-DOF (three actuated joints and two unactuated joints) hydraulic manipulator demonstrate the validity of the proposed method; however, in the scope of this study, the manipulator's end-effector is driven only in a vertical plane.

This paper is organized as follows. Section 2 outlines the essential mathematical foundations for the control system. Section 3 introduces the basis of the VDC approach and the kinematics and dynamics relations of the studied system, followed by the corresponding control equation in Section 4. Section 5 gives a stability proof for the designed controller. Finally, experimental results are given in Section 6, and conclusions are outlined in Section 7.

2 MATHEMATICAL FOUNDATION

2.1 Velocity and Force/Moment Transformations

Assume that an orthogonal three-dimensional coordinate system $\{\mathbf{A}\}$ is fixed to the rigid body. Now, the linear/angular velocity vector of the frame $\{\mathbf{A}\}$ can be defined as ${}^{\mathbf{A}}V = [{}^{\mathbf{A}}\mathbf{v} \;\; {}^{\mathbf{A}}\omega]^T$, where ${}^{\mathbf{A}}\mathbf{v} \in \mathbb{R}^3$ are linear and ${}^{\mathbf{A}}\omega \in \mathbb{R}^3$ are the linear angular velocity vectors of frame $\{\mathbf{A}\}$. Furthermore, the force/moment vector in frame $\{\mathbf{A}\}$ can be written as ${}^{\mathbf{A}}F = [{}^{\mathbf{A}}\mathbf{f} \;\; {}^{\mathbf{A}}\mathbf{m}]^T$, where ${}^{\mathbf{A}}\mathbf{f} \in \mathbb{R}^3$ and ${}^{\mathbf{A}}\mathbf{m} \in \mathbb{R}^3$ are the force and moment vectors applied to the origin of frame $\{\mathbf{A}\}$. Thus, for two coordinate frames $\{\mathbf{A}\}$ and $\{\mathbf{B}\}$, which are fixed to a rigid body, the following relations hold

$$ {}^{\mathbf{B}}V = {}^{\mathbf{A}}\mathbf{U}_{\mathbf{B}}^{T}\,{}^{\mathbf{A}}V \tag{1} $$

$$ {}^{\mathbf{A}}F = {}^{\mathbf{A}}\mathbf{U}_{\mathbf{B}}\,{}^{\mathbf{B}}F \tag{2} $$

where ${}^{\mathbf{A}}\mathbf{U}_{\mathbf{B}} \in \mathbb{R}^{6\times 6}$ is a force/moment transformation matrix. This matrix transforms the measured and expressed force/moment vectors in frame $\{\mathbf{B}\}$ to the same measured and expressed force/moment vectors in frame $\{\mathbf{A}\}$.

Assume that frame $\{\mathbf{A}\}$ is fixed to the rigid body. Now, the dynamic equation in frame $\{\mathbf{A}\}$ can be defined as

$$ {}^{\mathbf{B}_1}F^* = \mathbf{M}_{\mathbf{B}_1}\frac{d}{dt}({}^{\mathbf{B}_1}V) + \mathbf{C}_{\mathbf{B}_1}({}^{\mathbf{B}_1}\omega)\,{}^{\mathbf{B}_1}V + \mathbf{G}_{\mathbf{B}_1} \tag{3} $$

where $\mathbf{M}_A \in \mathbb{R}^{6\times 6}$ is the mass matrix, $\mathbf{C}_{\mathbf{A}}({}^{\mathbf{A}}\omega) \in \mathbb{R}^{6\times 6}$ is the Coriolis and centrifugal terms, $\mathbf{G}_{\mathbf{A}} \in \mathbb{R}^6$ is the gravity vector and ${}^{\mathbf{A}}F^* \in \mathbb{R}^{6\times 6}$ is the net force/moment vector. The linear parametrization expression for the required rigid body dynamics can be presented as

$$ \mathbf{Y}_{\mathbf{B}_1}\theta_{\mathbf{B}_1} \overset{\text{def}}{=} \mathbf{M}_{\mathbf{B}_1}\frac{d}{dt}({}^{\mathbf{B}_1}V_{\mathrm{r}}) + \mathbf{C}_{\mathbf{B}_1}({}^{\mathbf{B}_1}\omega)\,{}^{\mathbf{B}_1}V_{\mathrm{r}} + \mathbf{G}_{\mathbf{B}_1}, \tag{4} $$

where detailed formulations for the regressor matrix $\mathbf{Y}_A \in \mathbb{R}^{6\times 13}$ and the parameter vector $\theta_{\mathbf{A}} \in \mathbb{R}^{13}$ are given in [16]. VDC allows parameter adaption for parameters in $\theta_{\mathbf{A}}$. However, parameter adaption is not used in this paper but it will be added in the future to the control equations.

2.2 L_2 and L_∞ Stability

The Lebesgue space is defined in Definition 1.

Definition 1 ([16]). *The Lebesgue space, denoted as L_p with p being a positive integer, contains all Lebesgue measurable and integrable functions $f(t)$ subject to*

$$ \|f\|_p = \lim_{T\to\infty}\left[\int_0^T |f(t)|^p d\tau\right]^{\frac{1}{p}} < +\infty \tag{5} $$

Two particular cases are considered:

(a) *A Lebesgue measurable function $f(t)$ belongs to L_2 if and only if $\lim_{T\to\infty}\int_0^T |f(t)|^2 d\tau < +\infty$.*

(b) *A Lebesgue measurable function $f(t)$ belongs to L_∞ if and only if $\max_{t\in[0,\infty)}|f(t)| < +\infty$.*

Then, Lemma 1 provides that a system is stable with its affiliated vector $\mathbf{x}(t)$, being a function in L_∞, and its affiliated vector $\mathbf{y}(t)$, being a function in L_2.

Lemma 1 ([16]). *Consider a non-negative differentiable function $\xi(t)$ defined as*

$$ \xi(t) \geqslant \frac{1}{2}\mathbf{x}(t)^T\mathbf{P}\mathbf{x}(t) \tag{6} $$

with $\mathbf{x}(t) \in \mathbb{R}^n$, $n \geqslant 1$ and $\mathbf{P} \in \mathbb{R}^{n\times n}$ a symmetric positive-definite matrix. If the time derivative of $\xi(t)$ is Lebesgue integrable and *governed by*

$$\dot{\xi}(t) \leqslant -\mathbf{y}(t)^T \mathbf{Q} \mathbf{y}(t) \tag{7}$$

where $\mathbf{y}(t) \in \mathbb{R}^m$, $m \geqslant 1$ *and* $\mathbf{Q} \in \mathbb{R}^{m \times m}$ *a symmetric positive definite matrix. Then, it follows that* $\xi(t) \in L_\infty$, $\mathbf{x}(t) \in L_\infty$ *and* $\mathbf{y}(t) \in L_2$ *hold.*

The following Lemma 2 provides that L_2 and L_∞ signal retains its properties after passing through a first-order filter.

Lemma 2 ([16]). *Consider a first-order system described by*

$$\dot{x}(t) + cx(t) = u(t) \tag{8}$$

with $c > 0$. *If* $u(t) \in L_p$ *holds, then* $x(t) \in L_p$ *and* $\dot{x}(t) \in L_p$ *hold for* $p = 2, \infty$.

2.3 Virtual Stability

In the VDC framework, the dynamic interactions among the subsystems are addressed with the scalar term, namely, the *virtual power flow* (VPF), defined in Definition 2.

Definition 2 ([16]). *The VPF with respect to frame* $\{A\}$ *can be defined as the inner product of the linear/angular velocity vector error and the force/moment vector error as*

$$p_{\mathbf{A}} = ({}^{\mathbf{A}}V_{\mathrm{r}} - {}^{\mathbf{A}}V)^T ({}^{\mathbf{A}}F_{\mathrm{r}} - {}^{\mathbf{A}}F) \tag{9}$$

where ${}^{\mathbf{A}}V_{\mathrm{r}} \in \mathbb{R}^6$ *and* ${}^{\mathbf{A}}F_{\mathrm{r}} \in \mathbb{R}^6$ *represent the required vectors of* ${}^{\mathbf{A}}V \in \mathbb{R}^6$ *and* ${}^{\mathbf{A}}F \in \mathbb{R}^6$, *respectively.*

Then, the virtual stability of the system is defined as shown in Definition 3.

Definition 3 ([16]). *A subsystem with a driven virtual cutting point (VCP) to which frame* $\{\mathbf{A}\}$ *is attached and a driving VCP to which frame* $\{\mathbf{C}\}$ *is attached is said to be virtually stable with its affiliated vector* $\mathbf{x}(t)$ *a virtual function in* L_∞ *and its affiliated vector* $\mathbf{y}(t)$ *a virtual function in* L_2, *if and only if there exists a non-negative accompanying function*

$$\nu(t) \geqslant \frac{1}{2}\mathbf{x}(t)^T \mathbf{P} \mathbf{x}(t) \tag{10}$$

so that

$$\dot{\nu}(t) \leqslant -\mathbf{y}(t)^T \mathbf{Q} \mathbf{y}(t) + p_{\mathbf{A}} - p_{\mathbf{C}} \tag{11}$$

holds, where $\mathbf{P}$ *and* $\mathbf{Q}$ *are two block-diagonal positive-definite matrices and* $p_{\mathbf{A}}$ *and* $p_{\mathbf{C}}$ *denote the VPFs (by Definition 2) at frames* $\{\mathbf{A}\}$ *and* $\{\mathbf{C}\}$, *respectively.*

3 KINEMATIC AND DYNAMIC MODELS FOR THE CONTROL DESIGN

In this study, the VDC approach is used as a framework to design an anti-sway control functionality for unactuated joints of a hydraulic manipulator. The VDC approach (see [15, 16]) is designed especially for controlling complex robotic systems. The fundamental idea behind VDC is to design the system control on subsystems dynamics (based on the *Newton-Euler dynamics*) instead of using the complete dynamics (based on the *Lagrange dynamics*). Thus, VDC can be described as a subsystem-dynamics-based control design method, which enables one to 1) design the system control locally at the subsystem level, and 2) perform the system stability analysis at the subsystem level; stability of control system is the primary requirement for all control systems [22]. One significant advantage of the VDC approach it that is has brought a certain type of modularity in the control system design engineering. For instance, it is possible to replace or add new subsystems to the original system without changing the control equations of the remaining subsystems.

Next, a vital part of the VDC approach is discussed, which is virtual decomposition of the studied 5-DOF hydraulic manipulator into subsystems. This section also addresses other vital parts of VDC, which are a simple oriented graph (SOG) presentation and a coordinate frame attachment into the decomposed subsystems. Then, the kinematic and dynamic relations are defined for the decomposed subsystems.

3.1 Virtual Decomposition, Simple Oriented Graph and Coordinate Frame Attachment

Fig. 1a shows the studied 5-DOF hydraulic manipulator. In total, four hydraulic actuators exist in the system: 1) cylinder-actuated pinion to slew the manipulator, 2) Cylinder 1 to lift the manipulator, 3) Cylinder 2 to tilt the manipulator and 4) Cylinder 3 to drive the telescopic boom. In addition, a gripper is attached to the end of manipulator tip with two unactuated joints (see Fig. 2), making the gripper sway freely in two dimensions. In the scope of this study, the cylinder-actuated pinion is not driven, making the manipulator for operating in a vertical plane. Note also that Cylinder 3 to operate the telecopic boom makes the system redundant.

In VDC, the first step is to virtually decompose the original system into subsystems, i.e., *objects* and *open chains*, by placing conceptual VCPs. Note that if *closed chain* structures exist in the system, they are further decomposed to *open chain* structures. A VCP is a directed separation interface that conceptually cuts through a rigid body and defines the reference direction for a six-dimensional force/moment vector. A VCP is simultaneously interpreted as a *driving* VCP by one subsystem (from which the force/moment vector is exerted) and as a *driven* VCP by another subsystem (to which the force/moment vector is exerted) [16]. The virtual decomposition of the system is given in Fig. 1b.

After the first step, the systems are presented by a SOG. In a SOG, each subsystem represents a node, and each VCP corresponds to a directed edge, which defines the reference direction for the force/moment vectors. No loop is allowed in a system

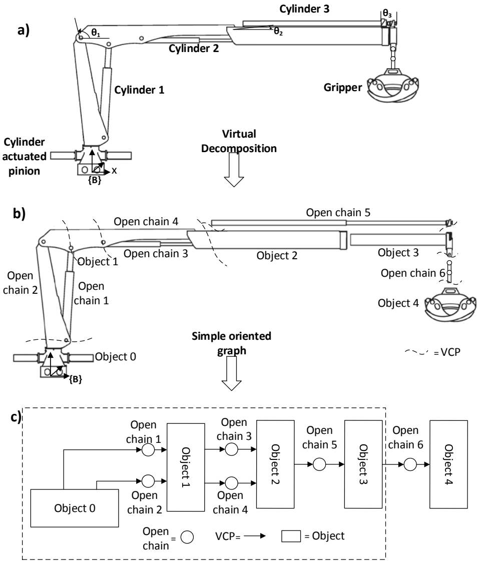

FIGURE 1. VIRTUAL DECOMPOSITION OF THE HYDRAULIC MANIPULATOR

SOG. The SOG for the manipulator is shown in Fig. 1c.

This paper designs the control laws only for the 6th *open chain* (composed of two unactuated joints with two rigid links) and for the 4th *object* (i.e., the gripper), shown in Fig. 2 and Fig. 3, respectively. The detailed control laws for the subsystems inside the dashed line in Fig. 1c (i.e., *objects* 0–3 and *open chains* 1–5) can be found in [19], where a VDC-based control is designed for a similar redundant hydraulic manipulator that does not have a gripper connected to two unactuated joints.

To describe the kinematics and dynamics relations of the subsystems, the fixed coordinate frames need to be attached to the rigid bodies. Fig. 2 shows the attached coordinate frames of the 6th *open chain*. The coordinate frames are attached so that in frames $\{\mathbf{B}_{60}\}$ and $\{\mathbf{B}_{61}\}$, denoted with red, the z-axle points out from *joint 1* and in frames $\{\mathbf{B}_{62}\}$, $\{\mathbf{B}_{63}\}$ and $\{\mathbf{B}_{64}\}$, denoted with blue, the z-axle points out from *joint 2*. Other axles are chosen by using the right-hand rule. This subsystem includes a VCP with the boom tip and with the 4th *object*. Because in hydraulic manipulator it is possible to use many different tools, in this paper, the gripper is modeled as an *object*. When the tool or load mass changes, only the modeling parameters of the 4th *object* need to change to correspond to the real system.

Fig. 3 illustrates the attached coordinate frames of the 4th *object*. The coordinate frames of the *object* follow from the 6th *open chains* coordinate frames. Therefore, in Fig. 3 the z-axle points out from the paper.

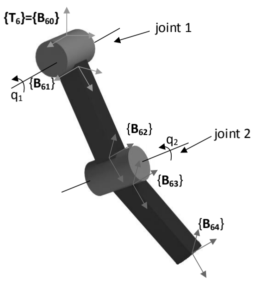

FIGURE 2. 6TH OPEN CHAIN

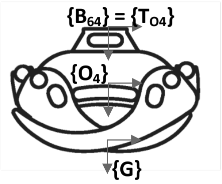

FIGURE 3. OBJECT 4

3.2 Kinematics of the 6th Open Chain

The linear/angular velocities at the VCPs of the studied *open chain* can be defined according to Eq. (1) and Fig. 2 as

$$ {}^{\mathbf{B}_{61}}V = {}^{\mathbf{B}_{60}}\mathbf{U}_{\mathbf{B}_{61}}^{T}\,{}^{\mathbf{B}_{60}}V + \mathbf{z}\dot{q}_1 \tag{12} $$

$$ {}^{\mathbf{B}_{62}}V = {}^{\mathbf{B}_{61}}\mathbf{U}_{\mathbf{B}_{62}}^{T}\,{}^{\mathbf{B}_{61}}V \tag{13} $$

$$ {}^{\mathbf{B}_{63}}V = {}^{\mathbf{B}_{62}}\mathbf{U}_{\mathbf{B}_{63}}^{T}\,{}^{\mathbf{B}_{62}}V + \mathbf{z}\dot{q}_2 \tag{14} $$

$$ {}^{\mathbf{B}_{64}}V = {}^{\mathbf{B}_{63}}\mathbf{U}_{\mathbf{B}_{64}}^{T}\,{}^{\mathbf{B}_{63}}V \tag{15} $$

where $\mathbf{z} = [0\;0\;0\;0\;0\;1]^T$.

3.3 Kinematics of the 4th Object

The linear/angular velocity vectors of 4th *object* can be defined according to Eq. (1) and Fig. 3 as

$$ {}^{\mathbf{O}_4}V = {}^{\mathbf{T}_{O4}}\,\mathbf{U}_{\mathbf{O}_4}^{T}\,{}^{\mathbf{T}_{O4}}V = {}^{\mathbf{G}}\,\mathbf{U}_{\mathbf{O}_4}^{T}\,{}^{\mathbf{G}}V \tag{16} $$

3.4 Dynamics of the 4th Object

In view of Eq. (3), the force/moment vector for the 4th *object* can be written as

$$ {}^{\mathbf{O}_4}F^* = \mathbf{M}_{\mathbf{O}_4}\frac{d}{dt}({}^{\mathbf{O}_4}V) + \mathbf{C}_{\mathbf{O}_4}({}^{\mathbf{O}_4}\omega)\,{}^{\mathbf{O}_4}V + \mathbf{G}_{\mathbf{O}_4} \tag{17} $$

On the other hand,

$$ {}^{\mathbf{O}_4}F^* = {}^{\mathbf{O}_4}\mathbf{U}_{\mathbf{T}_{O4}}\,{}^{\mathbf{T}_{O4}}F - {}^{\mathbf{O}_4}\mathbf{U}_{\mathbf{G}}\,{}^{\mathbf{G}}F \tag{18} $$

holds for the 4th *object*, where

$$ {}^{\mathbf{G}}\boldsymbol{F} = [0\;0\;0\;0\;0\;0]^T \tag{19} $$

holds for the external force vector ${}^{\mathbf{G}}\boldsymbol{F}$ in the free-space motions.

3.5 Dynamics of the 6th Open Chain

In view of Eq. 3, the dynamics of the two rigid links (link 61 and link 63) of the 6th *open chain* can be written as

$$ {}^{\mathbf{B}_{61}}F^* = \mathbf{M}_{\mathbf{B}_{61}} \frac{d}{dt}({}^{\mathbf{B}_{61}}V) + \mathbf{C}_{\mathbf{B}_{61}}({}^{\mathbf{B}_{61}}\omega){}^{\mathbf{B}_{61}}V + \mathbf{G}_{\mathbf{B}_{61}} \tag{20} $$

$$ {}^{\mathbf{B}_{63}}F^* = \mathbf{M}_{\mathbf{B}_{63}} \frac{d}{dt}({}^{\mathbf{B}_{63}}V) + \mathbf{C}_{\mathbf{B}_{63}}({}^{\mathbf{B}_{63}}\omega){}^{\mathbf{B}_{63}}V + \mathbf{G}_{\mathbf{B}_{63}} \tag{21} $$

Now the total force/moment vectors, which affect the frames, can be defined as

$$ {}^{\mathbf{B}_{63}}F = {}^{\mathbf{B}_{63}}F^* + {}^{\mathbf{B}_{63}}\mathbf{U}_{\mathbf{B}_{64}}\,{}^{\mathbf{B}_{64}}F \tag{22} $$

$$ {}^{\mathbf{B}_{62}}F = {}^{\mathbf{B}_{62}}\mathbf{U}_{\mathbf{B}_{63}}\,{}^{\mathbf{B}_{63}}F \tag{23} $$

$$ {}^{\mathbf{B}_{61}}F = {}^{\mathbf{B}_{61}}F^* + {}^{\mathbf{B}_{61}}\mathbf{U}_{\mathbf{B}_{62}}\,{}^{\mathbf{B}_{62}}F \tag{24} $$

$$ {}^{\mathbf{B}_{60}}F = {}^{\mathbf{B}_{60}}\mathbf{U}_{\mathbf{B}_{61}}\,{}^{\mathbf{B}_{61}}F \tag{25} $$

Both joints of the studied *open chain* are unactuated. In this paper, the following assumption is made.

Assumption 1. *The friction torques in the unactuated joints are zero.*

Then, using Assumption 1, the force constraints for the unactuated joints can be written as

$$ 0 = -\mathbf{z}^T\,{}^{\mathbf{B}_{6j}}F \tag{26} $$

where $j \in \{1,3\}$ is the order number of the coordinate frame.

4 CONTROL EQUATIONS FOR THE HYDRAULIC MANIPULATOR

This section defines the control equations for the 4th *object* and the 6th *open chain*. First, kinematics relations from desired the Cartesian motions to manipulator joint space motions are studied. Then, the required linear/angular velocities of the studied subsystems are presented. Finally, the required dynamics relations of the subsystems are given.

4.1 Inverse Kinematics of the Redundant Hydraulic Manipulator

Desired boom tip motions can be expressed by studying the kinematics relations between the Cartesian space and joint space motions (see Fig.1a) as

$$ \begin{bmatrix} \dot{X}_d \\ \dot{Y}_d \end{bmatrix} = \mathbf{J}\left[\dot\theta_{1d}\ \dot\theta_{2d}\ \dot\theta_{3d}\right]^T \tag{27} $$

where $\mathbf{J} \in \mathbb{R}^{2\times3}$ is the Jacobian matrix, $\dot{X}_d$ is the desired velocity of the Cartesian x-coordinate and $\dot{Y}_d$ is the desired velocity of the Cartesian y-coordinate. In Eq. (27), it is assumed that the joint space motions are defined, but usually the Cartesian space motions are defined in robotics. That is why the inverse kinematics of the manipulator need to be defined. If the manipulator is redundant, then an infinite number of joint velocities fulfill the given Cartesian velocity. However, inverse solution for Eq. (27) can be solved as

$$ \left[\dot\theta_{1d}\ \dot\theta_{2d}\ \dot\theta_{3d}\right]^T = \mathbf{J}_\mathbf{w}^* \begin{bmatrix} \dot{X}_d \\ \dot{Y}_d \end{bmatrix} \tag{28} $$

where $\mathbf{J}_W^* \in \mathbb{R}^{2\times3}$ is the weighted pseudoinverse solution, which can be defined as

$$ \mathbf{J}_\mathbf{w}^* = \mathbf{W}^{-1}\mathbf{J}^\mathbf{T}(\mathbf{J}\mathbf{W}^{-\mathbf{1}}\mathbf{J}^\mathbf{T})^{-1} \tag{29} $$

In Eq. (29), $\mathbf{W} \in \mathbb{R}^{3\times3}$ is the weighting matrix. In the literature, methods, such as [23, 24], for constructing the weighting matrix are presented. In this paper, a weighting matrix in [24], which minimizes the least-norm velocities of the joints, is used.

In VDC, the control objective is to make the controlled actual velocities track the required velocities. This can be performed either in the Cartesian space or in the joint space [16]. In this paper, the joint space approach is used. Using (28) and (29), the required joint space variables are designed similarly as demonstrated in [19] for a similar hydraulic crane.

The general format of a required velocity includes the a desired velocity (which usually serves as the reference trajectory for the system) and one or more terms that are related to control errors [16]. The required joint velocity for the ith unactuated joint, $\forall i \in \{1,2\}$, is designed as

$$ \dot{q}_{i\mathrm{r}} = \dot{q}_{i\mathrm{d}} + \lambda_i(q_{i\mathrm{d}} - q_i) \tag{30} $$

where λ_i is the position feedback gain for the joint and, to minimize the tool swaying, the desired joint velocity and the desired joint position are designed as $\dot{q}_{i\mathrm{d}} = 0$ rad/s and $q_{i\mathrm{d}} = 0$ rad, respectively.

4.2 Required Kinematics of the 6th Open Chain

The required linear/angular velocities at the coordinate frames of the studied *open chain* can be computed by reusing Eq. (12)-(15) as

$$ {}^{\mathbf{B}_{61}}V_r = \mathbf{z}\dot{q}_{1r} + {}^{\mathbf{B}_{60}}\mathbf{U}_{\mathbf{B}_{61}}^T\,{}^{\mathbf{B}_{60}}V_r \tag{31} $$

$$ {}^{\mathbf{B}_{62}}V_r = {}^{\mathbf{B}_{61}}\mathbf{U}_{\mathbf{B}_{62}}^T\,{}^{\mathbf{B}_{61}}V_r \tag{32} $$

$$ {}^{\mathbf{B}_{63}}V_r = \mathbf{z}\dot{q}_{2r} + {}^{\mathbf{B}_{62}}\mathbf{U}_{\mathbf{B}_{63}}^T\,{}^{\mathbf{B}_{62}}V_r \tag{33} $$

$$ {}^{\mathbf{B}_{64}}V_r = {}^{\mathbf{B}_{63}}\mathbf{U}_{\mathbf{B}_{64}}^T\,{}^{\mathbf{B}_{63}}V_r \tag{34} $$

4.3 Required Kinematics of the Object 4

The required kinematic of the 4th *object* can be defined by reusing Eq. (16) as

$$ {}^{\mathbf{O}_4}V_r = {}^{\mathbf{T}_{O4}}\mathbf{U}_{\mathbf{O}_4}^T\,{}^{\mathbf{T}_{O4}}V_r = {}^{\mathbf{G}}\mathbf{U}_{\mathbf{O}_4}^T\,{}^{\mathbf{G}}V_r \tag{35} $$

4.4 Required Dynamics of the Object 4

When the required linear/angular velocities for the studied subsystems are defined, the required net force/moment vectors

${}^{\mathbf{A}}F_r^* \in \mathbb{R}^6$ for the *object* and the *rigid links* can be defined in view of [16] as

$$ {}^{\mathbf{O}_4}F_r^* = \mathbf{Y_A}\theta_\mathbf{A} + K_\mathbf{A}({}^{\mathbf{A}}V_r - {}^{\mathbf{A}}V) \tag{36} $$

In Eq. (36), $K_\mathbf{A}$ is the velocity feedback control gain.

The required net force/moment vector of the 4th *object* can be presented by reusing Eq. (36) as

$$ {}^{\mathbf{O}_4}F_r^* = \mathbf{Y}_{\mathbf{O}_4}\theta_{\mathbf{O}_4} + \mathbf{K}_{\mathbf{O}_4}({}^{\mathbf{O}_4}V_r - {}^{\mathbf{O}_4}V) \tag{37} $$

In addition, the net force/moment vector in frame $\{\mathbf{T}_{\mathbf{O}_4}\}$ can be calculated by reusing Eq. (18) as

$$ {}^{\mathbf{T}_{O4}}F_r^* = {}^{\mathbf{T}_{O4}}\mathbf{U}_{\mathbf{O}_4}{}^{\mathbf{T}_{O4}}F_r - {}^{\mathbf{T}_{O4}}\mathbf{U}_\mathbf{G}{}^{\mathbf{G}}F_r \tag{38} $$

and, similar to (19), ${}^{\mathbf{G}}F_r$ is designed as

$$ {}^{\mathbf{G}}F_r = [0\,0\,0\,0\,0\,0]^T \tag{39} $$

4.5 Required Dynamics of the 6th Open Chain

When the required linear/angular velocities of the *open chain* are defined (Eq.(31)-(34)), the required net force/moment vectors of the rigid links in the 6th *open chain* can be solved by reusing Eq. (36) as

$$ {}^{\mathbf{B}_{61}}F_r^* = \mathbf{Y}_{\mathbf{B}_{61}}\theta_{\mathbf{B}_{61}} + \mathbf{K}_{\mathbf{B}_{61}}({}^{\mathbf{B}_{61}}V_r - {}^{\mathbf{B}_{61}}V) \tag{40} $$

$$ {}^{\mathbf{B}_{63}}F_r^* = \mathbf{Y}_{\mathbf{B}_{63}}\theta_{\mathbf{B}_{63}} + \mathbf{K}_{\mathbf{B}_{63}}({}^{\mathbf{B}_{63}}V_r - {}^{\mathbf{B}_{63}}V) \tag{41} $$

Now, the total required force/moment vectors can be presented as

$$ {}^{\mathbf{B}_{63}}F_r = {}^{\mathbf{B}_{63}}F_r^* + {}^{\mathbf{B}_{63}}\mathbf{U}_{\mathbf{B}_{64}}{}^{\mathbf{B}_{64}}F_r \tag{42} $$

$$ {}^{\mathbf{B}_{62}}F_r = {}^{\mathbf{B}_{62}}\mathbf{U}_{\mathbf{B}_{63}}{}^{\mathbf{B}_{63}}F_r \tag{43} $$

$$ {}^{\mathbf{B}_{61}}F_r = {}^{\mathbf{B}_{61}}F^* + {}^{\mathbf{B}_{61}}\mathbf{U}_{\mathbf{B}_{62}}{}^{\mathbf{B}_{62}}F_r \tag{44} $$

$$ {}^{\mathbf{B}_{60}}F_r = {}^{\mathbf{B}_{60}}\mathbf{U}_{\mathbf{B}_{61}}{}^{\mathbf{B}_{61}}F_r \tag{45} $$

Similar to (26), the required force constraints for the unactuated joints can be written as

$$ 0 = -\mathbf{z}^{T\,\mathbf{B}_{6j}}F_r \tag{46} $$

where $j \in \{1,3\}$ is the order number of the coordinate frame.

Remark 1. *The proposed overall control method is a twofold. First, the desired boom tip velocities are converted to the required joint space velocities (see Section 4.1), which are further needed to compute the required cylinder actuation forces; see [19]. Second, the required unactuated joint velocities in* (30) *are designed to perform the tool anti-sway functionality. Using the required velocities in* (30)*, the required force/moment vector* ${}^{\mathbf{B}_{60}}F_r$ *at the driving VCP of object 3 (i.e., the driven VCP of open chain 6) can be computed from the dynamics described by Eqs.* (31)–(45)*. Further, with the known "tool sway-optimizing"* ${}^{\mathbf{B}_{60}}F_r$*, the required "tool sway-optimizing" cylinder actuation forces can be computed similar to [19]. Eventually, the swaying damping in this control method is based on the force error in the hydraulic cylinder control equations.*

5 STABILITY ANALYSIS

This section addresses the virtual stability of the 6th *open chain* and the 4th *object*. The proof for the virtual stability of the remaining subsystem (see Fig.1c) is presented in [19] for a similar hydraulic crane. The stability of the entire system is proven in the last subsection.

5.1 Virtual Stability of the 4th Object

Theorem 1 ensures that the 4th *object* qualifies as *virtually stable* in the sense of Definition 3.

Theorem 1. *Consider the 4th object depicted in Fig. 3, described by Eqs.* (16)–(19)*, and combined with its control Eqs.* (35) *and* (37)–(39)*. Subject to the gripper free-space motion, this subsystem is virtually stable with its affiliated vector* ${}^{\mathbf{O}_4}V_r - {}^{\mathbf{O}_4}V$ *being a virtual function in* L_2 *and* L_∞ *in the sense of Definition 3*

Proof. Subtracting Eq. (17) from Eq. (37) yields

$$ \begin{aligned} {}^{\mathbf{O}_4}F_r^* - {}^{\mathbf{O}_4}F^* = {}& \mathbf{M}_{\mathbf{O}_4}\frac{d}{dt}({}^{\mathbf{O}_4}V_r - {}^{\mathbf{O}_4}V) + \mathbf{C}_{\mathbf{O}_4}({}^{\mathbf{O}_4}\omega)({}^{\mathbf{O}_4}V_r - {}^{\mathbf{O}_4}V) \\ & + \mathbf{K}_{\mathbf{O}_4}({}^{\mathbf{O}_4}V_r - {}^{\mathbf{O}_4}V) \end{aligned} \tag{47} $$

Further, the skew-symmetric property of $\mathbf{C}_{\mathbf{O}_4}({}^{\mathbf{O}_4}\omega)$ yields

$$ ({}^{\mathbf{O}_4}V_r - {}^{\mathbf{O}_4}V)^T\mathbf{C}({}^{\mathbf{O}_4}\omega)({}^{\mathbf{O}_4}V_r - {}^{\mathbf{O}_4}V) = 0 \tag{48} $$

Next, let the non-negative accompanying function for the 4th *object* be defined as

$$ \nu_{\mathbf{O}_4} = \frac{1}{2}({}^{\mathbf{O}_4}V_r - {}^{\mathbf{O}_4}V)^T\mathbf{M}_{\mathbf{O}_4}({}^{\mathbf{O}_4}V_r - {}^{\mathbf{O}_4}V) \tag{49} $$

Using Eqs. (47) and (48), the time derivative of (49) can be written as

$$ \begin{aligned} \dot{\nu}_{\mathbf{O}_4} &= ({}^{\mathbf{O}_4}V_r - {}^{\mathbf{O}_4}V)^T\mathbf{M}_{\mathbf{O}_4}\frac{d}{dt}({}^{\mathbf{O}_4}V_r - {}^{\mathbf{O}_4}V) \\ &= ({}^{\mathbf{O}_4}V_r - {}^{\mathbf{O}_4}V)^T\Big[({}^{\mathbf{O}_4}F_r^* - {}^{\mathbf{O}_4}F^*) - \mathbf{C}({}^{\mathbf{O}_4}\omega)({}^{\mathbf{O}_4}V_r - {}^{\mathbf{O}_4}V) \\ &\quad - \mathbf{K}_{\mathbf{O}_4}({}^{\mathbf{O}_4}V_r - {}^{\mathbf{O}_4}V)\Big] \\ &= -({}^{\mathbf{O}_4}V_r - {}^{\mathbf{O}_4}V)^T\mathbf{K}_{\mathbf{O}_4}({}^{\mathbf{O}_4}V_r - {}^{\mathbf{O}_4}V) \\ &\quad + ({}^{\mathbf{O}_4}V_r - {}^{\mathbf{O}_4}V)^T({}^{\mathbf{O}_4}F_r^* - {}^{\mathbf{O}_4}F^*) \end{aligned} \tag{50} $$

Using Definition 2 and Eqs. (16), (18), (19), (35), (38) and (39), the last term in (50) can be rewritten as

$$ \begin{aligned} & ({}^{\mathbf{O}_4}V_r - {}^{\mathbf{O}_4}V)^T({}^{\mathbf{O}_4}F_r^* - {}^{\mathbf{O}_4}F^*) \\ &\quad = ({}^{\mathbf{O}_4}V_r - {}^{\mathbf{O}_4}V)^{T\,\mathbf{O}_4}\mathbf{U}_{\mathbf{T}_{O4}}({}^{\mathbf{T}_{O4}}F_r - {}^{\mathbf{T}_{O4}}F) \\ &\quad\quad - ({}^{\mathbf{O}_4}V_r - {}^{\mathbf{O}_4}V)^{T\,\mathbf{O}_4}\mathbf{U}_\mathbf{G}({}^{\mathbf{G}}F_r - {}^{\mathbf{G}}F) \\ &\quad = \Big[{}^{\mathbf{O}_4}\mathbf{U}_{\mathbf{T}_{O4}}^T({}^{\mathbf{O}_4}V_r - {}^{\mathbf{O}_4}V)\Big]^T({}^{\mathbf{T}_{O4}}F_r - {}^{\mathbf{T}_{O4}}F) \\ &\quad = p_{\mathbf{T}_{O4}} \end{aligned} \tag{51} $$

Finally, substituting Eq. (51) into Eq. (50) yields

$$ \dot{\nu}_{\mathbf{O}_4} = -({}^{\mathbf{O}_4}V_r - {}^{\mathbf{O}_4}V)^T\mathbf{K}_{\mathbf{O}_4}({}^{\mathbf{O}_4}V_r - {}^{\mathbf{O}_4}V) + p_{\mathbf{T}_{04}} \tag{52} $$

Consider that the 4th *object* has one *driven* VCP associated with frame $\{\mathbf{T}_{O4}\}$. Then, using (49) and (52) completes the proof of the *virtual stability* of the 4th *object*, in the sense of Definition 3, ensuring that ${}^{\mathbf{O}_4}V_r - {}^{\mathbf{O}_4}V \in L_2 \bigcap L_\infty$. ■

5.2 Virtual Stability of the 6th Open Chain

Theorem 2 ensures that the 6th *open chain* qualifies as virtually stable in the sense of Definition 2.

Theorem 2. *Consider the 6th open chain, composed of two unactuated joints (joint 1 and joint 2) and two rigid links (link 61 and link 63), depicted in Fig. 2, described by Eqs.* (12)–(15) *and* (20)–(26)*, and with its control equations Eqs.* (31)–(34) *and* (40)–(46)*. This subsystem is virtually stable with its affiliated vector* ${}^{\mathbf{B}_{6j}}V_r - {}^{\mathbf{B}_{6j}}V, \forall j \in \{1,3\}$ *being a virtual function in* L_2 *and* L_∞ *in the sense of Definition 3.*

Proof. Let the non-negative accompanying functions $\nu_{\mathrm{oc}6}$ for the 6th *open chain* be

$$\nu_{\mathrm{oc}6} = \nu_{\mathbf{B}_{61}} + \nu_{\mathbf{B}_{63}} \tag{53}$$

where $\nu_{\mathbf{B}_{61}}$ and $\nu_{\mathbf{B}_{63}}$ denote the non-negative accompanying functions for the rigid links 61 and 63, respectively, and are defined as

$$\nu_{\mathbf{B}_{61}} = \frac{1}{2}({}^{\mathbf{B}_{61}}V_r - {}^{\mathbf{B}_{61}}V)^T \mathbf{M}_{\mathbf{B}_{61}} ({}^{\mathbf{B}_{61}}V_r - {}^{\mathbf{B}_{61}}V) \tag{54}$$

$$\nu_{\mathbf{B}_{63}} = \frac{1}{2}({}^{\mathbf{B}_{63}}V_r - {}^{\mathbf{B}_{63}}V)^T \mathbf{M}_{\mathbf{B}_{63}} ({}^{\mathbf{B}_{63}}V_r - {}^{\mathbf{B}_{63}}V) \tag{55}$$

Similar to Eqs. (47), (48) and (50), it can be easily shown that the time derivatives of $\nu_{\mathbf{B}_{61}}$ and $\nu_{\mathbf{B}_{63}}$ can be written as

$$\begin{aligned}\dot{\nu}_{\mathbf{B}_{61}} &= -({}^{\mathbf{B}_{61}}V_r - {}^{\mathbf{B}_{61}}V)^T \mathbf{K}_{\mathbf{B}_{61}} ({}^{\mathbf{B}_{61}}V_r - {}^{\mathbf{B}_{61}}V) \\ &\quad + ({}^{\mathbf{B}_{61}}V_r - {}^{\mathbf{B}_{61}}V)^T ({}^{\mathbf{B}_{61}}F_r^* - {}^{\mathbf{B}_{61}}F^*) \end{aligned} \tag{56}$$

$$\begin{aligned}\dot{\nu}_{\mathbf{B}_{63}} &= -({}^{\mathbf{B}_{63}}V_r - {}^{\mathbf{B}_{63}}V)^T \mathbf{K}_{\mathbf{B}_{63}} ({}^{\mathbf{B}_{63}}V_r - {}^{\mathbf{B}_{61}}V) \\ &\quad + ({}^{\mathbf{B}_{63}}V_r - {}^{\mathbf{B}_{63}}V)^T ({}^{\mathbf{B}_{63}}F_r^* - {}^{\mathbf{B}_{63}}F^*) \end{aligned} \tag{57}$$

using Eqs. (20), (21), (40) and (41).

Then, it follows from Definition 2 and Eqs. (12), (13), (24), (25), (26), (31), (32), (44), (45) and (46) that the last term in (56) can be expressed as

$$\begin{aligned}&({}^{\mathbf{B}_{61}}V_r - {}^{\mathbf{B}_{61}}V)^T ({}^{\mathbf{B}_{61}}F_r^* - {}^{\mathbf{B}_{61}}F^*) \\ &= ({}^{\mathbf{B}_{61}}V_r - {}^{\mathbf{B}_{61}}V)^T \left[({}^{\mathbf{B}_{61}}F_r - {}^{\mathbf{B}_{61}}F) - {}^{\mathbf{B}_{61}}\mathbf{U}_{\mathbf{B}_{62}}({}^{\mathbf{B}_{62}}F_r - {}^{\mathbf{B}_{62}}F)\right] \\ &= \left[{}^{\mathbf{B}_{60}}\mathbf{U}_{\mathbf{B}_{61}}^T({}^{\mathbf{B}_{60}}V_r - {}^{\mathbf{B}_{60}}V) + \mathbf{z}(\dot{q}_{1r} - \dot{q}_1)\right]^T ({}^{\mathbf{B}_{61}}F_r - {}^{\mathbf{B}_{61}}F) \\ &\quad - \left[{}^{\mathbf{B}_{61}}\mathbf{U}_{\mathbf{B}_{62}}^T({}^{\mathbf{B}_{61}}V_r - {}^{\mathbf{B}_{61}}V)\right]^T ({}^{\mathbf{B}_{62}}F_r - {}^{\mathbf{B}_{62}}F) \\ &= ({}^{\mathbf{B}_{60}}V_r - {}^{\mathbf{B}_{60}}V)^T\, {}^{\mathbf{B}_{60}}\mathbf{U}_{\mathbf{B}_{61}}({}^{\mathbf{B}_{61}}F_r - {}^{\mathbf{B}_{61}}F) \\ &\quad + (\dot{q}_{1r} - \dot{q}_1)\mathbf{z}^T({}^{\mathbf{B}_{61}}F_r - {}^{\mathbf{B}_{61}}F) \\ &\quad - ({}^{\mathbf{B}_{62}}V_r - {}^{\mathbf{B}_{62}}V)^T ({}^{\mathbf{B}_{62}}F_r - {}^{\mathbf{B}_{62}}F) \\ &= p_{\mathbf{B}_{60}} - p_{\mathbf{B}_{62}} \end{aligned} \tag{58}$$

Similar to (58), it follows from Definition 2 and Eqs. (14), (15), (22), (23), (26), (33), (34), (42), (43) and (46) that the last term in (57) can be expressed as

$$\begin{aligned}&({}^{\mathbf{B}_{63}}V_r - {}^{\mathbf{B}_{63}}V)^T ({}^{\mathbf{B}_{63}}F_r^* - {}^{\mathbf{B}_{63}}F^*) \\ &= ({}^{\mathbf{B}_{63}}V_r - {}^{\mathbf{B}_{63}}V)^T \left[({}^{\mathbf{B}_{63}}F_r - {}^{\mathbf{B}_{63}}F) - {}^{\mathbf{B}_{63}}\mathbf{U}_{\mathbf{B}_{64}}({}^{\mathbf{B}_{64}}F_r - {}^{\mathbf{B}_{64}}F)\right] \\ &= \left[{}^{\mathbf{B}_{62}}\mathbf{U}_{\mathbf{B}_{63}}^T({}^{\mathbf{B}_{62}}V_r - {}^{\mathbf{B}_{62}}V) + \mathbf{z}(\dot{q}_{2r} - \dot{q}_2)\right]^T ({}^{\mathbf{B}_{63}}F_r - {}^{\mathbf{B}_{63}}F) \\ &\quad - \left[{}^{\mathbf{B}_{63}}\mathbf{U}_{\mathbf{B}_{64}}^T({}^{\mathbf{B}_{63}}V_r - {}^{\mathbf{B}_{63}}V)\right]^T ({}^{\mathbf{B}_{64}}F_r - {}^{\mathbf{B}_{64}}F) \\ &= ({}^{\mathbf{B}_{62}}V_r - {}^{\mathbf{B}_{62}}V)^T\, {}^{\mathbf{B}_{62}}\mathbf{U}_{\mathbf{B}_{63}}({}^{\mathbf{B}_{63}}F_r - {}^{\mathbf{B}_{63}}F) \\ &\quad + (\dot{q}_{2r} - \dot{q}_2)\mathbf{z}^T({}^{\mathbf{B}_{63}}F_r - {}^{\mathbf{B}_{63}}F) \\ &\quad - ({}^{\mathbf{B}_{64}}V_r - {}^{\mathbf{B}_{64}}V)^T ({}^{\mathbf{B}_{64}}F_r - {}^{\mathbf{B}_{64}}F) \\ &= p_{\mathbf{B}_{62}} - p_{\mathbf{B}_{64}} \end{aligned} \tag{59}$$

Taking the time derivative from (53) and using Eqs. (56), (57), (58) and (59) yields

$$\begin{aligned}\dot{\nu}_{\mathrm{oc}6} &= \dot{\nu}_{\mathbf{B}_{61}} + \dot{\nu}_{\mathbf{B}_{63}} \\ &= -({}^{\mathbf{B}_{61}}V_r - {}^{\mathbf{B}_{61}}V)^T \mathbf{K}_{\mathbf{B}_{61}} ({}^{\mathbf{B}_{61}}V_r - {}^{\mathbf{B}_{61}}V) \\ &\quad -({}^{\mathbf{B}_{63}}V_r - {}^{\mathbf{B}_{63}}V)^T \mathbf{K}_{\mathbf{B}_{63}} ({}^{\mathbf{B}_{63}}V_r - {}^{\mathbf{B}_{61}}V) \\ &\quad + p_{\mathbf{B}_{60}} - p_{\mathbf{B}_{64}} \end{aligned} \tag{60}$$

Consider that the 6th *open chain* has one *driven* VCP associated with frame $\{\mathbf{B}_{60}\}$ and one *driving* VCP associated with frame $\{\mathbf{B}_{64}\}$. Using (53)–(55) and (60) completes the proof of the *virtual stability* of the 6th *open chain*, in the sense of Definition 3, ensuring that ${}^{\mathbf{B}_{6j}}V_r - {}^{\mathbf{B}_{6j}}V \in L_2 \bigcap L_\infty, \forall j \in \{1,3\}$. ■

5.3 Stability of the Entire System

As addressed in Theorem 2.1 in [16], the *virtual stability* of every subsystem ensures the L_2 and L_∞ stability of the entire system. This is because at every placed VCP, a negative VPF is connected to its corresponding positive VPF. Hence, VPFs function as "stability connectors" between subsystems and they cancel each other out at every VCP [16].

The stability of a similar system in relation to the remaining subsystem, shown inside the dashed line in Fig. 1(c), is proven in [19]. Thus, using the results in [19], the non-negative accompanying function and its time-derivative for the remaining subsystem can be written as

$$\begin{aligned}\nu_{\mathbf{R}} &= \frac{1}{2}\sum_{\mathbf{B}\in\Phi}({}^{\mathbf{B}}V_{\mathrm{r}} - {}^{\mathbf{B}}V)^T \mathbf{M}_{\mathbf{B}}({}^{\mathbf{B}}V_{\mathrm{r}} - {}^{\mathbf{B}}V) + \frac{1}{2\beta}\sum_{i=1}^{3}(f_{\mathrm{pr}i} - f_{\mathrm{p}i})^2 \\ &\geqslant 0 \end{aligned} \tag{61}$$

$$\begin{aligned}\dot{\nu}_{\mathbf{R}} &= -\sum_{\mathbf{B}\in\Phi}({}^{\mathbf{B}}V_{\mathrm{r}} - {}^{\mathbf{B}}V)^T \mathbf{K}_{\mathbf{B}}({}^{\mathbf{B}}V_{\mathrm{r}} - {}^{\mathbf{B}}V) \\ &\quad -\sum_{i=1}^{3}\frac{k_{\mathrm{f}i}}{k_{\mathrm{x}i}}(f_{\mathrm{pr}i} - f_{\mathrm{p}i})^2 - p_{\mathbf{T}_6} \\ &\leqslant -p_{\mathbf{T}_6} \end{aligned} \tag{62}$$

where set Φ contains rigid body frames for all the rigid links and objects in the remaining subsystem, $(f_{\mathrm{pr}i} - f_{\mathrm{p}i})$ is a local force feedback for the ith cylinder, β is a fluid bulk modulus, and $k_{\mathrm{f}i}, k_{\mathrm{x}i} > 0$ hold for the two feedback gains.

Theorem 3 ensures the stability of the entire system in view of Lemmas 1 and 2.

Theorem 3. *Let Eqs.* (61) *and* (62) *hold for the remaining subsystem depicted inside the dashed line in Fig. 1(c). Then, it follows directly from Theorems 1 and 2 that the entire system is stable in view of Lemmas 1 and 2.*

Proof. Due to the frame attachment (see Section 3 and Fig. 2), the VPF at the *driven* VCP and the *driving* VCP can be written as

$$p_{\mathbf{B}_{60}} = p_{\mathbf{T}_6} \tag{63}$$

$$p_{\mathbf{B}_{64}} = p_{\mathbf{T}_{\mathrm{O4}}} \tag{64}$$

In view of (49), (53), (54), (55) and (61), the non-negative accompanying function for the entire system can be written as

$$\begin{aligned} \nu_{\mathrm{tot}} &= \nu_{\mathbf{R}} + \nu_{\mathrm{oc6}} + \nu_{\mathbf{O}_4} \\ &\geqslant \frac{1}{2} \sum_{\mathbf{A} \in \Psi} ({}^{\mathbf{A}}V_{\mathrm{r}} - {}^{\mathbf{A}}V)^T \mathbf{M}_{\mathbf{A}} ({}^{\mathbf{A}}V_{\mathrm{r}} - {}^{\mathbf{A}}V) \end{aligned} \tag{65}$$

where set Ψ contains frames $\{\mathbf{B}_{61}\}$, $\{\mathbf{B}_{63}\}$ and $\{\mathbf{O}_4\}$. Then, it follows from (52), (60), and (62)–(64) that the time derivative of (65) can be written as

$$\begin{aligned} \dot{\nu}_{\mathrm{tot}} &= \dot{\nu}_{\mathbf{R}} + \dot{\nu}_{\mathrm{oc6}} + \dot{\nu}_{\mathbf{O}_4} \\ &\leqslant - \sum_{\mathbf{A} \in \Psi} ({}^{\mathbf{A}}V_{\mathrm{r}} - {}^{\mathbf{A}}V)^T \mathbf{A}_{\mathbf{A}} ({}^{\mathbf{A}}V_{\mathrm{r}} - {}^{\mathbf{A}}V) \end{aligned} \tag{66}$$

Then, using Lemma 1, (65) and (66) yields

$$({}^{\mathbf{A}}V_{\mathrm{r}} - {}^{\mathbf{A}}V) \in L_2 \bigcap L_\infty, \ \forall \{\mathbf{A}\} \in \Psi \tag{67}$$

Finally, in view of Eqs. (22)–(25), (42)–(45) and (67), it follows that $(\dot{q}_{i\mathrm{r}} - \dot{q}_i) \in L_2 \bigcap L_\infty$, $\forall i \in \{1,2\}$, which further yields that $(\dot{q}_{i\mathrm{d}} - \dot{q}_i) \in L_2 \bigcap L_\infty$ and $(q_{i\mathrm{d}} - q_i) \in L_2 \bigcap L_\infty$ hold, $\forall i \in \{1,2\}$, in view of (30) and Lemma 2. ■

6 EXPERIMENTAL RESULTS

In this section, the control performance of the proposed controller is demonstrated with a full-scale commersial HIAB 033 hydraulic manipulator (see Fig. 1a). In the experiments, the real-time control interface was implemented with a PowerPC-based dSpace DS1103. The controller sampling rate was set to 1000 Hz (T_s=0.001 s).[1] The hydraulic cylinders of the manipulator were controlled with NG6 size servo solenoid valves, with a nominal fluid flow rate of 40 l/min at Δp = 3.5 MPa per control notch. The size of the lift cylinder and the tilt cylinder was ϕ80/60 - 607, and the size of the extension cylinder was ϕ45/30 - 1350. The system supply pressure was set to 20 MPa. The manipulator joint angles were measured with Fraba Incremental encoders (16384 inc/rev). The system pressures (supply pressure and cylinder chamber pressures) were measured with a Druck PTX1400 pressure transmitter with an operating pressure range of 25 MPa. The gripper was connected at the end of manipulator with two unactuated rigid links, having lengths of l_1 = 0.13 m and l_2 = 0.21 m. The gripper was a Vahva B15 with mass 90 kg and with load mass 150 kg.

TABLE 1. VDC CONTROLLER FEEDBACK GAINS

Cylinder 1	Cylinder 2	Cylinder 3
$\lambda_{\mathrm{x}1}$ = 27.49 $[\frac{\mathrm{m}}{\mathrm{s}}]$	$\lambda_{\mathrm{x}2}$ = 31.5 $[\frac{\mathrm{m}}{\mathrm{s}}]$	$\lambda_{\mathrm{x}3}$ = 30.3 $[\frac{\mathrm{m}}{\mathrm{s}}]$
$k_{\mathrm{f}1}$ = $3 \cdot 10^{-6}$ $[\frac{\mathrm{m}^2}{\mathrm{Ns}}]$	$k_{\mathrm{f}2}$ = $1.3 \cdot 10^{-6}$ $[\frac{\mathrm{m}^2}{\mathrm{Ns}}]$	$k_{\mathrm{f}3}$ = $1 \cdot 10^{-8}$ $[\frac{\mathrm{m}^2}{\mathrm{Ns}}]$
$k_{\mathrm{x}1}$ = 0.03 [m]	$k_{\mathrm{x}2}$ = 0.043 [m]	$k_{\mathrm{x}3}$ = 0.022 [m]

Detailed control laws for the cylinders can be found in [19]. Table 1 shows the feedback gains for the hydraulic cylinders used in the present study, where $\lambda_{\mathrm{x}i}$, $k_{\mathrm{x}i}$ and $k_{\mathrm{f}i}$, $\forall i \in \{1,2,3\}$ denote the cylinder piston position, velocity and force feedback gains, respectively. The position feedback gains for the joint angles in Eq. (30) were λ_{61} = 13 and λ_{63} = 13.

In the experiments, the proposed anti-sway controller was tested in horizontal motion along the X-axis of the system base frame $\{\mathbf{B}\}$ (see Fig. 1), so that a freely swaying motion was produced for the first unactuated joint only. A point-to-point quintic reference trajectory was used for the manipulator tip motions. Fig. 4 shows the results in the gripper forward motion when its center of the mass was driven from 2.4 m to 2.8 m in 1.8 s. The solid line shows the desired position trajectory, the dashed line shows the results with the proposed anti-sway control, and the dotted line shows the results without any anti-sway control (the manipulator was driven with well-tuned p-control). The peak velocity in the ramp was approximately 0.4 m/s. As Fig. 4 shows, the anti-sway controller compensates the load swaying with a settling time (2% from final value) of 3 seconds. The corresponding settling time without the anti-sway control was approximately 7.5 seconds. Thus, approximately 2.5 times faster settling time of was obtained with the proposed anti-sway controller. The load overshoot with and without anti-sway control was almost the same.

Fig. 5 shows the results using the same reference path as in the first experiment, but the time between the beginning and the end points was reduced to 1.6 s. The peak velocity in the ramp was approximately 0.47 m/s. Now, the settling time with the proposed controller (the dashed line) was approximately 4 seconds, whereas without the anti-sway control (the dotted line) the settling time was approximately 10.5 seconds. By comparing

---

[1] In previous VDC studies [18–21], the controller turnaround time (the time to calculate the controller outputs from the inputs) was more than 2.8 ms, and the controller sample rates were 16 ms in [18] and 3 ms in [19–21]. The present study demonstrates that *it is possible to use sample rates even smaller than 1 ms* (in the proposed controller, the turnaround time is 0.35 ms) *in full-model based VDC controller implementation* with more efficient control code generation. In the nonlinear model predictive controller [14], the controller sample rate was 16 ms.

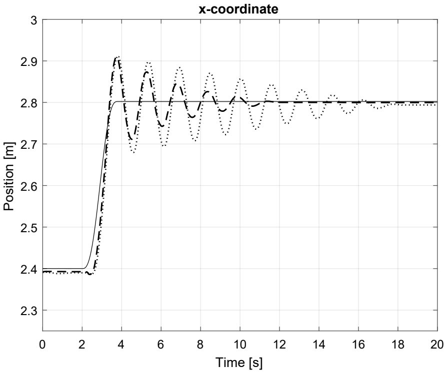

FIGURE 4. LOAD CENTER OF MASS POSITION WITH LOAD SWAY CONTROL AND WITHOUT LOAD SWAY CONTROL FOR 1.8 SECOND RAMP

the load settling in Figs. 4 and 5 shows that the longer transition time raises the settling time of the uncontrolled system from 7.5 to 10.5 seconds. Thus, approximately 2.65 times faster settling time of was obtained with the proposed anti-sway controller.

Fig. 6 shows the results in the gripper backward motion when its center of the mass was driven from 2.8 m to 2.4 m in 1.7 s. The peak velocity in the ramp was approximately 0.44 m/s peak velocity. The settling time of both systems was approximately 3 seconds. However, as this figure shows, the anti-sway controller (the dashed line) can still eliminate the gripper swaying much faster in relation to the controller without anti-sway (the dotted line). The load overshoot with the anti-sway controller is slightly higher in relation to the controller without anti-sway.

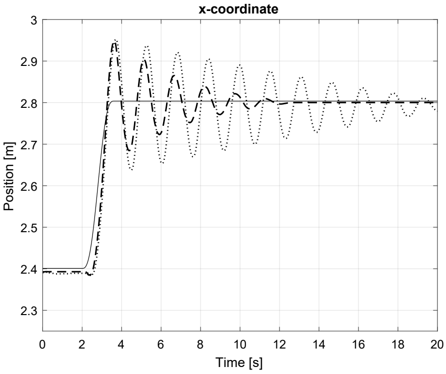

FIGURE 5. LOAD CENTER OF MASS POSITION WITH LOAD SWAY CONTROL AND WITHOUT LOAD SWAY CONTROL FOR 1.6 SECOND RAMP

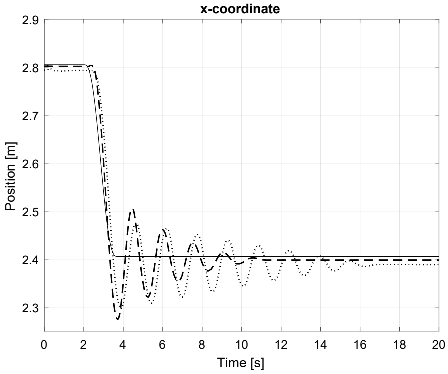

FIGURE 6. LOAD CENTER OF MASS POSITION WITH LOAD SWAY CONTROL AND WITHOUT LOAD SWAY CONTROL FOR 1.7 SECOND RAMP

7 CONCLUSIONS

This paper proposed, for the first time, a stability-guaranteed NMB controller for the anti-sway control of hydraulic manipulators, whose dynamic behavior is highly nonlinear. An anti-sway functionality for the unactuated joints were designed at the subsystem level (see Remark 1), which was enabled by the subsystem-dynamics-based VDC approach. The stability of the proposed controller was guaranteed in the rigorous stability analysis. The experiments with a full-scale hydraulic manipulator demonstrated in the vertical plane that the proposed novel anti-sway control method can damp the load swaying more than two times faster in relation to the control without anti-sway control.

The results of this study provided a baseline controller for our future studies, where, e.g., joint frictions of the unactuated joints and the unactuated *open chain* internal force vector will be studied in more detail. Furthermore, the proposed VDC-based controller also allows the incorporation of a parameter adaption for uncertain parameters, e.g., in friction dynamics, fluid dynamics and rigid body dynamics. As demonstrated in [17, 25], incorporation of a specific fast parameter adaptation law can significantly improve the control performance of highly nonlinear hydraulic systems. In future studies, the proposed controller will also be extended to compensate load swaying in all unactuated directions (not only in a vertical plane as in this paper).

ACKNOWLEDGMENT

This work was supported by the Academy of Finland under the project ”Strap-down sensing for safe material handling and high-performance motion control,” grant no.283171.

REFERENCES

[1] Lovgren, R., 2004. "Radical improvements in crane safety". *ISO focus,* ***1***(7), pp. 21–93.

[2] Mattila, J., Koivumäki, J., Caldwell, D. G., and Semini, C., 2017. "A survey on control of hydraulic robotic manipulators with projection to future trends". *IEEE/ASME Transactions on Mechatronics,* ***22***(2), pp. 669–680.

[3] Watton, J., 1989. *Fluid Power Systems: modelling, simulation, analog and microcomputer control*. Prentice Hall, New York.

[4] Edge, K., 1997. "The control of fluid power systems-responding to the challenges". *Proc. IMechE, Part I: Journal of Systems and Control Engineering,* ***211***(2), pp. 91–110.

[5] Yao, B., Bu, F., and Chiu, G. T., 2001. "Non-linear adaptive robust control of electro-hydraulic systems driven by double-rod actuators". *International Journal of Control,* ***74***(8), pp. 761–775.

[6] Mattila, J., and Virvalo, T., 2000. "Energy-efficient motion control of a hydraulic manipulator". In Robotics and Automation, 2000. Proceedings. ICRA'00. IEEE International Conference on, Vol. 3, IEEE, pp. 3000–3006.

[7] Palis, F., and Palis, S., 2010. "Modelling and anti-sway control of rotary cranes". In Power Electronics and Motion Control Conference (EPE/PEMC), 2010 14th International, IEEE, pp. T5–163.

[8] Ouyang, H., Zhang, G., Mei, L., Deng, X., and Wang, D., 2016. "Load vibration reduction in rotary cranes using robust two-degree-of-freedom control approach". *Advances in Mechanical Engineering,* ***8***(3), p. 1687814016641819.

[9] Uchiyama, N., 2009. "Robust control of rotary crane by partial-state feedback with integrator". *Mechatronics,* ***19***(8), pp. 1294–1302.

[10] Kjelland, M. B., Tyapin, I., Hovland, G., and Hansen, M. R., 2012. "Tool-point control for a redundant heave compensated hydraulic manipulator". In IFAC Workshop on Automatic Control in Offshore Oil and Gas Production, pp. 299–304.

[11] Kjelland, M. B., Hansen, M. R., Tyapin, I., and Hovland, G., 2012. "Tool-point control of a planar hydraulically actuated manipulator with compensation of non-actuated degree of freedom". In Proc. IEEE 12th Int. Conf. on Control, Automation and Systems (ICCAS), pp. 672–677.

[12] Neupert, J., Arnold, E., Schneider, K., and Sawodny, O., 2010. "Tracking and anti-sway control for boom cranes". *Control Engineering Practice,* ***18***(1), pp. 31–44.

[13] Honkakorpi, J., Vihonen, J., and Mattila, J., 2013. "Mems sensor network based anti-sway control system for articulated hydraulic crane". In ASME/BATH 2013 Symposium on Fluid Power and Motion Control, American Society of Mechanical Engineers, pp. 1–9.

[14] Kalmari, J., Backman, J., and Visala, A., 2014. "Nonlinear model predictive control of hydraulic forestry crane with automatic sway damping". *Computers and Electronics in Agriculture,* ***109***, pp. 36–45.

[15] Zhu, W.-H., Xi, Y.-G., Zhang, Z.-J., Bien, Z., and De Schutter, J., 1997. "Virtual decomposition based control for generalized high dimensional robotic systems with complicated structure". *IEEE Trans. Robot. Autom.,* ***13***(3), pp. 411–436.

[16] Zhu, W.-H., 2010. *Virtual decomposition control: toward hyper degrees of freedom robots*, Vol. 60. Springer Science & Business Media.

[17] Zhu, W.-H., and Piedboeuf, J.-C., 2005. "Adaptive output force tracking control of hydraulic cylinders with applications to robot manipulators". *Journal of dynamic systems, measurement, and control,* ***127***(2), pp. 206–217.

[18] Koivumäki, J., and Mattila, J., 2013. "The automation of multi degree of freedom hydraulic crane by using virtual decomposition control". In Advanced Intelligent Mechatronics (AIM), 2013 IEEE/ASME International Conference on, IEEE, pp. 912–919.

[19] Koivumäki, J., and Mattila, J., 2015. "High performance nonlinear motion/force controller design for redundant hydraulic construction crane automation". *Automation in Construction,* ***51***, pp. 59–77.

[20] Koivumäki, J., and Mattila, J., 2015. "Stability-guaranteed force-sensorless contact force/motion control of heavy-duty hydraulic manipulators". *IEEE Trans. Robotics,* ***31***(4), pp. 918–935.

[21] Koivumäki, J., and Mattila, J., 2017. "Stability-guaranteed impedance control of hydraulic robotic manipulators". *IEEE/ASME Trans. Mechatronics,* ***22***(2), pp. 601–612.

[22] Krstić, M., Kanellakopoulos, I., and Kokotović, P., 1995. *Nonlinear and Adaptive Control Design*. John Wiley & Sons, Inc.

[23] Beiner, L., and Mattila, J., 1999. "An improved pseudoinverse solution for redundant hydraulic manipulators". *Robotica,* ***17***(02), pp. 173–179.

[24] Chan, T. F., and Dubey, R. V., 1995. "A weighted least-norm solution based scheme for avoiding joint limits for redundant joint manipulators". *IEEE Transactions on Robotics and Automation,* ***11***(2), pp. 286–292.

[25] Koivumäki, J., and Mattila, J., 2017. "Adaptive and nonlinear control of discharge pressure for variable displacement axial piston pumps". *ASME J. Dyn. Syst., Meas., Control,* ***139***(10).

PUBLICATION
II

Nonlinear Model-Based Controller Design for a Hydraulic Rack and Pinion Gear Actuator

P. Mustalahti and J. Mattila

In *BATH/ASME 2018 Symposium on Fluid Power and Motion Control*, ASME, Sep. 2018
DOI: 10.1115/FPMC2018-8841

Proceedings of the 2018 ASME/Bath Symposium on Fluid Power and Motion Control
FPMC2018
September 12-14, 2018, University of Bath, Bath, United Kingdom

FPMC2018-8841

NONLINEAR MODEL-BASED CONTROLLER DESIGN FOR A HYDRAULIC RACK AND PINION GEAR ACTUATOR

Pauli Mustalahti* **and Jouni Mattila**
Laboratory of Automation and Hydraulic Engineering
Tampere University of Technology
Tampere, Finland FI-33101
firstname.lastname@tut.fi

ABSTRACT

Hydraulic manipulators are extensively utilized to move heavy loads in many industrial tasks. In commercial applications, a manipulator base is required to rotate a motion range of the full 360°. This is usually implemented by using a hydraulic rack and pinion gear actuator. Due to the manipulator's long reach and heavy loads, manipulator tip acceleration can produce significant torque to the rotation gear in free-space motion. Imposed by nonlinear dynamical behavior (involving, e.g., the gear backlash and actuator friction) added to high inertia, a system closed-loop control design becomes a challenging task. An advanced closed-loop control enables to increase the automation-level of hydraulic manipulators. This study designs a novel subsystem-dynamics-based controller for a hydraulic rack and pinion gear actuator utilizing the control design principles of the virtual decomposition control (VDC) approach. An adaptive backlash compensation is incorporated in the control design. Furthermore, the proposed controller is implemented in previously-designed state-of-the-art hydraulic manipulator control. The stability of the overall control design is proven. Experiments with a full-scale commercial hydraulic manipulator demonstrate the effectiveness of the proposed adaptive backlash compensation and the overall control performance.

1 INTRODUCTION

Hydraulic actuated articulated heavy-duty manipulators are used in many industrial domains to move heavy loads, such as logs, containers and building materials. A common feature of all these industrial domains is that humans are often working in the same area with the manipulators. In the conventional open-loop controlled approach, a human operator controls each manipulator joint separately with visual feedback. For this reason, a skilled and trained human operator is needed to ensure safe load motions and effective working [1].

The productivity and safety of hydraulic manipulators can be increased by automated operations. As reviewed in [2], robotic control of hydraulic manipulators is expected to revolutionize control of hydraulic manipulators similarly, as is currently happening in the car industry. The first robotic control solutions for heavy-duty manipulators are already available such as John Deere Forestry Intelligent Boom Control (IBC) and Cargotec Hiab Crane Tip Control (CTC) (see [3] and [4]). Effective robotic control requires the closed-loop control of the manipulator. Still, the high-performance closed-loop control design and stability analysis for these manipulators are challenging tasks [2], due to the highly nonlinear dynamical behavior of the hydraulic systems. In multiple degrees-of-freedom (DOF) manipulators, non-smooth non-linearities (e.g. actuator friction, gear backlash, hysteresis, and control input saturation) limit the control performance.

As demonstrated in [2], stability-guaranteed nonlinear model-based (NMB) control design methods outperform other control methods in the control of hydraulic manipulators. In previous studies [5–9], the virtual decomposition control (VDC) has been addressed to achieve state-of-the-art control performance with hydraulic cranes. However, these studies focused on desig-

---

*Address all correspondence to this author

ning in these studies are focusing to design control for hydraulic manipulators without the hydraulic manipulators' base rotations. This paper focusses on motion control of the base rotation which suffers from very low damping subject to only the high-inertia type of loading condition.

The wide working area of hydraulic manipulators requires a full motion range of 360° for the base rotation. For this reason, the base rotation in commercial rotary boom manipulators is often implemented by using a hydraulic rack and pinion gear actuator. High accelerations of heavy loads with manipulators' long reach produce significant torque on the rack and pinion gear actuator. Typically, this type of actuator also has a significant backlash with its dynamical behavior.

Backlash is common non-smooth nonlinearities, which limits the control performance. This non-linearity is encountered, for example, in mechanical gears in motors and in sensors. As discussed in [10], backlash modelling and compensation have been subjects to research for many years. In literature, many of the proposed backlash compensation methods [11–14] are adaptive control methods because the backlash parameters are often unknown. Usually, backlash compensation is implemented by adding the inverse of the backlash nonlinearity to control design.

The VDC approach control performance can be increased by adding incorporating backlash compensation into the control design, as demonstrated in [15] with a helical gear-type hydraulic rotary actuator. The backlash compensation in [15] is implemented by using discrete time backlash model [16], which is not optimal solution with a continuous time VDC approach. Furthermore, the stability analysis of the entire system is neglects.

In this study, a novel subsystem-dynamics-based control design is developed for the hydraulic rack and pinion gear actuator by using the control design principles of the VDC approach. Adaptive backlash compensation is incorporated into the control design, and as a novelty, the VDC approach is extended to cover the adaptive backlash compensation. The stability of the proposed controller with adaptive backlash compensation is guaranteed in the rigorous stability analysis.

This paper is organized as follows. Section 2 shows the mathematical background and notations for the proposed method. Section 3 introduces the main steps of the VDC approach. Furthermore, the kinematics and the dynamics equations for the hydraulic rack and pinion gear actuator are defined. Section 4 defines control equations for the studied gear system. Section 5 defines the adaptive backlash model equations. The stability analysis for the entire studied system is proven in Section 6. Finally, the experimental results are shown in Section 7, and conclusions are outlined in Section 8.

2 MATHEMATICAL BACKGROUND

In this section, the necessary mathematical notations of the VDC approach are presented.

Assume that a three-dimensional coordinate frame $\{\mathbf{A}\}$ is attached to the rigid body. Now, the linear/angular velocity vector in this coordinate frame can be written as ${}^{\mathbf{A}}V = [{}^{\mathbf{A}}\mathbf{v}\ {}^{\mathbf{A}}\omega]^T$, in view of [17]. In vector ${}^{\mathbf{A}}V$, ${}^{\mathbf{A}}\mathbf{v} \in \mathbb{R}^3$ denotes the linear velocity vector, and ${}^{\mathbf{A}}\omega \in \mathbb{R}^3$ denotes the angular velocity vector. Similarly, the force/moment vector, in coordinate frame $\{\mathbf{A}\}$, is a defined as a combination of a force vector ${}^{\mathbf{A}}\mathbf{f} \in \mathbb{R}^3$ and a moment vector ${}^{\mathbf{A}}\mathbf{m} \in \mathbb{R}^3$, as ${}^{\mathbf{A}}F = [{}^{\mathbf{A}}\mathbf{f}\ {}^{\mathbf{A}}\mathbf{m}]^T$. For the two fixed successive coordinate frames $\{\mathbf{A}\}$ and $\{\mathbf{B}\}$, the following relations hold:

$$ {}^{\mathbf{B}}V = {}^{\mathbf{A}}\mathbf{U}_{\mathbf{B}}^{T}\,{}^{\mathbf{A}}V \tag{1} $$

$$ {}^{\mathbf{A}}F = {}^{\mathbf{A}}\mathbf{U}_{\mathbf{B}}\,{}^{\mathbf{B}}F, \tag{2} $$

where ${}^{\mathbf{A}}\mathbf{U}_{\mathbf{B}} \in \mathbb{R}^{6\times 6}$ denotes the force/moment transformation between the two fixed coordinate frames.

Then, the dynamics in the coordinate frame $\{\mathbf{A}\}$ can be described as

$$ {}^{\mathbf{A}}F^{*} = \mathbf{M}_{\mathbf{A}}\frac{d}{dt}({}^{\mathbf{A}}V) + \mathbf{C}_{\mathbf{A}}({}^{\mathbf{A}}\omega){}^{\mathbf{A}}V + \mathbf{G}_{\mathbf{A}}, \tag{3} $$

where $\mathbf{M}_A \in \mathbb{R}^{6\times 6}$ is the mass matrix, $\mathbf{C}_{\mathbf{A}}({}^{\mathbf{A}}\omega) \in \mathbb{R}^{6\times 6}$ is the Coriolis and centrifugal terms, $\mathbf{G}_{\mathbf{A}} \in \mathbb{R}^6$ is the gravity vector, and ${}^{\mathbf{A}}F^{*} \in \mathbb{R}^6$ is the net force/moment vector.

As discussed in [17], the required rigid body dynamics can be written, by using the linear parametrization expression, as

$$ \mathbf{Y}_{\mathbf{A}}\theta_{\mathbf{A}} \overset{\text{def}}{=} \mathbf{M}_{\mathbf{A}}\frac{d}{dt}({}^{\mathbf{A}}V_{\mathrm{r}}) + \mathbf{C}_{\mathbf{A}}({}^{\mathbf{A}}\omega){}^{\mathbf{A}}V_{\mathrm{r}} + \mathbf{G}_{\mathbf{A}}, \tag{4} $$

where the parameter vector $\theta_{\mathbf{A}} \in \mathbb{R}^{13}$ and the regressor matrix $\mathbf{Y}_A \in \mathbb{R}^{6\times 13}$ are defined in more detail in [17]. The VDC approach enables also the parameter adaption for uncertain parameters in $\theta_{\mathbf{A}}$.

3 KINEMATICS AND DYNAMICS FOR THE RACK AND PINION GEAR ACTUATOR

In commercial heavy-duty hydraulic rotary boom manipulators, the boom rotation is implemented by using a hydraulic rack and pinion gear actuator. Usually, these gears consist of one or two hydraulic cylinders, which rotate the manipulator via the pinion gear. The working principle of this gear actuator is presented in Fig. 1 and in Fig. 2a, with one hydraulic cylinder. In this actuator, the cylinder is connected to the control valve as a symmetric cylinder. Due to the symmetry of the connection, the pinion rotation angle is zero, when the rotation cylinder is in the center position.

In this paper, the control for the hydraulic rack and pinion gear actuator is designed by using the VDC approach as a framework. This approach (see [17, 18]) provides subsystem-dynamics-based control method for multi-DOF complex robotic systems. The VDC approach allows also to perform stability analysis locally in the subsystem level. The VDC approach also enables the modular control design.

The following subsection presents the main steps of the VDC approach: 1) virtual decomposition of the 5-DOF hydraulic

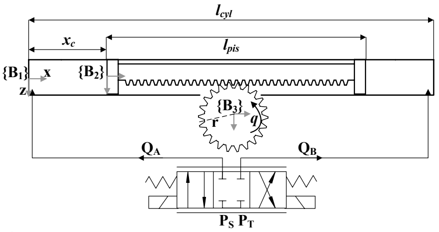

FIGURE 1. RACK AND PINION GEAR FROM ABOVE

manipulator, 2) simple oriented graph (SOG) presentation and 3) coordinate frame attachment to subsystems. Then, the kinematics and dynamics models for the hydraulic rack and pinion gear actuator are defined, and finally, the hydraulic cylinder dynamics equations are given.

3.1 Virtual Decomposition of the Entire System

Fig. 3a shows the 5-DOF hydraulic manipulator. The manipulator consists of four hydraulic cylinders: 1) Cylinder 1 to the hydraulic rack and pinion gear actuator, 2) Cylinder 2 to the lift manipulator, 3) Cylinder 3 to the tilt manipulator and 4) Cylinder 4 to extension. Also the gripper tool is connected at the manipulator tip via a pair of unactuated joints.

The first step of the VDC approach is virtually decompose the entire system into subsystems, which are *objects* and *open chains*, by placing virtual cutting points (VCPs). A VCP describes a separation the between successive subsystems by defining the direction for the force/moment in relation to these subsystems. One VCP is simultaneously interfered driving the VPC for one subsystem and driven for another subsystem. The driving VCP is the point from which the force/moment vector is exerted and the point to which the force/moment vector is exerted. Virtual decomposition for the entire system is given in Fig. 3b.

The main focus of this study is to design control equations for *open chain 1* (see Fig. 2a). The control equations for the similar redundant manipulator, without base rotation, are given in more detail in [5] (i.e. *open chains 2-6* and *objects 1-3*), and the control equations for the gripper with unactuated joints are given in [8] (i.e. *open chain 7* and *object 4*).

In a virtual decomposed system, the dynamics relations between successive subsystems can be presented by using a SOG (see Definition 2.14 in [17]). In an SOG, the force/moment direction is described by using a directed edge, and rigid links are presented as a node. The SOG for *open chain 1* is given in Fig. 2b (in dashed line). This *open chain* consists of a base rigid link and the first boom rigid link, which are connected to each other by the rotation gear.

For the kinematics and dynamics relations for the subsystems to be defined, the coordinate frames for the rigid links need to be fixed. The attached coordinate frames of *open chain 1* are shown in Fig. 1 and in Fig. 2a. The coordinate frames are attached so that the z-axle points out from the paper in Fig. 2a.

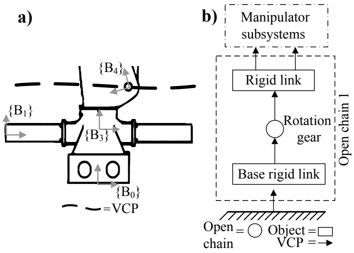

FIGURE 2. ROTATION OPEN CHAIN

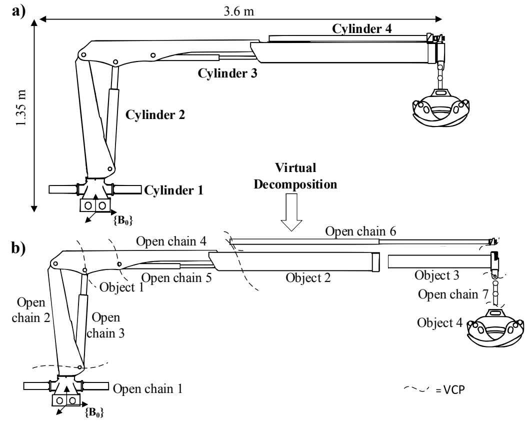

FIGURE 3. VIRTUAL DECOMPOSITION OF THE SYSTEM

3.2 Kinematics of the Rack and Pinion Gear

The linear/angular velocity vectors in the coordinate frames in Fig. 1 and Fig. 2a can be defined, by reusing Eq. (1), as

$$ {}^{\mathbf{B}_1}V = {}^{\mathbf{B}_1}\mathbf{U}_{\mathbf{B}_0}^{T}\,{}^{\mathbf{B}_0}V \tag{5} $$

$$ {}^{\mathbf{B}_2}V = {}^{\mathbf{B}_2}\mathbf{U}_{\mathbf{B}_1}^{T}\,{}^{\mathbf{B}_1}V + \mathbf{z}\dot{x}_c \tag{6} $$

$$ {}^{\mathbf{B}_3}V = {}^{\mathbf{B}_3}\mathbf{U}_{\mathbf{B}_0}^{T}\,{}^{\mathbf{B}_0}V + \mathbf{z}_\tau\dot{q} \tag{7} $$

$$ {}^{\mathbf{B}_4}V = {}^{\mathbf{B}_4}\mathbf{U}_{\mathbf{B}_3}^{T}\,{}^{\mathbf{B}_3}V \tag{8} $$

where $\mathbf{z} = [1\;0\;0\;0\;0\;0]^T$, $\mathbf{z}_\tau = [0\;0\;0\;0\;1\;0]^T$, $\dot{q}$ is a pinion angular velocity and $\dot{x}_c$ is the cylinder piston velocity. In Eq. (5), the linear/angular velocity, vector ${}^{\mathbf{B}_0}V = [0\;0\;0\;0\;0\;0]^T$, because in this paper the base frame position is fixed.

3.3 Dynamics of the Rack and Pinion Gear

The net force/moment vectors for *open chain 1* can be defined, by using Eq. (3), as

$$ {}^{\mathbf{B}_0}F^* = \mathbf{M}_{\mathbf{B}_0}\frac{d}{dt}({}^{\mathbf{B}_0}V) + \mathbf{C}_{\mathbf{B}_0}({}^{\mathbf{B}_0}\omega){}^{\mathbf{B}_0}V + \mathbf{G}_{\mathbf{B}_0} \tag{9} $$

$$ {}^{\mathbf{B}_2}F^* = \mathbf{M}_{\mathbf{B}_2}\frac{d}{dt}({}^{\mathbf{B}_2}V) + \mathbf{C}_{\mathbf{B}_2}({}^{\mathbf{B}_2}\omega){}^{\mathbf{B}_2}V + \mathbf{G}_{\mathbf{B}_2} \tag{10} $$

$$ {}^{\mathbf{B}_3}F^* = \mathbf{M}_{\mathbf{B}_3}\frac{d}{dt}({}^{\mathbf{B}_3}V) + \mathbf{C}_{\mathbf{B}_3}({}^{\mathbf{B}_3}\omega){}^{\mathbf{B}_3}V + \mathbf{G}_{\mathbf{B}_3} \tag{11} $$

When the net force/moment vectors are defined in Eqs. (9) and (11), the force/moment vectors for the *open chain* can be defined as

$$ {}^{\mathbf{B}_3}F = {}^{\mathbf{B}_3}F^* + {}^{\mathbf{B}_3}\mathbf{U}_{\mathbf{B}_4}{}^{\mathbf{B}_4}F \tag{12}$$

$$ {}^{\mathbf{B}_0}F = {}^{\mathbf{B}_0}F^* + {}^{\mathbf{B}_0}\mathbf{U}_{\mathbf{B}_3}{}^{\mathbf{B}_3}F \tag{13}$$

The rotation cylinder piston force in coordinate frame $\{\mathbf{B}_2\}$ can be calculated by using Eqs. (10) and (12) as

$$ f_c = \frac{1}{u_p}\mathbf{z}_\tau^T\,{}^{\mathbf{B}_3}F + \mathbf{z}^T\,{}^{\mathbf{B}_2}F^* \tag{14}$$

where $\mathbf{z} = [1\ 0\ 0\ 0\ 0\ 0]^T$, $\mathbf{z}_\tau = [0\ 0\ 0\ 0\ 1\ 0]^T$ and u_p is the gear ratio.

3.4 Dynamics Equations for the Hydraulic Cylinder

Consider the hydraulic cylinder and the servo control valve in Fig. 1. The defined cylinder piston force in Eq. (14) does not take into account the cylinder friction forces. So, the difference between the cylinder output force and the chamber pressure-induced piston force could be significant. For this reason, the cylinder force control performance can be approved by connecting a friction model for the piston force. Therefore, the chamber pressure-inducted piston force can be written as

$$ f_p = f_c + \mathbf{Y}_f\boldsymbol{\theta}_f \tag{15}$$

where $\mathbf{Y}_f\boldsymbol{\theta}_f \in \mathbb{R}$ denotes the linear parametrized piston friction model. The specifications of the friction model are given in more detail in [19].

Now, the pressure dynamics of the hydraulic cylinder can be written, in view of [17], as

$$ \dot{f}_p = \beta\left[u_f - \left(\frac{A_a}{x_c} + \frac{A_a}{l_0 - x_c}\right)\dot{x}_c\right] \tag{16}$$

where β is the effective bulk modulus, A_a is the cylinder area, x_c is the cylinder piston position, $\dot{x}_c$ is piston velocity and $l_0 = l_{cyl} - l_{pis}$ (see Fig. 1) is the maximum stroke of the cylinder. Also assumptions $x_c > 0$ and $l_0 - x_c > 0$ hold in Eq. (16). The hydraulic valve voltage-related term u_f can be defined as

$$ u_f = -\mathbf{Y}(u)\boldsymbol{\theta}_v \tag{17}$$

where the regressor vector is

$$ \mathbf{Y}_v = \begin{bmatrix} -\frac{\nu_{pr}(p_s-p_a)}{x_c}u\varepsilon(u) \\ -\frac{\nu_{pr}(p_a-p_t)}{x_c}u\varepsilon(-u) \\ -\frac{\nu_{pr}(p_s-p_b)}{x_c}u\varepsilon(-u) \\ -\frac{\nu_{pr}(p_b-p_t)}{x_c}u\varepsilon(u) \end{bmatrix}^T \in \mathbb{R}^{1\times 4} \tag{18}$$

and the valve flow coefficient parameter vector is

$$ \boldsymbol{\theta}_v = [c_{p1}\ c_{n1}\ c_{p2}\ c_{n2}]^T \in \mathbb{R}^4 \tag{19}$$

In Eqs. (17) and (18) valve dynamics can be neglected if high-bandwidth servo-valves are used. Switching function ε in Eq. (18) can be written as

$$ \varepsilon(x) = \begin{cases} 1 & \text{if } x > 0 \\ 0 & \text{if } x \leq 0 \end{cases} \tag{20}$$

Pressure-drop function ν_{pr} in Eq. (18) is defined as

$$ \nu_{pr}(x) = \sqrt{|x|}\operatorname{sign}(x) \tag{21}$$

where the sign function is defined as

$$ sign(x) = \begin{cases} 1 & \text{if } x > 0 \\ -1 & \text{if } x < 0 \\ 0 & \text{if } x = 0 \end{cases} \tag{22}$$

4 CONTROL EQUATION FOR THE HYDRAULIC RACK AND PINION GEAR ACTUATOR

In this section, the control equations for *open chain 1* are defined. First, the required linear/angular velocity vectors of the gear actuator are defined. Then, the required dynamics relations of the subsystem are given. Finally, the control equations for the hydraulic servo valve are presented.

4.1 Required Kinematics of the Rack and Pinion Gear

The required linear/angular velocity vectors of *open chain 1* can be defined, by reusing Eqs. (5)–(8), as

$$ {}^{\mathbf{B}_1}V_r = {}^{\mathbf{B}_1}\mathbf{U}_{\mathbf{B}_0}^T\,{}^{\mathbf{B}_0}V_r \tag{23}$$

$$ {}^{\mathbf{B}_2}V_r = {}^{\mathbf{B}_2}\mathbf{U}_{\mathbf{B}_1}^T\,{}^{\mathbf{B}_1}V_r + \mathbf{z}\dot{x}_{cr} \tag{24}$$

$$ {}^{\mathbf{B}_3}V_r = {}^{\mathbf{B}_3}\mathbf{U}_{\mathbf{B}_0}^T\,{}^{\mathbf{B}_0}V_r + \mathbf{z}_\tau\dot{q}_r \tag{25}$$

$$ {}^{\mathbf{B}_4}V_r = {}^{\mathbf{B}_4}\mathbf{U}_{\mathbf{B}_3}^T\,{}^{\mathbf{B}_3}V_r \tag{26}$$

where $\mathbf{z} = [1\ 0\ 0\ 0\ 0\ 0]^T$, $\mathbf{z}_\tau = [0\ 0\ 0\ 0\ 1\ 0]^T$, $\dot{q}_r$ is the required pinion angular velocity, and $\dot{x}_{cr}$ is the required cylinder piston velocity. Similar to Eq. (5), the base frame required linear/angular velocity vector is defined as ${}^{\mathbf{B}_0}V_r = [0\ 0\ 0\ 0\ 0\ 0]^T$.

4.2 Required Dynamics of the Rack and Pinion Gear

The required net force/moment vectors for *open chain 1* can be written, by using Eq. (4) and Eqs. (23)–(26), as

$$ {}^{\mathbf{B}_0}F_r^* = \mathbf{Y}_{\mathbf{B}_0}\widehat{\boldsymbol{\theta}}_{\mathbf{B}_0} + \mathbf{K}_{\mathbf{B}_0}({}^{\mathbf{B}_0}V_r - {}^{\mathbf{B}_0}V) \tag{27}$$

$$ {}^{\mathbf{B}_2}F_r^* = \mathbf{Y}_{\mathbf{B}_2}\widehat{\boldsymbol{\theta}}_{\mathbf{B}_2} + \mathbf{K}_{\mathbf{B}_2}({}^{\mathbf{B}_2}V_r - {}^{\mathbf{B}_2}V) \tag{28}$$

$$ {}^{\mathbf{B}_3}F_r^* = \mathbf{Y}_{\mathbf{B}_3}\widehat{\boldsymbol{\theta}}_{\mathbf{B}_3} + \mathbf{K}_{\mathbf{B}_3}({}^{\mathbf{B}_3}V_r - {}^{\mathbf{B}_3}V) \tag{29}$$

where $\mathbf{K}_{\mathbf{B}_0}$, $\mathbf{K}_{\mathbf{B}_2}$ and $\mathbf{K}_{\mathbf{B}_4}$ are the velocity feedback control gains. Vectors $\widehat{\boldsymbol{\theta}}_{\mathbf{B}_0}$, $\widehat{\boldsymbol{\theta}}_{\mathbf{B}_2}$ and $\widehat{\boldsymbol{\theta}}_{\mathbf{B}_4}$ denote the estimates of parameter vectors $\boldsymbol{\theta}_{\mathbf{B}_0}$, $\boldsymbol{\theta}_{\mathbf{B}_2}$ and $\boldsymbol{\theta}_{\mathbf{B}_4}$. In view of [17], the update of these vectors can be defined as

$$ \mathbf{s}_{\mathbf{B}_0} = \mathbf{Y}_{\mathbf{B}_0}^T({}^{\mathbf{B}_0}V_r - {}^{\mathbf{B}_0}V) \tag{30}$$

$$ \mathbf{s}_{\mathbf{B}_2} = \mathbf{Y}_{\mathbf{B}_2}^T({}^{\mathbf{B}_2}V_r - {}^{\mathbf{B}_2}V) \tag{31}$$

$$ \mathbf{s}_{\mathbf{B}_3} = \mathbf{Y}_{\mathbf{B}_3}^T({}^{\mathbf{B}_3}V_r - {}^{\mathbf{B}_3}V) \tag{32}$$

Then, the ith element of $\widehat{\theta}_{\mathbf{B}_j}$ can be updated, by using Definition 2.11 in [17], as

$$\widehat{\theta}_{\mathbf{B}_{ij}} = \mathscr{P}(s_{\mathbf{B}_{ij}}, \rho_{\mathbf{B}_{ij}}, \underline{\theta}_{\mathbf{B}_{ij}}, \overline{\theta}_{\mathbf{B}_{ij}}, t)\ \forall i \in \{1,2,\ldots,13\} \tag{33}$$

In Eq. (33), $\widehat{\theta}_{\mathbf{B}_{ij}}$ denotes the ith element of $\widehat{\theta}_{\mathbf{B}_j}$, $s_{\mathbf{B}_{ij}}$ denotes the ith element of $s_{\mathbf{B}_j}$, $\rho_{\mathbf{B}_{ij}} > 0$ is the update gain, $\underline{\theta}_{\mathbf{B}_{ij}}$ is the lower bound of $\theta_{\mathbf{B}_j}$, $\overline{\theta}_{\mathbf{B}_{ij}}$ is the upper bound of $\theta_{\mathbf{B}_j}$ and $j \in \{0,2,3\}$ is the order number of the coordinate frame.

When the net required force/moment vectors are defined in Eqs. (27) and (29), the force/moment vectors for *open chain 1* can be written as

$$^{\mathbf{B}_3}F_r = {}^{\mathbf{B}_3}F_r^* + {}^{\mathbf{B}_3}\mathbf{U}_{\mathbf{B}_4}\, {}^{\mathbf{B}_4}F_r \tag{34}$$

$$^{\mathbf{B}_0}F_r = {}^{\mathbf{B}_0}F_r^* + {}^{\mathbf{B}_0}\mathbf{U}_{\mathbf{B}_3}\, {}^{\mathbf{B}_3}F_r \tag{35}$$

The required cylinder piston force can be calculated by using Eqs. (28) and (34) as

$$f_{cr} = \frac{1}{u_p}\mathbf{z}_\tau^T\, {}^{\mathbf{B}_3}F_r + \mathbf{z}^T\, {}^{\mathbf{B}_2}F_r^* \tag{36}$$

where $\mathbf{z} = [1\ 0\ 0\ 0\ 0\ 0]^T$, $\mathbf{z}_\tau = [0\ 0\ 0\ 0\ 1\ 0]^T$ and u_p is the gear ratio.

4.3 Control Equations for the Hydraulic Cylinder

For the hydraulic servo valve (see Fig. 1), the unique control voltage u_v can be defined, in view of [17], as

$$\begin{aligned} u_v = {} & \frac{1}{\frac{c_{p1}\nu(p_s - p_a)}{x_c} + \frac{c_{n2}\nu(p_b - p_t)}{l_0 - x_c}} u_{fd}\varepsilon(u_{fd}) \\ & + \frac{1}{\frac{c_{n1}\nu(p_a - p_t)}{x_c} + \frac{c_{p2}\nu(p_s - p_b)}{l_0 - x_c}} u_{fd}\varepsilon(-u_{fd}) \end{aligned} \tag{37}$$

where assumptions $x_c > 0$ and $l_0 - x_c > 0$ holds for the hydraulic cylinder. In addition, it is assumed that for supply pressure p_s, tank pressure p_t and chamber pressures p_a and p_b, assumptions $p_s > p_a > p_t \geq 0$ and $p_s > p_b > p_t \geq 0$ hold.

The control valve control-voltage related term u_{fd} can be defined, by using the control laws for the hydraulic dynamics, as

$$\begin{aligned} u_{fd} = {} & \Big(\frac{1}{\widehat{\beta}}\Big)\dot{f}_{pr} + \Big(\frac{\widehat{A}_a}{x_c} + \frac{\widehat{A}_a}{l_0 - x_c}\Big)\dot{x}_c \\ & + K_f(f_{pr} - f_p) + K_x(\dot{x}_{cr} - \dot{x}_c) \\ = {} & \mathbf{Y}_c\widehat{\theta}_c + K_f(f_{pr} - f_p) + K_x(\dot{x}_{cr} - \dot{x}_c) \end{aligned} \tag{38}$$

where $K_f > 0$ and $K_x > 0$ are the feedback gains for the cylinder piston force and the cylinder piston velocity, l_0 is the maximum cylinder stroke, β is the effective bulk modulus, A_a is the cylinder area, $\widehat{\theta}_c$ is the estimation of parameter vector θ_c and

$$f_{pr} = f_{cr} + \mathbf{Y}_f\widehat{\theta}_f \tag{39}$$

$$\mathbf{Y}_c = \Big[\dot{f}_{pr}\ \frac{\dot{x}_c}{x_c}\ \frac{\dot{x}_c}{l_0 - x_c}\Big] \in \mathbb{R}^{1x3} \tag{40}$$

$$\widehat{\theta}_c = \Big[\frac{1}{\widehat{\beta}}\ \widehat{A}_a\ \widehat{A}_a\Big] \in \mathbb{R}^3 \tag{41}$$

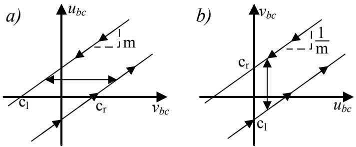

FIGURE 4. BACKLASH AND INVERSE BACKLASH MODEL

Here, f_{cr} is the required piston force, x_c is the cylinder piston position, its required counterpart is x_{cr}, $\dot{x}_c$ is the piston velocity and its required counterpart is $\dot{x}_{cr}$. $\mathbf{Y}_f\widehat{\theta}_f$ denotes the linear parametrized piston friction model, where $\widehat{\theta}_f$ is the estimation of parameter vector θ_f. Now, in view of [17], the hydraulic valve control voltage in Eq. (38) can be written inversely

$$u_{fd} = -\mathbf{Y}_v(u)\widehat{\theta}_v \tag{42}$$

where $\widehat{\theta}_v$ is the estimation of parameter vector θ_v.

Estimations for the parameter vectors in Eqs. (38), (39) and (42) can be updated, by reusing Eq. (30), as

$$\mathbf{s}_f = \mathbf{Y}_f^T(\dot{x}_{cr} - \dot{x}_c) \tag{43}$$

$$\mathbf{s}_d = \mathbf{Y}_d^T(f_{cr} - f_c) \tag{44}$$

$$\mathbf{s}_v = \mathbf{Y}_v^T(f_{cr} - f_c) \tag{45}$$

Now, the ith element of $\widehat{\theta}_f$, $\widehat{\theta}_d$ and $\widehat{\theta}_v$ can be updated, by reusing Eq. (33), as

$$\widehat{\theta}_{f_i} = \mathscr{P}(s_{f_i}, \rho_{f_i}, \underline{\theta}_{f_i}, \overline{\theta}_{f_i}, t)\ \forall i \in \{1,2,\ldots,7\} \tag{46}$$

$$\widehat{\theta}_{d_i} = \mathscr{P}(s_{d_i}, \rho_{d_i}, \underline{\theta}_{d_i}, \overline{\theta}_{d_i}, t)\ \forall i \in \{1,2,3\} \tag{47}$$

$$\widehat{\theta}_{v_i} = \mathscr{P}(s_{v_i}, \rho_{v_i}, \underline{\theta}_{v_i}, \overline{\theta}_{v_i}, t)\ \forall i \in \{1,2,3,4\} \tag{48}$$

where $\widehat{\theta}_{f_i}$, $\widehat{\theta}_{d_i}$ and $\widehat{\theta}_{v_i}$ denote the ith elements of θ_f, θ_d and θ_v respectively; s_{f_i}, s_{d_i} and s_{v_i} denote the ith element of $\mathbf{s}_f$, $\mathbf{s}_d$ and $\mathbf{s}_v$ respectively; $\rho_{f_i} > 0$, $\rho_{d_i} > 0$ and $\rho_{v_i} > 0$ are the update gains; $\underline{\theta}_{f_i}$, $\underline{\theta}_{d_i}$ and $\underline{\theta}_{v_i}$ are the lower bounds for θ_f, θ_d and θ_v, respectively $\overline{\theta}_{f_i}$, $\overline{\theta}_{d_i}$ and $\overline{\theta}_{v_i}$ are the lower bounds for θ_f, θ_d and θ_v, respectively.

5 ADAPTIVE BACKLASH INVERSE MODEL

This section presents a adaptive backlash inverse compensation. The parameter adaption for the unknown backlash parameters is given by using the VDC approach as a framework. As discussed in [17], this framework provides a rapid adaption law for the uncertain parameters. First, backlash model and its inverse are given. Then, a parameter adaption for the backlash is defined.

5.1 Backlash Model and Inverse Backlash Model

Backlash is a common non-smooth non-linearity in a mechanical gear transmission. Fig. 4a shows a simple backlash model, that consist of two parallel lines, which are connected to each other with a horizontal line. In the backlash model, the downwards line is active, when the backlash model input v_{bc} and the output

u_{bc} decrease. The upwards line is active, when v_{bc} and u_{bc} increase. In Fig. 4a, for The model left and right offset $c_r > c_l$ holds. Mathematically, a continuous time model for the backlash [11] can be written as

$$\dot{u}_{bc} = \begin{cases} m\dot{v}_{bc} & \dot{u}_{bc} > 0 \text{ and } u_{bc} = m(v_{bc} - c_r) \\ m\dot{v}_{bc} & \dot{u}_{bc} < 0 \text{ and } u_{bc} = m(v_{bc} - c_l) \\ 0 & \text{otherwise} \end{cases} \tag{49}$$

where m denotes the slope gain for the backlash (see Fig. 4a). As discussed in [11], the backlash model in Eq. (49) is also the first-order velocity-driven dynamic system. Therefore, the backlash model-desired input signals v_{bc} and $\dot{v}_{bc}$ generate unique output signals u_{bc} and $\dot{u}_{bc}$.

In closed-loop control, the backlash affects the control performance, because during the motion, the contact between the driving gear and the load gear shifts. One method for compensating the effects of the backlash in closed-loop control is to an inverse model for the backlash. In Fig. 4b the principle for the backlash inverse model is presented. Mathematically, the exact continuous time model for the backlash inverse [11] can be defined as

$$\dot{v}_{bc} = \begin{cases} \frac{\dot{u}_{tr}}{m} & \dot{u}_{tr} > 0 \text{ and } v_{bc} = \frac{u_{tr}}{m} + c_r \\ \frac{\dot{u}_{tr}}{m} & \dot{u}_{tr} < 0 \text{ and } v_{bc} = \frac{u_{tr}}{m} + c_l \\ 0 & \dot{u}_{tr} = 0 \\ g(\tau,t) & \dot{u}_{tr} > 0 \text{ and } v_{bc} = \frac{u_{tr}}{m} + c_l \\ -g(\tau,t) & \dot{u}_{tr} < 0 \text{ and } v_{bc} = \frac{u_{tr}}{m} + c_r \end{cases} \tag{50}$$

where $u_{tr} = u_{bc}$ and $\dot{u}_{tr} = \dot{u}_{bc}$ are the desired values for the backlash model output In Eq. (50) $\mathrm{g}(\tau,t) = \delta(\tau,t)(c_r - c_l)$ with $\delta(t)$ being the Dirac δ-function, which describes a vertical jump between c_r and c_l.

The backlash inverse model in Eq. (50) is also a first-order velocity-driven dynamic system, in view of [11]. Therefore, the backlash model-desired output signals u_{tr} and $\dot{u}_{tr}$ generate unique input signals v_{bc} and $\dot{v}_{bc}$. When the desired values for u_{tr} and $\dot{u}_{tr}$ are known, the backlash inverse model can be presented as

$$v_{bc} = \begin{cases} \frac{u_{tr}}{m} + c_r & \text{if } \dot{u}_{tr} > 0 \\ \frac{u_{tr}}{m} + c_l & \text{if } \dot{u}_{tr} < 0 \\ \frac{u_{tr}}{m} & \text{if } \dot{u}_{tr} = 0 \end{cases} \tag{51}$$

5.2 Adaptive Backlash Inverse Model

As Eqs. (49)–(51) show, the models for the backlash and its inverse are discontinuous, when the sign of $\dot{u}_{tr}$ will change. For this reason, if the time derivatives of v_{bc} and $\dot{v}_{bc}$ are needed in the control design, the discontinuous switching functions need to be replaced with continuous differentiable functions. First, the discontinuous switching function (see Eq. (22)) can be replaced with a continuous time switching function

$$\eta_c(x) = \frac{\tanh([x - x_o]/c\eta_c) + 1}{2} \tag{52}$$

where x_o is a sufficiently small offset constant parameter, and c_{η_c} is a sufficiently small constant. Another discontinuous switching function is form

$$\eta_{ds}(x) = \begin{cases} 1 & x = 0 \\ 0 & \text{otherwise} \end{cases} \tag{53}$$

Now, the discontinuous selective function can be replaced with continuous function

$$\eta_s(x) = 1 - \tanh(c_{\eta s}|x|) \tag{54}$$

where $c_{\eta s}$ is a sufficiently high constant value.

Usually, the backlash model parameters m, c_r and c_l are unknown [11]. For this reason, it is useful to replace these parameters with their estimates. Therefore, by using Eq. (52) the backlash inverse model in Eq. (51) can be rewritten as

$$\begin{aligned} v_{bc} &= \frac{u_{tr}}{\widehat{m}} + \widehat{c}_r \eta_c(\dot{u}_{tr}) + \widehat{c}_l \eta_c(-\dot{u}_{tr}) \\ &= [u_{tr}\ \eta_c(\dot{u}_{tr})\ \eta_c(-\dot{u}_{tr})] \left[\frac{1}{\widehat{m}}\ \widehat{c}_r\ \widehat{c}_l\right]^T \\ &= \mathbf{Y}_{bc}(\dot{u}_{tr})\widehat{\theta}_{bc}\ \in \mathbb{R} \end{aligned} \tag{55}$$

where $\widehat{m}$, $\widehat{c}_r$ and $\widehat{c}_l$ are estimates for backlash model parameters m, c_r and c_l. Similarly, the first-order velocity-driven backlash model, based on Eq. (49), can inversely written as

$$u_{bc} = \mathbf{Y}_{bc}(\dot{u}_{tr})\theta_{bc} \tag{56}$$

The estimations for parameters $\widehat{m}$, $\widehat{c}_r$ and $\widehat{c}_l$ can be updated, in view of [17], as

$$\mathbf{s}_{bc} = \mathbf{Y}_{bc}^T(\dot{u}_{tr})(\dot{u}_{tr} - \dot{u}) \tag{57}$$

where $\dot{u}_{tr}$ is the desired output velocity of the backlash model, and $\dot{u}$ is the measured velocity. Then, the ith element of $\widehat{\theta}_{bc}$ can be updated, by reusing Eq. (30), as

$$\widehat{\theta}_{bc_i} = \mathscr{P}(s_{bc_i}, \rho_{bc_i}, \underline{\theta}_{bc_i}, \overline{\theta}_{bc_i}, t)\ \forall i \in \{1,2,3\} \tag{58}$$

where $\widehat{\theta}_{bc_i}$ denotes the ith element of θ_{bc}, s_{bc_i} denotes the ith element of s_{bc}, $\rho_{bc} > 0$ is the update gain, $\underline{\theta}_{bc_i}$ is the lower bound for of $\theta_{bc}$and $\overline{\theta}_{bc_i}$ is the upper bound for of θ_{bc}.

When v_{bc} is calculated in Eq. (55), the backlash inverse velocity in Eq. (50) can be rewritten, by using Eqs. (52) and (54), as

$$\dot{v}_{bc} = \mathbf{Y}_{bv}(\dot{u}_{tr})\widehat{\theta}_{bv} \tag{59}$$

where

$$\mathbf{Y}_{bv}(\dot{u}_{tr}) = \left[\dot{u}_{tr}\eta_c(\dot{u}_{tr})\ \dot{u}_{tr}\eta_c(-\dot{u}_{tr})\ c_k\eta_c(\dot{u}_{tr})\ -c_k\eta_c(-\dot{u}_{tr})\right] \in \mathbb{R}^4 \tag{60}$$

and

$$\widehat{\theta}_{bv} = \begin{bmatrix} \frac{1}{\widehat{m}}\eta_s(v_{bc} - \frac{u_{tr}}{\widehat{m}} - \widehat{c}_r) \\ \frac{1}{\widehat{m}}\eta_s(v_{bc} - \frac{u_{tr}}{\widehat{m}} - \widehat{c}_l) \\ \eta_s(v_{bc} - \frac{u_{tr}}{\widehat{m}} - \widehat{c}_l) \\ \eta_s(v_{bc} - \frac{u_{tr}}{\widehat{m}} - \widehat{c}_r) \end{bmatrix} \in \mathbb{R}^4 \tag{61}$$

In Eq. (61), c_k is the boundary gain for the vertical jump between c_r and c_l.

Remark 1. *Consider that $\dot{v}_{bc}$ is a time derivation of v_{bc}. Therefore, the backlash model parameters m, c_r and c_l in Eqs.* (55) *and* (59) *should be correspond to each other. For this reason, the estimations for parameters $\widehat{m}$, $\widehat{c}_r$ and $\widehat{c}_l$ are updated by using Eq.* (58)*, and the same updated parameters are used in Eqs.* (55) *and* (61).

In this study, the adapted required pinion angular velocity can be defined by using Eqs. (55) and (59), in view of [17], as

$$\dot{q}_r = \mathbf{Y}_{bv}(\dot{u}_{tr})\widehat{\theta}_{bv} + \lambda(\mathbf{Y}_{bc}(\dot{u}_{tr})\widehat{\theta}_{bc} - q) \qquad (62)$$

where λ is the feedback gain for the angular position error, and q is the measured joint angle. According to Eq. (62), the required cylinder velocity can be calculated as

$$\dot{x}_{cr} = u_p \dot{q}_r \qquad (63)$$

where u_p is a gear ration.

6 STABILITY ANALYSIS FOR THE RACK AND PINION GEAR ACTUATOR

This section addresses the virtual stability analysis for *open chain 1* with parameter adaption and for the backlash model with parameter adaption. The stability analysis for the other subsystems (described in Fig. 3b) is presented in more detail in [5] and [8]. Finally, the stability analysis for the entire system is given.

6.1 Virtual Stability of the Rack and Pinion Gear

The virtual stability of *open chain 1* can be proved by considering Definition 2.17 in [17] and Theorem 1.

Theorem 1. *Let open chain 1 be composed of two rigid links and one actuated revolute joint, described in Fig. 2b, depicted by Eqs.* (5)–(14)*, and combined with its control Eqs.* (23)–(36)*. Studied subsystem is virtually stable with its affiliated vectors ${}^{\mathbf{B}j}V_r - {}^{\mathbf{B}j}V$, $\forall j \in \{0,3\}$ being a virtual function in L_2 and L_∞ in view of Definition 2.17 in [17]*

The non-negative accompanying function ν_{oc1} for *open chain 1* can be defined as

$$\nu_{\mathrm{oc1}} = \nu_{\mathbf{B}_0} + \nu_{\mathbf{B}_3} \qquad (64)$$

where $\nu_{\mathbf{B}_0}$ and $\nu_{\mathbf{B}_3}$ are the non-negative accompanying functions for the rigid bodies and are defined as

$$\begin{aligned}\nu_{\mathbf{B}_0} = {} & \frac{1}{2}({}^{\mathbf{B}0}V_r - {}^{\mathbf{B}0}V)^T \mathbf{M}_{\mathbf{B}_0}({}^{\mathbf{B}0}V_r - {}^{\mathbf{B}0}V) \\ & + \frac{1}{2}\sum_{i=1}^{13}\frac{(\theta_{\mathbf{B}_{0i}} - \widehat{\theta}_{\mathbf{B}_{0i}})^2}{\rho_{\mathbf{B}_{0i}}} \qquad (65)\\ \nu_{\mathbf{B}_3} = {} & \frac{1}{2}({}^{\mathbf{B}3}V_r - {}^{\mathbf{B}3}V)^T \mathbf{M}_{\mathbf{B}_3}({}^{\mathbf{B}3}V_r - {}^{\mathbf{B}3}V) \\ & + \frac{1}{2}\sum_{i=1}^{13}\frac{(\theta_{\mathbf{B}_{3i}} - \widehat{\theta}_{\mathbf{B}_{3i}})^2}{\rho_{\mathbf{B}_{3i}}} \qquad (66)\end{aligned}$$

Subtracting Eq. (9) from Eq. (27) yields

$$\begin{aligned}{}^{\mathbf{B}0}F_r^* - {}^{\mathbf{B}0}F^* = {} & \mathbf{M}_{\mathbf{B}_0}\frac{d}{dt}({}^{\mathbf{B}0}V_r - {}^{\mathbf{B}0}V) \qquad (67)\\ & + \mathbf{C}_{\mathbf{B}_0}({}^{\mathbf{B}0}\omega)({}^{\mathbf{B}0}V_r - {}^{\mathbf{B}0}V) + \mathbf{K}_{\mathbf{B}_0}({}^{\mathbf{B}0}V_r - {}^{\mathbf{B}0}V)\end{aligned}$$

Further, the skew-symmetric property of $\mathbf{C}_{\mathbf{B}_0}({}^{\mathbf{B}0}\omega)$ yields

$$({}^{\mathbf{B}0}V_r - {}^{\mathbf{B}0}V)^T \mathbf{C}({}^{\mathbf{B}0}\omega)({}^{\mathbf{B}0}V_r - {}^{\mathbf{B}0}V) = 0 \qquad (68)$$

The time derivative of $\nu_{\mathbf{B}_0}$ can be written, by differentiating Eq. (65), as

$$\begin{aligned}\dot{\nu}_{\mathbf{B}_0} \leq {} & ({}^{\mathbf{B}0}V_r - {}^{\mathbf{B}0}V)^T \mathbf{M}_{\mathbf{B}_0}\frac{d}{dt}({}^{\mathbf{B}0}V_r - {}^{\mathbf{B}0}V) \\ \leq {} & ({}^{\mathbf{B}0}V_r - {}^{\mathbf{B}0}V)^T \Big[({}^{\mathbf{B}0}F_r^* - {}^{\mathbf{B}0}F^*) \\ & - \mathbf{C}({}^{\mathbf{B}0}\omega)({}^{\mathbf{B}0}V_r - {}^{\mathbf{B}0}V) - \mathbf{K}_{\mathbf{B}_0}({}^{\mathbf{B}0}V_r - {}^{\mathbf{B}0}V)\Big] \\ \leq {} & -({}^{\mathbf{B}0}V_r - {}^{\mathbf{B}0}V)^T \mathbf{K}_{\mathbf{B}_0}({}^{\mathbf{B}0}V_r - {}^{\mathbf{B}0}V) \\ & + ({}^{\mathbf{B}0}V_r - {}^{\mathbf{B}0}V)^T({}^{\mathbf{B}0}F_r^* - {}^{\mathbf{B}0}F^*) \qquad (69)\end{aligned}$$

Similar, subtracting Eq. (11) from Eq. (29) yields

$$\begin{aligned}\dot{\nu}_{\mathbf{B}_3} \leq {} & -({}^{\mathbf{B}3}V_r - {}^{\mathbf{B}3}V)^T \mathbf{K}_{\mathbf{B}_3}({}^{\mathbf{B}3}V_r - {}^{\mathbf{B}3}V) \\ & + ({}^{\mathbf{B}3}V_r - {}^{\mathbf{B}3}V)^T({}^{\mathbf{B}3}F_r^* - {}^{\mathbf{B}3}F^*) \qquad (70)\end{aligned}$$

Now, according to Definition 2.16 in [17] and from Eqs. (5), (12), (14), (23), (34) and (36), that the last term of Eq. (69) can be expressed as

$$\begin{aligned}& ({}^{\mathbf{B}0}V_r - {}^{\mathbf{B}0}V)^T({}^{\mathbf{B}0}F_r^* - {}^{\mathbf{B}0}F^*) \\ & = ({}^{\mathbf{B}0}V_r - {}^{\mathbf{B}0}V)^T\Big[({}^{\mathbf{B}0}F_r - {}^{\mathbf{B}0}F) - {}^{\mathbf{B}0}\mathbf{U}_{\mathbf{B}_3}({}^{\mathbf{B}3}F_r - {}^{\mathbf{B}3}F)\Big] \\ & = p_{\mathbf{B}_0} - ({}^{\mathbf{B}0}V_r - {}^{\mathbf{B}0}V)^{T\,\mathbf{B}0}\mathbf{U}_{\mathbf{B}_3}({}^{\mathbf{B}3}F_r - {}^{\mathbf{B}3}F) \\ & = p_{\mathbf{B}_0} - ({}^{\mathbf{B}0}V_r - {}^{\mathbf{B}0}V)^{T\,\mathbf{B}0}\mathbf{U}_{\mathbf{B}_3}\Big[\mathbf{z}_\tau u_p(f_{cr} - f_c) \\ & \quad - \mathbf{z}_\tau u_p \mathbf{z}^T({}^{\mathbf{B}2}F_r^* - {}^{\mathbf{B}2}F^*)\Big] \\ & = p_{\mathbf{B}_0} - ({}^{\mathbf{B}0}V_r - {}^{\mathbf{B}0}V)^{T\,\mathbf{B}0}\mathbf{U}_{\mathbf{B}_3}\mathbf{z}_\tau u_p(f_{cr} - f_c) \qquad (71)\end{aligned}$$

where $p_{\mathbf{B}_0}$ is *virtual power flow* term, in view of Definition 2.16 in [17], for the base rigid link. Respectively, the last term of Eq. (70) can be written according to

Eqs. (7), (12), (14), (25), (34), (36) and (63), as

$$\begin{aligned}
&({}^{\mathbf{B}_3}V_r - {}^{\mathbf{B}_3}V)^T({}^{\mathbf{B}_3}F_r^* - {}^{\mathbf{B}_3}F^*) \\
&\quad = ({}^{\mathbf{B}_3}V_r - {}^{\mathbf{B}_3}V)^T\left[({}^{\mathbf{B}_3}F_r - {}^{\mathbf{B}_3}F) - {}^{\mathbf{B}_3}\mathbf{U}_{\mathbf{B}_4}({}^{\mathbf{B}_4}F_r - {}^{\mathbf{B}_4}F)\right] \\
&\quad = ({}^{\mathbf{B}_3}V_r - {}^{\mathbf{B}_3}V)^T({}^{\mathbf{B}_3}F_r - {}^{\mathbf{B}_3}F) - p_{\mathbf{B}_4} \\
&\quad = -p_{\mathbf{B}_4} + ({}^{\mathbf{B}_3}V_r - {}^{\mathbf{B}_3}V)^T(\mathbf{z}_\tau u_p(f_{cr} - f_c)) \\
&\quad = -p_{\mathbf{B}_4} + \left[{}^{\mathbf{B}_0}\mathbf{U}_{\mathbf{B}_3}^T({}^{\mathbf{B}_0}V_r - {}^{\mathbf{B}_0}V) + \mathbf{z}_\tau(\dot{q}_r - \dot{q})\right]^T \\
&\qquad \times \mathbf{z}_\tau u_p(f_{cr} - f_c) \\
&\quad = -p_{\mathbf{B}_4} + ({}^{\mathbf{B}_0}V_r - {}^{\mathbf{B}_0}V)^T\,{}^{\mathbf{B}_0}\mathbf{U}_{\mathbf{B}_3}\mathbf{z}_\tau u_p(f_{cr} - f_c) \\
&\qquad + (\dot{x}_{cr} - \dot{x})(f_{cr} - f_c) \qquad (72)
\end{aligned}$$

where $p_{\mathbf{B}_4}$ is *virtual power flow* term, for the manipulator rigid link.

Now, the time derivative of Eq. (64) can be written, by using Eqs. (69)–(72), as

$$\begin{aligned}
\dot{\nu}_{\mathrm{oc}1} &\leq \dot{\nu}_{\mathbf{B}_1} + \dot{\nu}_{\mathbf{B}_3} \\
&\leq -({}^{\mathbf{B}_0}V_r - {}^{\mathbf{B}_0}V)^T\mathbf{K}_{\mathbf{B}_0}({}^{\mathbf{B}_0}V_r - {}^{\mathbf{B}_0}V) \\
&\quad -({}^{\mathbf{B}_3}V_r - {}^{\mathbf{B}_3}V)^T\mathbf{K}_{\mathbf{B}_3}({}^{\mathbf{B}_3}V_r - {}^{\mathbf{B}_3}V) \\
&\quad +p_{\mathbf{B}_0} - p_{\mathbf{B}_4} + (\dot{x}_{cr} - \dot{x}_c)(f_{cr} - f_c) \qquad (73)
\end{aligned}$$

In Eq. (73), the appearance of $(\dot{x}_{cr} - \dot{x}_c)(f_{cr} - f_c)$ prevents the *virtual stability*. The virtual stability of *open chain 1* can be verified by considering Lemma 1.

Lemma 1. *Consider the hydraulic cylinder dynamics, defined in Eqs.* (15)–(17) *with control equations Eqs.* (37)–(41) *and with parameter adaption in Eqs.* (42)–(48).

Let the non-negative accompanying function for the cylinder dynamics be

$$\begin{aligned}
\nu_{cd} &= \frac{1}{2\beta}(f_{pr} - f_p)^2 + \frac{K_x}{2}\sum_{i=1}^{7}\frac{(\theta_{fi} - \widehat{\theta}_{fi})^2}{\rho_{fi}} \\
&\quad + \frac{1}{2}\sum_{i=1}^{3}\frac{(\theta_{ci} - \widehat{\theta}_{ci})^2}{\rho_{ci}} + \frac{1}{2}\sum_{i=1}^{4}\frac{(\theta_{vi} - \widehat{\theta}_{vi})^2}{\rho_{vi}} \qquad (74)
\end{aligned}$$

Now, the time derivative of Eq. (74) can be written as

$$\dot{\nu}_{cd} \leq -K_f(f_{pr} - f_p)^2 - K_x(\dot{x}_{cr} - \dot{x}_c)(f_{pr} - f_p) \qquad (75)$$

Proof for this Lemma is given in more detail in [6].

By using Lemma 1, Eq. (73) can be rewritten as

$$\begin{aligned}
\dot{\nu}_{\mathrm{oc}1} &\leq -({}^{\mathbf{B}_0}V_r - {}^{\mathbf{B}_0}V)^T\mathbf{K}_{\mathbf{B}_0}({}^{\mathbf{B}_0}V_r - {}^{\mathbf{B}_0}V) \\
&\quad -({}^{\mathbf{B}_3}V_r - {}^{\mathbf{B}_3}V)^T\mathbf{K}_{\mathbf{B}_3}({}^{\mathbf{B}_3}V_r - {}^{\mathbf{B}_3}V) \\
&\quad +p_{\mathbf{B}_0} - p_{\mathbf{B}_4} - \frac{K_f}{K_x}(f_{cr} - f_c)^2 \qquad (76)
\end{aligned}$$

As Fig. 2b shows, the *driving* VCP is fixed to frame $\{\mathbf{B}_4\}$ and the *driven* VCP is fixed to frame $\{\mathbf{B}_0\}$. Then, it follows from Eqs. (64)–(66) and (73) that the *virtual stability* of the *open chain 1* is ensured, in view of Definition 2.17 in [17], and that ${}^{\mathbf{B}_j}V_r - {}^{\mathbf{B}_j}V \in L_2 \bigcap L_\infty, \forall j \in \{0,3\}$. ■

6.2 Virtual Stability of the Adaptive Backlash Inverse

The virtual stability of the backlash model is ensured by using Theorem 2 and Definition 2.17 in [17].

Theorem 2. *Consider the inverse backlash model, described in Eqs.* (55), (56) *and* (62) *with parameter adaption in Eqs.* (57)–(58). *The backlash model is virtually stable with its affiliated vector* $(q_{tr} - q)$ *being a virtual function in* L_2 *and* L_∞ *in the sense of Definition 2.17 in [17]*

Let the non-negative accompanying function for the backlash model be

$$\nu_{bl} = \frac{1}{2}(q_{tr} - q)^2 + \sum_{i=1}^{3}\frac{(\theta_{bc} - \widehat{\theta}_{bc})^2}{\rho_{bci}} \qquad (77)$$

Now, the time derivation for the accompanying function can be written, according to Eqs. (55)–(58) and (62), in view of Definition 2.11 in [17] and Lemma 2.9 in [17], as

$$\begin{aligned}
\dot{\nu}_{bl} &= (q_{tr} - q)(\dot{q}_{tr} - \dot{q}) - \sum_{i=1}^{3}(\theta_{bc} - \widehat{\theta}_{bc})\frac{\dot{\widehat{\theta}}_{bc}}{\rho_{bci}} \\
&= -\lambda(q_{tr} - q)^2 + (q_{tr} - q)(\dot{q}_r - \dot{q}) - \sum_{i=1}^{3}(\theta_{bc} - \widehat{\theta}_{bc})\frac{\dot{\widehat{\theta}}_{bc}}{\rho_{bci}} \\
&= -\lambda(q_{tr} - q)^2 + \mathbf{Y}_{bc}(\theta_{bc} - \widehat{\theta}_{bc})(\dot{q}_r - \dot{q}) - \sum_{i=1}^{3}(\theta_{bc} - \widehat{\theta}_{bc})\frac{\dot{\widehat{\theta}}_{bc}}{\rho_{bci}} \\
&= -\lambda(q_{tr} - q)^2 + \sum_{i=1}^{3}(\theta_{bc} - \widehat{\theta}_{bc})\left(s_{bci} - \frac{\dot{\widehat{\theta}}_{bc}}{\rho_{bci}}\right) \\
&\leq -\lambda(q_{tr} - q)^2 \qquad (78)
\end{aligned}$$

The proposed backlash model is virtually stable with its affiliated vector $(q_{tr} - q)$ being a virtual function in L_2 and L_∞ in the sense of Definition 2.17 in [17]. ■

6.3 Stability of the Entire System

The entire system stability can be ensured, in view of Theorem 1 in [17], by analyzing the virtual stability of the subsystems. If all of the subsystems are proofed to virtual stable and if all of the VPF's are canceled out in the summation of the time derivative of all non-negative accompanying functions, in view of Lemma 2.3 in [17], the system is stable. The stability analysis for the gripper tool with the unactuated joints is given specific in [9], and the stability analysis for the manipulator subsystems (see Fig. 3b) is given specific in [5].

7 EXPERIMENTAL RESULTS

In this section, the control performance of the proposed controller with adaptive backlash compensation is demonstrate with a full-scale commercial Hiab 033 hydraulic manipulator (see Fig. 3a). The experimental setup for the hydraulic rack and pinion gear actuator consists of the next hardware components:

1. PowerPC-based dSpace ds1103 with a sample time of 1 ms
2. Bosch Rexroth NG6 size servo solenoid valve (12 l/min at $\Delta p = 3.5$ MPa per notch) for rotation cylinder
3. Rotation cylinder dimensions: ϕ80/60–607
4. MTS linear position sensor (range 0.5 m) for rotation cylinder
5. Druck PTX1400 pressure transmitter (range 25 MPa)
6. Fraba Incremental encoders (16384 inc/rev)
7. Gripper tool with mass 90 kg with load mass 150 kg

Other hardware components for the rest manipulator are listed in more detail in [8]. In the experiments, the manipulator rotation angle is measured by using an incremental encoder ,and the rotation cylinder position is calculated using measured joint angle. A linear position sensor for the rotation cylinder position is used to verify the gear backlash.

In the experiments, the proposed controller for the hydraulic rack and pinion gear actuator is tested by driving the rotation joint whilst the positions of the other manipulator joints are fixed. The reference trajectory for the rotation joint is designed by using a point-to-point quintic reference trajectory. The VDC controller gains, in the experiments are $\lambda = 5.259$ [m], $k_\mathrm{f} = 5.4{\cdot}10^{-8}$ $[\frac{\mathrm{m}^2}{\mathrm{Ns}}]$ and $k_\mathrm{x} = 0.036$ $[\frac{\mathrm{m}}{\mathrm{s}}]$.

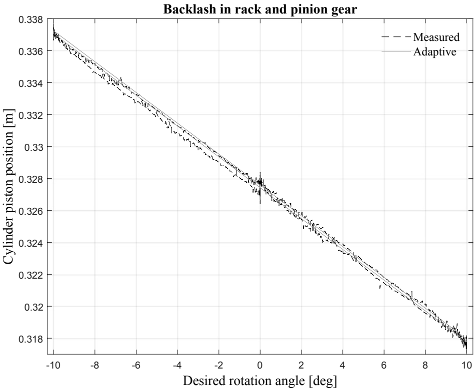

FIGURE 5. MEASURED BACKLASH OF THE GEAR

Fig. 5 presents the measured backlash of the rotation gear and the adapted backlash, when the required rotation gear moves from angle 0° to 10° and back and then to angle $-10°$ and back. The dashed line denotes the measured backlash, and the red line corresponds to the adapted backlash model. Fig. 5 shows that the proposed parameter adaption method for backlash model parameters produces efficient estimates for the unknown model parameters. The adapted parameters backlash parameters in this case are $\theta_{bc} = [0.993\ 0.0013\ -0.0014]$ after four working cycles when the initial parameter vector was set to $\theta_{bc} = [1\ 0.0\ 0.0]$.

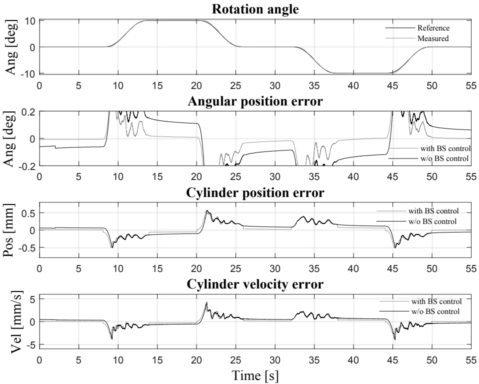

FIGURE 6. POSITION ERRORS AND VELOCITY ERROR

Fig. 6 presents the effect of the proposed controller with the backlash compensation compared to the controller without any compensation, with the same trajectory as in Fig. 5, and the time between the two point is 6 s. The black line denotes the control output without the backlash compensation, and red line denotes the controller with adaptive backlash compensation. Fig. 6 shows that the proposed backlash compensation in the control significantly decreases steady-state errors in the control system. Most significantly this can be detected in the rotation angle steady-state error, where the steady-state error without compensation is about 0.1°, and with compensation, the steady-state error is about 0.01°. As Fig. 6 shows the backlash compensation also enables a drive rotation from one angle to another repeatedly.

Fig. 7 presents the control results with the same trajectory as in Fig. 6, but the time between the two point is now reduced to 3 s. As Fig. 7 shows, the steady-state errors was equal to those in Fig. 6. As Fig. 7 shows also that the dynamic tracking errors increase only slightly.

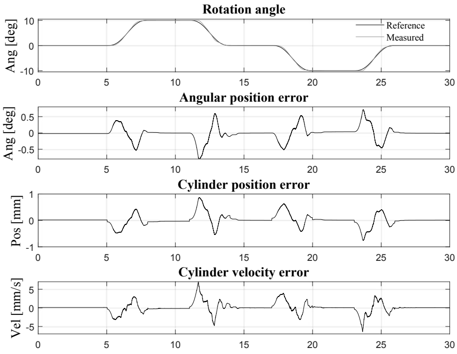

FIGURE 7. CYLINDER POSITION AND VELOCITY ERRORS FOR 3 SECOND RAMP

8 CONCLUSIONS

This paper proposed a stability-guaranteed NMB controller for the hydraulic rack and pinion gear actuator. In addition, this study extends the VDC approach to cover adaptive backlash compensation. The stability of the proposed controller with adaptive backlash compensation was guaranteed in the rigorous stability analysis. The experimental results with a full-size commercial hydraulic manipulator are d to verify the effectiveness of the proposed control method and the effectiveness of the proposed adaptive backlash compensation.

The proposed controller enables to extend the VDC approach, a current state-of-art with hydraulic manipulators, to cover rotary boom manipulator applications in future studies. In addition, the proposed backlash compensation method will be added to improve the control performance in other gear actuators in a multi-DOF hydraulic manipulator.

ACKNOWLEDGMENT

This work was supported by the Academy of Finland under the project ”Autonomous grasping and centralized multimodal human machine interface for multi-site heavy-duty working machines,” grant No. 304604.

REFERENCES

[1] Lovgren, R., 2004. “Radical improvements in crane safety”. *ISO focus,* ***1***(7), pp. 21–93.

[2] Mattila, J., Koivumäki, J., Caldwell, D. G., and Semini, C., 2017. “A survey on control of hydraulic robotic manipulators with projection to future trends”. *IEEE/ASME Trans. on Mechatronics,* ***22***(2), pp. 669–680.

[3] John Deere, 2013. *Intelligent Boom Control*. [online], accessed 14.6.2018, available: https://www.deere.co.uk/en/forestry/ibc/.

[4] HIAB, 2018. *Crane Tip Control*. [online], accessed 14.6.2018, available: https://www.hiab.com/en/HIAB/why-choose-hiab2/why-choose-hiab/features-and-benefits/hiab-crane-tip-control/.

[5] Koivumäki, J., and Mattila, J., 2015. “High performance nonlinear motion/force controller design for redundant hydraulic construction crane automation”. *Automation in Construction,* ***51***, pp. 59–77.

[6] Koivumäki, J., and Mattila, J., 2015. “Stability-guaranteed force-sensorless contact force/motion control of heavy-duty hydraulic manipulators”. *IEEE Trans. Robotics,* ***31***(4), pp. 918–935.

[7] Koivumäki, J., and Mattila, J., 2017. “Stability-guaranteed impedance control of hydraulic robotic manipulators”. *IEEE/ASME Trans. on Mechatronics,* ***22***(2), pp. 601–612.

[8] Mustalahti, P., and Mattila, J., 2017. “Nonlinear full-model-based controller for unactuated joints in vertical plane”. In Cybernetics and Intelligent Systems and Conference on Robotics, Automation and Mechatronics, IEEE, pp. 201–206.

[9] Mustalahti, P., Koivumäki, J., and Mattila, J., 2017. “Stability-guaranteed anti-sway controller design for a redundant articulated hydraulic manipulator in the vertical plane”. In ASME/BATH Symp. on Fluid Power and Motion Control, ASME, pp. V001T01A031–V001T01A031.

[10] Nordin, M., and Gutman, P.-O., 2002. “Controlling mechanical systems with backlash—a survey”. *Automatica,* ***38***(10), pp. 1633–1649.

[11] Tao, G., and Kokotovic, P. V., 1995. “Continuous-time adaptive control of systems with unknown backlash”. *IEEE Transactions on Automatic Control,* ***40***(6), pp. 1083–1087.

[12] Zhou, J., and Wen, C., 2008. *Adaptive backstepping control of uncertain systems: Nonsmooth nonlinearities, interactions or time-variations*. Springer.

[13] Lai, G., Liu, Z., Zhang, Y., Chen, C. P., and Xie, S., 2017. “Adaptive inversion-based fuzzy compensation control of uncertain pure-feedback systems with asymmetric actuator backlash”. *IEEE Trans. on Fuzzy Systems,* ***25***(1), pp. 141–155.

[14] He, W., Amoateng, D. O., Yang, C., and Gong, D., 2016. “Adaptive neural network control of a robotic manipulator with unknown backlash-like hysteresis”. *IET Control Theory & Applications,* ***11***(4), pp. 567–575.

[15] Adeyemi, A., and Mattila, J., 2017. “Adaptive backlash inverse augmented virtual decomposition control of a hydraulic manipulator”. In Cybernetics and Intelligent Systems and Conference on Robotics, Automation and Mechatronics, IEEE, pp. 322–327.

[16] Tao, G., and Kokotovic, P. V., 1995. “Adaptive control of system with unknown output backlash”. *IEEE Transactions on Automatic Control,* ***40***(2), pp. 326–330.

[17] Zhu, W.-H., 2010. *Virtual decomposition control: toward hyper degrees of freedom robots*, Vol. 60. Springer Science & Business Media.

[18] Zhu, W.-H., Xi, Y.-G., Zhang, Z.-J., Bien, Z., and De Schutter, J., 1997. “Virtual decomposition based control for generalized high dimensional robotic systems with complicated structure”. *IEEE Trans. Robot. Autom.,* ***13***(3), pp. 411–436.

[19] Zhu, W.-H., and Piedboeuf, J., 2005. “Adaptive output force tracking control of hydraulic cylinders with applications to robot manipulators”. *ASME J. Dyn. Syst., Meas., Control,* ***127***(2), June, pp. 206–217.

PUBLICATION
III

Cartesian Damping Controller with Nonlinear Control for a Floating-Base Hydraulic Manipulator

P. Mustalahti and J. Mattila

In *2022 Global Fluid Power Society PhD Symposium (GFPS)*, IEEE, Oct. 2022, Accepted

PUBLICATION
IV

Nonlinear Model-Based Control Design for a Hydraulically Actuated Spherical Wrist

P. Mustalahti and J. Mattila

In *ASME/BATH 2019 Symposium on Fluid Power and Motion Control*, ASME, Oct. 2019
DOI: 10.1115/FPMC2019-1663

**Proceedings of the 2019 ASME/Bath
Symposium on Fluid Power and Motion Control
FPMC 2019
October 7-9, 2019, Sarasota, FL, USA**

FPMC2019-1663

NONLINEAR MODEL-BASED CONTROL DESIGN FOR A HYDRAULICALLY ACTUATED SPHERICAL WRIST

Pauli Mustalahti* **and Jouni Mattila**
Automation Technology and Mechanical Engineering Unit
Tampere University
Tampere, Finland FI-33101
firstname.lastname@tuni.fi

ABSTRACT

Anthropomorphic hydraulic manipulator arms are extensively utilized for moving heavy loads in many industrial domains, e.g., in off-shore, construction and mining. By equipping these manipulator arms with an additional 3 degrees-of-freedom (DOF) spherical wrist mechanism, the dexterity and working envelope of the manipulator can be increased. For versatile operations, the motion range for the hydraulic wrist actuators should be close to 360 degrees with high torque output, with a compact volumetric size. Although the wrist can provide a high power-to-weight ratio, the actuators also introduce significant non-linearities in their dynamic behaviors. The complex dynamic behavior combined with high loads yield significant challenges in closed-loop control design. In this paper, we design a novel subsystem-dynamics-based controller for a hydraulically actuated spherical wrist mechanism utilizing the virtual decomposition control (VDC) approach. The proposed 3-DOF wrist controller is designed to be modular; thus, it can be connected as an plug-and-play subsystem into our previously designed state-of-the-art controller for a 3-DOF hydraulic manipulator arm. Stability proof of the overall 6-DOF system is provided. Experiments with a full-scale commercial hydraulic manipulator arm equipped with the 3-DOF spherical wrist demonstrate the effectiveness of the proposed method.

1 INTRODUCTION

Anthropomorphic hydraulic manipulator arms are widespread in industrial domains (e.g., construction, forestry and offshore); this is due to their high power-to-weight ratio and high robustness. A common feature of these domains is that a human operator operates the manipulator in an open-loop by controlling each joint of the manipulator separately with visual feedback. Hydraulic manipulators are also used for different repair, inspection, and maintenance tasks in challenging environments, e.g., in subsea conditions [1] and in nuclear power plants [2], where the anthropomorphic arms are typically controlled in a closed-loop haptic master-slave configuration. When manipulators are operated in a limited space with inaccurate visual feedback, automated operations with high-precision control performance are necessary to improve safety.

As discussed in [3], the commercial manipulators arm for challenging environments are typically employed with three to six actuators, providing the respective number of degrees-of-freedom (DOF) in motion. A manipulator with 3-DOF can achieve an arbitrary position, whereas a manipulator with 6-DOF can achieve both the arbitrary position and orientation of the end-effector in the workspace. The 6-DOF manipulators are usually implemented by equipping a 3-DOF manipulator arm with a 3-DOF spherical wrist.

All hydraulically actuated spherical wrist actuators must be able to deliver near to 360 degree motion range at a high torque level with a highly compact volumetric size [4]. There are three common types of hydraulic rotary actuators (i.e., vane, rack and

---

*Address all correspondence to this author

pinion, and helical spline), each with specific strengths and drawbacks. Rack and pinion gears [5] have the drawback of being bulky in size. The vane actuators [4, 6] are compact in size, but their uncontrollable joint motions mean that there is no fail-safe position. The helical spline gears are compact in size and exhibit lower but the high speed of gears causes significant friction. Thus, this study focuses on helical gear rotary actuators. In the designed spherical wrist, the angle of rotation of the first and the third actuators is *360°* and that for the second actuator is *180°*. A complex dynamic behavior (including, e.g., gear backlash [7] and actuator friction [8]) of the actuator, combined with high inertial loads, yields significant challenges in closed-loop control.

A survey of the control of hydraulic robotic manipulators [9] demonstrates, stability-guaranteed nonlinear model-based (NMB) control methods have achieve superior control performance with hydraulic manipulators. Due to the high nonlinear dynamics behavior of the hydraulic systems, NMB controllers are needed. In previous studies [10–13], virtual decomposition control (VDC) has been proven to reach the current state-of-the-art control performance with hydraulic manipulators. However, these studies focused on designing for the 2-DOF manipulator arm. The VDC controller for the 3-DOF manipulator arm is presented in [5]. Furthermore, the VDC approach is suitable for the haptic teleoperation applications, as demonstrates in [14, 15]. In [8], force tracking control was used for the six joint manipulator, but the motion range of the wrist mechanism was limited due to use of cylinder applications only. In the study, the main focus is extending VDC approach to cover 6-DOF hydraulic manipulator control by incorporating the control of the spherical wrist into previous designed controller.

The main contribution of this study is designing the NMB controller for the hydraulic rotary actuated spherical wrist by using the VDC approach as a framework. The proposed controller is also incorporated into the previous designed state-of-the-art controller for the hydraulic manipulators as plug-and-play module. The stability of the entire system is guaranteed by using rigorous stability analysis.

This paper is organized as follows. Section 2 briefly introduces the mathematical notations of the VDC approach. In Section 3, the virtual decomposition for the spherical wrist is expressed along with the kinematics and dynamics modeling of the wrist mechanism. The control equations for the studied system are presented in Section 4. The stability analysis for the entire system is addressed in Section 5. Finally, the experimental results are presented in Section 6, and conclusions are drawn in Section 7.

2 MATHEMATICAL BACKGROUND

In this section, the mathematical notations for the VDC approach are introduced. Consider an orthogonal three-dimensional coordinate frame $\{\mathbf{A}\}$ attached to the rigid body. Then, the linear/angular velocity vector in this coordinate frame can be defined as ${}^{\mathbf{A}}V = [{}^{\mathbf{A}}\mathbf{v}\ \ {}^{\mathbf{A}}\omega]^T$, following [16]. In vector ${}^{\mathbf{A}}V$, ${}^{\mathbf{A}}\mathbf{v} \in \mathbb{R}^3$ is the linear velocity vector, and ${}^{\mathbf{A}}\omega \in \mathbb{R}^3$ is the angular velocity vector. Similarly, the force/moment vector, in coordinate frame $\{\mathbf{A}\}$, is defined as a combination of a force vector ${}^{\mathbf{A}}\mathbf{f} \in \mathbb{R}^3$ and moment vector ${}^{\mathbf{A}}\mathbf{m} \in \mathbb{R}^3$, as ${}^{\mathbf{A}}F = [{}^{\mathbf{A}}\mathbf{f}\ \ {}^{\mathbf{A}}\mathbf{m}]^T$. For the two attached successive coordinate frames $\{\mathbf{A}\}$ and $\{\mathbf{B}\}$, the following holds:

$$ {}^{\mathbf{B}}V = {}^{\mathbf{A}}\mathbf{U}_{\mathbf{B}}^{T}\,{}^{\mathbf{A}}V \tag{1} $$

$$ {}^{\mathbf{A}}F = {}^{\mathbf{A}}\mathbf{U}_{\mathbf{B}}\,{}^{\mathbf{B}}F, \tag{2} $$

where ${}^{\mathbf{A}}\mathbf{U}_{\mathbf{B}} \in \mathbb{R}^{6\times6}$ describes the force/moment transformation from one fixed coordinate frame to another fixed frame.

Now, the rigid body dynamics the in coordinate frame $\{\mathbf{A}\}$ can be expressed as

$$ {}^{\mathbf{A}}F^{*} = \mathbf{M}_{\mathbf{A}}\frac{d}{dt}({}^{\mathbf{A}}V) + \mathbf{C}_{\mathbf{A}}({}^{\mathbf{A}}\omega){}^{\mathbf{A}}V + \mathbf{G}_{\mathbf{A}} \tag{3} $$

where $\mathbf{M}_{A} \in \mathbb{R}^{6\times6}$ is the mass matrix, $\mathbf{C}_{\mathbf{A}}({}^{\mathbf{A}}\omega) \in \mathbb{R}^{6\times6}$ is the Coriolis and centrifugal terms, ${}^{\mathbf{A}}F^{*} \in \mathbb{R}^{6}$ is the net force/moment vector, and $\mathbf{G}_{\mathbf{A}} \in \mathbb{R}^{6}$ is the gravity vector.

For the control design, the linear-in-parameter expression [16] for the required rigid body dynamics can be expressed as

$$ \mathbf{Y}_{\mathbf{A}}\theta_{\mathbf{A}} \overset{\text{def}}{=} \mathbf{M}_{\mathbf{A}}\frac{d}{dt}({}^{\mathbf{A}}V_{\mathrm{r}}) + \mathbf{C}_{\mathbf{A}}({}^{\mathbf{A}}\omega){}^{\mathbf{A}}V_{\mathrm{r}} + \mathbf{G}_{\mathbf{A}} \tag{4} $$

In relation to Eq. (4), the regressor matrix $\mathbf{Y}_{A} \in \mathbb{R}^{6\times13}$ and parameter vector $\theta_{\mathbf{A}} \in \mathbb{R}^{13}$ are specified in [16].

Finally, the required net force/moment vectors for the *rigid links*, in view of [16], can be defined as

$$ {}^{\mathbf{A}}F_{r}^{*} = \mathbf{Y}_{\mathbf{A}}\widehat{\theta}_{\mathbf{A}} + K_{\mathbf{A}}({}^{\mathbf{A}}V_{r} - {}^{\mathbf{A}}V) \tag{5} $$

In Eq. (5), $K_{\mathbf{A}}$ is the velocity feedback control gain and vector $\widehat{\theta}_{\mathbf{A}}$ denotes the estimate for the parameter vector $\theta_{\mathbf{A}}$. Estimations for the parameters in vector $\theta_{\mathbf{A}}$ in Eq. (5) can be updated as following

$$ \mathbf{s}_{\mathbf{A}} = \mathbf{Y}_{\mathbf{A}}^{T}({}^{\mathbf{A}}V_{r} - {}^{\mathbf{A}}V) \tag{6} $$

Now, the ith element of $\widehat{\theta}_{\mathbf{B}_j}$ can be updated, according to Definition 2.11 in [16], as

$$ \widehat{\theta}_{\mathbf{A}_i} = \mathscr{P}(s_{\mathbf{A}_i}, \rho_{\mathbf{A}_i}, \underline{\theta}_{\mathbf{A}_i}, \overline{\theta}_{\mathbf{A}_i}, t)\ \forall i \in \{1,2,\dots,13\}. \tag{7} $$

In Eq. (7), $\widehat{\theta}_{\mathbf{A}_i}$ denotes the ith element of $\widehat{\theta}_{\mathbf{A}}$, $s_{\mathbf{A}_i}$ denotes the ith element of $s_{\mathbf{A}}$, $\rho_{\mathbf{A}_i} > 0$ is the update gain, $\underline{\theta}_{\mathbf{A}_i}$ is the lower bound of $\theta_{\mathbf{A}}$, $\overline{\theta}_{\mathbf{A}_i}$ is the upper bound of $\theta_{\mathbf{A}}$.

3 KINEMATICS AND DYNAMICS FOR THE SPHERICAL WRIST

The traditional commercial heavy-duty manipulators may not be suitable for complex industrial tasks in all applications due to a limited working envelope and dexterity of the manipulator. For this reason, by equipping the manipulator arm with a 3-DOF spherical wrist, the manipulator dexterity can be significantly increased. The hydraulic rotary actuated wrist can provide a high power-to-weight ratio. The commercial 3-DOF hydraulic manipulator arm with a hydraulic rotary actuated spherical wrist is shown in Fig. 1.

The main contribution of this paper is designing model-based control for the hydraulic rotary actuated spherical wrist by using control design principles of the VDC approach. This approach (see [16, 17]) is especially designed for controlling complex robotic systems. As a novel property, the VDC approach allows the control design and the stability analysis to be carried out locally at the subsystem level. A model-based control design for a 2-DOF hydraulic manipulator arm is specified in [18], and a control design for a rotary boom manipulator is given in [5].

The main parts of the VDC approach are as presented follows: 1) virtual decomposition of the 3-DOF spherical wrist, 2) simple oriented graph (SOG) presentation, and 3) coordinate frame attachment to subsystems. Then, the kinematics and dynamics equations for the hydraulic rotary actuated spherical wrist are defined.

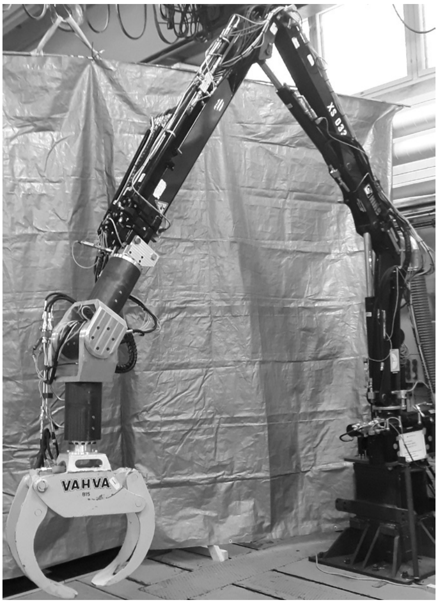

FIGURE 1. Commercial hydraulic manipulator with a spherical wrist

3.1 Virtual Decomposition of the Spherical Wrist

The commercial manipulator in Fig. 1 consists of the three following hydraulic cylinders: 1) a boom rotation cylinder, 2) lift cylinder and 3) tilt cylinder. The 3-DOF spherical wrist consists of three serially connected rotary actuators, which are presented in Fig. 2a. Here, the angle of rotation of the first and third rotary actuators is *360*° and that for the second actuator is *180*°. This structure is equal to the wrist mechanism in industrial robotics. As Fig. 1 show, the gripping tool is connected at the end of the third rotary actuator; in this study, the gripper is unused.

In the VDC approach, the first step is virtual decomposing the entire studied system into subsystems, which are called *objects* and *open chains*. The virtual decomposition is constructed by placing *virtual cutting points* (VCPs) in the studied system. A VCP describes the separation the between successive subsystems by defining the direction for the force/moment relation to these subsystems. One VCP is simultaneously interfered driven the VCP for one subsystem and driving for another subsystem. The driving VCP is the point from which and to which the force/moment vector is exerted. Virtual decomposition for the spherical wrist mechanism is expressed in Fig. 2b.

The dynamics between successive subsystems in a virtual decomposition system can be representing as SOG (see Definition 2.14 in [16]). The SOG describes the force/moment directions as directed edges and rigid links as nodes. The SOG for the spherical wrist is given in Fig. 2c, where the subsystems of the wrist mechanism are shown with a dashed line.

In Fig. 2c, *open chains 1, 2, and 3* consist of hydraulic rotary gear actuators, which transform cylinder linear force to the torque. The internal structure of these actuators is that of a symmetric hydraulic cylinder, as Fig. 3 shows. The rotary actuators are directly controlled using hydraulic servo-valves. In Fig. 3, the actuator rotation angles q_1, q_2, and q_3 are defined so that the positive direction is counter-clockwise.

The subsystems' kinematic and dynamics relations require the coordinate frames for the rigid links to be fixed. The fixed coordinate frames of the spherical wrist are given in Fig. 2a, and the coordinate frames for the hydraulic cylinders are presented in Fig. 3. The coordinate frames are attached so that the z-axis points out from the paper in Fig. 2a and Fig. 3.

3.2 Kinematics of the Hydraulically Actuated Spherical Wrist

In view of Eq. (1), the linear/angular velocity relations of coordinate frames in Fig. 2a can be defined as

$$ {}^{\mathbf{B}_1}V = {}^{\mathbf{B}_0}\mathbf{U}_{\mathbf{B}_1}^{T}\,{}^{\mathbf{B}_0}V + \mathbf{z}\dot{q}_1 \tag{8} $$

$$ {}^{\mathbf{B}_2}V = {}^{\mathbf{B}_1}\mathbf{U}_{\mathbf{B}_2}^{T}\,{}^{\mathbf{B}_1}V + \mathbf{z}_{\tau}\dot{q}_2 \tag{9} $$

$$ {}^{\mathbf{B}_3}V = {}^{\mathbf{B}_2}\mathbf{U}_{\mathbf{B}_3}^{T}\,{}^{\mathbf{B}_2}V + \mathbf{z}\dot{q}_3 \tag{10} $$

$$ {}^{\mathbf{B}_4}V = {}^{\mathbf{B}_3}\mathbf{U}_{\mathbf{B}_4}^{T}\,{}^{\mathbf{B}_3}V \tag{11} $$

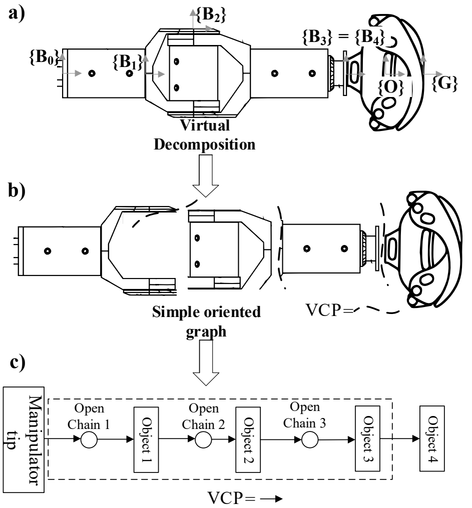

FIGURE 2. Virtual decomposition of the spherical wrist

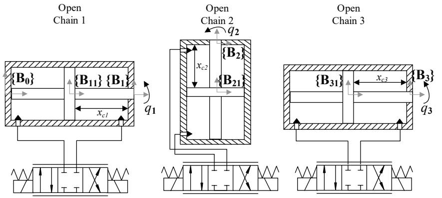

FIGURE 3. Structure of the hydraulically actuated spherical wrist

where $\mathbf{z} = [0\,0\,0\,1\,0\,0]^T$, $\mathbf{z}_\tau = [0\,0\,0\,0\,1\,0]^T$, and $\dot{q}_1$, $\dot{q}_2$,and $\dot{q}_3$ are the angular velocities of the wrist joints. Furthermore, the linear velocity in coordinate frames in the Fig. 3 can be expressed as

$$
\begin{aligned}
{}^{\mathbf{B}_{11}}V &= u_1\mathbf{z}\dot{q}_1 \qquad (12)\\
{}^{\mathbf{B}_{21}}V &= u_2\mathbf{z}_\tau\dot{q}_2 \qquad (13)\\
{}^{\mathbf{B}_{31}}V &= u_3\mathbf{z}\dot{q}_3 \qquad (14)
\end{aligned}
$$

where u_1, u_2, and u_3 denote the gear ratios of the rotary actuators, $\mathbf{z} = [0\,0\,0\,1\,0\,0]^T$, and $\mathbf{z}_\tau = [0\,0\,0\,0\,1\,0]^T$.

3.3 Kinematics of the Gripper Tool Object

The kinematics relations of the gripper tool object can be written, in view of Eq. (1) and Fig. 2a, as

$$
{}^{\mathbf{O}}V = {}^{\mathbf{B}_4}\mathbf{U}_{\mathbf{O}}^{T}\,{}^{\mathbf{B}_4}V = {}^{\mathbf{G}}\mathbf{U}_{\mathbf{O}}^{T}\,{}^{\mathbf{G}}V \tag{15}
$$

3.4 Dynamics of the Gripper Tool Object

According to Eq. (3), the force/moment vector for the gripper tool object can be written as

$$
{}^{\mathbf{O}}F^* = \mathbf{M_O}\frac{d}{dt}({}^{\mathbf{O}}V) + \mathbf{C_O}({}^{\mathbf{O}}\omega){}^{\mathbf{O}}V + \mathbf{G_O} \tag{16}
$$

In contrast,

$$
{}^{\mathbf{O}}F^* = {}^{\mathbf{O}}\mathbf{U}_{\mathbf{B}_4}{}^{\mathbf{B}_4}F - {}^{\mathbf{O}}\mathbf{U}_{\mathbf{G}}{}^{\mathbf{G}}F \tag{17}
$$

holds for the gripper tool object, while for the external force vector,

$$
{}^{\mathbf{G}}\boldsymbol{F} = [0\,0\,0\,0\,0\,0]^T \tag{18}
$$

holds in the free-space motions.

3.5 Dynamics of the Spherical Wrist

The following dynamics relations holds, in view of Eq. 3, for the spherical wrist *open chains*

$$
\begin{aligned}
{}^{\mathbf{B}_0}F^* &= \mathbf{M}_{\mathbf{B}_1}\frac{d}{dt}({}^{\mathbf{B}_1}V) + \mathbf{C}_{\mathbf{B}_1}({}^{\mathbf{B}_1}\omega){}^{\mathbf{B}_1}V + \mathbf{G}_{\mathbf{B}_1} \qquad (19)\\
{}^{\mathbf{B}_1}F^* &= \mathbf{M}_{\mathbf{B}_2}\frac{d}{dt}({}^{\mathbf{B}_2}V) + \mathbf{C}_{\mathbf{B}_2}({}^{\mathbf{B}_2}\omega){}^{\mathbf{B}_2}V + \mathbf{G}_{\mathbf{B}_2} \qquad (20)\\
{}^{\mathbf{B}_2}F^* &= \mathbf{M}_{\mathbf{B}_3}\frac{d}{dt}({}^{\mathbf{B}_3}V) + \mathbf{C}_{\mathbf{B}_3}({}^{\mathbf{B}_3}\omega){}^{\mathbf{B}_3}V + \mathbf{G}_{\mathbf{B}_3} \qquad (21)\\
{}^{\mathbf{B}_3}F^* &= \mathbf{M}_{\mathbf{B}_4}\frac{d}{dt}({}^{\mathbf{B}_4}V) + \mathbf{C}_{\mathbf{B}_4}({}^{\mathbf{B}_4}\omega){}^{\mathbf{B}_4}V + \mathbf{G}_{\mathbf{B}_4} \qquad (22)
\end{aligned}
$$

Then, the total force/moment vectors in coordinate frames, can be defined as

$$
\begin{aligned}
{}^{\mathbf{B}_3}F &= {}^{\mathbf{B}_3}F^* + {}^{\mathbf{B}_3}\mathbf{U}_{\mathbf{B}_4}{}^{\mathbf{B}_4}F \qquad (23)\\
{}^{\mathbf{B}_2}F &= {}^{\mathbf{B}_2}F^* + {}^{\mathbf{B}_2}\mathbf{U}_{\mathbf{B}_3}{}^{\mathbf{B}_3}F \qquad (24)\\
{}^{\mathbf{B}_1}F &= {}^{\mathbf{B}_1}F^* + {}^{\mathbf{B}_1}\mathbf{U}_{\mathbf{B}_2}{}^{\mathbf{B}_2}F \qquad (25)\\
{}^{\mathbf{B}_0}F &= {}^{\mathbf{B}_0}F^* + {}^{\mathbf{B}_0}\mathbf{U}_{\mathbf{B}_1}{}^{\mathbf{B}_1}F \qquad (26)
\end{aligned}
$$

Finally, the linear force of the hydraulic cylinders in Fig. 3 can be defined using Eqs. 24–26 as

$$
\begin{aligned}
f_{c3} &= \frac{1}{u_3}\mathbf{z}^{T}\,{}^{\mathbf{B}_3}F \qquad (27)\\
f_{c2} &= \frac{1}{u_2}\mathbf{z}_\tau^{T}\,{}^{\mathbf{B}_2}F \qquad (28)\\
f_{c1} &= \frac{1}{u_1}\mathbf{z}^{T}\,{}^{\mathbf{B}_1}F \qquad (29)
\end{aligned}
$$

where u_1, u_2, and u_3 are the gear ratio of rotary actuator, $\mathbf{z} = [0\ 0\ 0\ 1\ 0\ 0]^T$, and $\mathbf{z}_\tau = [0\ 0\ 0\ 0\ 1\ 0]^T$.

4 CONTROL EQUATIONS FOR THE HYDRAULICALLY ACTUATED SPHERICAL WRIST

This section specifies the control equations for the spherical wrist with parameter adaption. In addition, the adaptive backlash model (see [5]) for the rotary actuators is incorporated into the control design. As Fig. 3 shows, the control system consists of hydraulic cylinders and servo-valves. The dynamics model for the hydraulic cylinder is specified in [16] and [10] with corresponding modular control equations. These equations can be incorporate into the control design by defining the kinematics and dynamics equations in view of the VDC approach.

4.1 Required Kinematics of the Hydraulically Actuated Spherical Wrist

In view of Eqs. 8–10, the required linear/angular velocities can be defined as

$$
\begin{aligned}
{}^{\mathbf{B}_1}V_r &= {}^{\mathbf{B}_0}\mathbf{U}_{\mathbf{B}_1}^T\,{}^{\mathbf{B}_0}V_r + \mathbf{z}\dot{q}_{1r} && (30)\\
{}^{\mathbf{B}_2}V_r &= {}^{\mathbf{B}_1}\mathbf{U}_{\mathbf{B}_2}^T\,{}^{\mathbf{B}_1}V_r + \mathbf{z}_\tau\dot{q}_{2r} && (31)\\
{}^{\mathbf{B}_3}V_r &= {}^{\mathbf{B}_2}\mathbf{U}_{\mathbf{B}_3}^T\,{}^{\mathbf{B}_2}V_r + \mathbf{z}\dot{q}_{3r} && (32)\\
{}^{\mathbf{B}_4}V_r &= {}^{\mathbf{B}_3}\mathbf{U}_{\mathbf{B}_4}^T\,{}^{\mathbf{B}_3}V_r && (33)
\end{aligned}
$$

where $\mathbf{z} = [0\ 0\ 0\ 1\ 0\ 0]^T$, $\mathbf{z}_\tau = [0\ 0\ 0\ 0\ 1\ 0]^T$, and $\dot{q}_{1r}$, $\dot{q}_{2r}$, and $\dot{q}_{3r}$ are the angular velocities of the wrist joints. Similarly, the required velocities in coordinate frames in Fig. 3 can be written as

$$
\begin{aligned}
{}^{\mathbf{B}_{11}}V_r &= u_1\mathbf{z}\dot{q}_{1r} && (34)\\
{}^{\mathbf{B}_{21}}V_r &= u_2\mathbf{z}_\tau\dot{q}_{2r} && (35)\\
{}^{\mathbf{B}_{31}}V_r &= u_3\mathbf{z}\dot{q}_{3r} && (36)
\end{aligned}
$$

where u_1, u_2, and u_3 are the gear ratios of rotary actuator.

4.2 Required Kinematics of the Gripper Tool Object

The gripper tool object's required kinematics model can be specified, in view of Eq. (15), as

$$
{}^{\mathbf{O}}V_r = {}^{\mathbf{B}_4}\mathbf{U}_{\mathbf{O}}^T\,{}^{\mathbf{B}_4}V_r = {}^{\mathbf{G}}\mathbf{U}_{\mathbf{O}}^T\,{}^{\mathbf{G}}V_r \qquad (37)
$$

4.3 Required Dynamics of the Gripper Tool Object

The required net force/moment vector of the gripper tool object can be written, by reusing Eq. (5), as

$$
{}^{\mathbf{O}}F_r^* = \mathbf{Y}_{\mathbf{O}}\widehat{\theta}_{\mathbf{O}} + \mathbf{K}_{\mathbf{O}}({}^{\mathbf{O}}V_r - {}^{\mathbf{O}}V) \qquad (38)
$$

The parameter vector $\widehat{\theta}_{\mathbf{O}}$ can be updates by reusing Eqs. (7) as

$$
\widehat{\theta}_{\mathbf{O}_i} = \mathscr{P}(s_{\mathbf{O}_i}, \rho_{\mathbf{O}_i}, \underline{\theta}_{\mathbf{O}_i}, \overline{\theta}_{\mathbf{O}_i}, t)\ \forall i \in \{1,2,\ldots,13\} \qquad (39)
$$

Furthermore, it follows from Eq. (17) that, the net force/moment vector in frame $\{\mathbf{B}_4\}$ can be presented as

$$
{}^{\mathbf{B}_4}F_r^* = {}^{\mathbf{B}_4}\mathbf{U}_{\mathbf{O}}\,{}^{\mathbf{B}_4}F_r - {}^{\mathbf{B}_4}\mathbf{U}_{\mathbf{G}}\,{}^{\mathbf{G}}F_r \qquad (40)
$$

and, similarly to Eq. (18), ${}^{\mathbf{G}}F_r$ is defined as

$$
{}^{\mathbf{G}}F_r = [0\ 0\ 0\ 0\ 0\ 0]^T \qquad (41)
$$

4.4 Required Dynamics of the Spherical Wrist

The kinematics model for the spherical wrist subsystems in Eqs. (30)–(33) enables the required net force/moment vectors for rigid links to be written, according Eq. (5), as

$$
\begin{aligned}
{}^{\mathbf{B}_0}F_r^* &= \mathbf{Y}_{\mathbf{B}_0}\widehat{\theta}_{\mathbf{B}_0} + \mathbf{K}_{\mathbf{B}_0}({}^{\mathbf{B}_0}V_r - {}^{\mathbf{B}_0}V) && (42)\\
{}^{\mathbf{B}_1}F_r^* &= \mathbf{Y}_{\mathbf{B}_1}\widehat{\theta}_{\mathbf{B}_1} + \mathbf{K}_{\mathbf{B}_1}({}^{\mathbf{B}_1}V_r - {}^{\mathbf{B}_1}V) && (43)\\
{}^{\mathbf{B}_2}F_r^* &= \mathbf{Y}_{\mathbf{B}_2}\widehat{\theta}_{\mathbf{B}_2} + \mathbf{K}_{\mathbf{B}_2}({}^{\mathbf{B}_2}V_r - {}^{\mathbf{B}_2}V) && (44)\\
{}^{\mathbf{B}_3}F_r^* &= \mathbf{Y}_{\mathbf{B}_3}\widehat{\theta}_{\mathbf{B}_3} + \mathbf{K}_{\mathbf{B}_3}({}^{\mathbf{B}_3}V_r - {}^{\mathbf{B}_3}V) && (45)
\end{aligned}
$$

where $\mathbf{K}_{\mathbf{B}_0}$, $\mathbf{K}_{\mathbf{B}_1}$, $\mathbf{K}_{\mathbf{B}_2}$, and $\mathbf{K}_{\mathbf{B}_3}$ are the velocity feedback control gains. Vectors $\widehat{\theta}_{\mathbf{B}_0}$, $\widehat{\theta}_{\mathbf{B}_1}$, $\widehat{\theta}_{\mathbf{B}_2}$, and $\widehat{\theta}_{\mathbf{B}_3}$ denote the estimates of parameter vectors $\theta_{\mathbf{B}_0}$, $\theta_{\mathbf{B}_1}$, $\theta_{\mathbf{B}_2}$ and $\theta_{\mathbf{B}_3}$. By reusing Eq. (6), the update version of these vectors can be presented as

$$
\begin{aligned}
\mathbf{s}_{\mathbf{B}_0} &= \mathbf{Y}_{\mathbf{B}_0}^T({}^{\mathbf{B}_0}V_r - {}^{\mathbf{B}_0}V) && (46)\\
\mathbf{s}_{\mathbf{B}_1} &= \mathbf{Y}_{\mathbf{B}_1}^T({}^{\mathbf{B}_1}V_r - {}^{\mathbf{B}_1}V) && (47)\\
\mathbf{s}_{\mathbf{B}_2} &= \mathbf{Y}_{\mathbf{B}_2}^T({}^{\mathbf{B}_2}V_r - {}^{\mathbf{B}_2}V) && (48)\\
\mathbf{s}_{\mathbf{B}_3} &= \mathbf{Y}_{\mathbf{B}_3}^T({}^{\mathbf{B}_3}V_r - {}^{\mathbf{B}_3}V) && (49)
\end{aligned}
$$

Further, the ith element of $\widehat{\theta}_{\mathbf{B}_j}$ can be updated, using Eq. (7), as

$$
\widehat{\theta}_{\mathbf{B}_{ij}} = \mathscr{P}(s_{\mathbf{B}_{ij}}, \rho_{\mathbf{B}_{ij}}, \underline{\theta}_{\mathbf{B}_{ij}}, \overline{\theta}_{\mathbf{B}_{ij}}, t)\ \forall i \in \{1,2,\ldots,13\} \qquad (50)
$$

In Eq. (50), $\widehat{\theta}_{\mathbf{B}_{ij}}$ denotes the ith element of $\widehat{\theta}_{\mathbf{B}_j}$, $s_{\mathbf{B}_{ij}}$ denotes the ith element of $s_{\mathbf{B}_j}$, $\rho_{\mathbf{B}_{ij}} > 0$ is the update gain, $\underline{\theta}_{\mathbf{B}_{ij}}$ is the lower bound of $\theta_{\mathbf{B}_j}$, $\overline{\theta}_{\mathbf{B}_{ij}}$ is the upper bound of $\theta_{\mathbf{B}_j}$, and $j \in \{0,1,2,3\}$ is the order number of the coordinate frame.

Now, it follows from Eqs. (5), (42), and (44) that the force/moment vectors for the spherical wrist subsystems can be written as

$$
\begin{aligned}
{}^{\mathbf{B}_3}F_r &= {}^{\mathbf{B}_3}F_r^* + {}^{\mathbf{B}_3}\mathbf{U}_{\mathbf{B}_4}{}^{\mathbf{B}_4}F_r && (51)\\
{}^{\mathbf{B}_2}F_r &= {}^{\mathbf{B}_2}F_r^* + {}^{\mathbf{B}_2}\mathbf{U}_{\mathbf{B}_3}{}^{\mathbf{B}_3}F_r && (52)\\
{}^{\mathbf{B}_1}F_r &= {}^{\mathbf{B}_1}F_r^* + {}^{\mathbf{B}_1}\mathbf{U}_{\mathbf{B}_2}{}^{\mathbf{B}_2}F_r && (53)\\
{}^{\mathbf{B}_0}F_r &= {}^{\mathbf{B}_0}F_r^* + {}^{\mathbf{B}_0}\mathbf{U}_{\mathbf{B}_1}{}^{\mathbf{B}_1}F_r && (54)
\end{aligned}
$$

Then, the required cylinder piston forces can be calculated from Eqs. (52)–(54)

$$
\begin{aligned}
f_{c3r} &= \frac{1}{u_3}\mathbf{z}^T{}^{\mathbf{B}_3}F_r && (55)\\
f_{c2r} &= \frac{1}{u_2}\mathbf{z}_\tau^T{}^{\mathbf{B}_2}F_r && (56)\\
f_{c1r} &= \frac{1}{u_1}\mathbf{z}^T{}^{\mathbf{B}_1}F_r && (57)
\end{aligned}
$$

where u_1, u_2, and u_3 are the gear ratios of rotary actuators, and $\mathbf{z} = [0\ 0\ 0\ 1\ 0\ 0]^T$ and $\mathbf{z}_\tau = [0\ 0\ 0\ 0\ 1\ 0]^T$.

4.5 Adaptive Backlash Inverse Model

Backlash is common in non-smooth non-linearity and it may limit the control performance. As presented in [5], the adaptive backlash inverse model can be used to compensate for the effect of the gear backlash. The adaptive backlash inverse model for the desired output of the backlash can be defined as

$$v_{bc} = \mathbf{Y}_{bc}(\dot{u}_{tr})\widehat{\theta}_{bc} \qquad (58)$$

where v_{bc} is the desired output vector, $\dot{u}_{tr}$ is the desired gear velocity, $\mathbf{Y}_{bc}$ is the regressor matrix for the backlash model, and $\widehat{\theta}_{bc}$ is the parameter vector for the backlash model. Continuously, the adaptive backlash inverse for the velocity can be written as

$$\dot{v}_{bc} = \mathbf{Y}_{bv}(\dot{u}_{tr})\widehat{\theta}_{bv} \qquad (59)$$

where $\dot{v}_{bv}$ is the desired output vector, $\dot{u}_{tr}$ is the desired gear velocity, $\mathbf{Y}_{bv}$ is the regressor matrix for the backlash model, and $\widehat{\theta}_{bv}$ is parameter vector for the backlash model velocity. In view of [5], the estimations for the parameter vectors $\widehat{\theta}_{bc}$ and $\widehat{\theta}_{bv}$ can be updated, as

$$\mathbf{s}_{bc} = \mathbf{Y}_{bc}^T(\dot{u}_{tr})(\dot{u}_{tr} - \dot{u}) \qquad (60)$$

where $\dot{u}_{tr}$ denotes the desired output velocity of the model, and $\dot{u}$ denotes the measured joint velocity. Now, the ith element of $\widehat{\theta}_{bc}$ can be updated, according to Eq. (7), as

$$\widehat{\theta}_{bc_i} = \mathscr{P}(s_{bc_i}, \rho_{bc_i}, \underline{\theta}_{bc_i}, \overline{\theta}_{bc_i}, t)\ \forall i \in \{1,2,3\} \qquad (61)$$

where $\widehat{\theta}_{bc_i}$ denotes the ith element of θ_{bc}, s_{bc_i} denotes the ith element of s_{bc}, $\rho_{bc} > 0$ is the update gain, $\underline{\theta}_{bc_i}$ is the lower bound for of θ_{bc}, and $\overline{\theta}_{bc_i}$ is the upper bound for of θ_{bc}.

Finally, by using Eqs. 58–59, the adaptive backlash model can be incorporated into the control design by defining the required angular velocities in Eqs. 30–32, as

$$
\begin{aligned}
\dot{q}_{1r} &= \mathbf{Y}_{bv1}(\dot{u}_{tr1})\widehat{\theta}_{bv1} + \lambda_1(\mathbf{Y}_{bc1}(\dot{u}_{tr1})\widehat{\theta}_{bc1} - q_1) && (62)\\
\dot{q}_{2r} &= \mathbf{Y}_{bv2}(\dot{u}_{tr2})\widehat{\theta}_{bv2} + \lambda_2(\mathbf{Y}_{bc2}(\dot{u}_{tr2})\widehat{\theta}_{bc2} - q_2) && (63)\\
\dot{q}_{3r} &= \mathbf{Y}_{bv3}(\dot{u}_{tr3})\widehat{\theta}_{bv3} + \lambda_3(\mathbf{Y}_{bc3}(\dot{u}_{tr3})\widehat{\theta}_{bc3} - q_3) && (64)
\end{aligned}
$$

where q_1, q_2, and q_3 are measured wrist joint angles (see Fig. 3) and $\dot{q}_1$, $\dot{q}_2$, and $\dot{q}_3$ are required wrist joint velocities.

5 STABILITY ANALYSIS FOR THE SPHERICAL WRIST

This section describes the virtual stability analysis for the hydraulically actuated spherical wrist (see Fig. 2a) with parameter adaption. In addition, the stability analysis for the gripper tool object is addressed. The virtual stability of the 2-DOF hydraulic manipulator arm is specified closely in [18], and the stability analysis for the rotary boom manipulator is given in [5]. Based on these analyses, the virtual stability of the entire system can be proven.

5.1 Virtual Stability of the Gripper Tool Object

The virtual stability of the gripper tool object in the sense of Definition 2.17 in [16] can be ensured by considering Theorem 1.

Theorem 1. *Consider the gripper tool object depicted in Fig. 2, described by Eqs.* (15)–(18)*, and combined with its control Eqs.* (37)–(41)*. Subject to the gripper free-space motion, this subsystem is virtually stable, with its affiliated vector* ${}^{\mathbf{O}}V_r - {}^{\mathbf{O}}V$ *being a virtual function in* L_2 *and* L_∞ *in the sense of Definition 2.17 in [16].*

Proof. Subtracting Eq. (16) from Eq. (38) yields

$$
\begin{aligned}
{}^{\mathbf{O}}F_r^* - {}^{\mathbf{O}}F^* = \mathbf{M}_{\mathbf{O}}\frac{d}{dt}({}^{\mathbf{O}}V_r - {}^{\mathbf{O}}V) + \mathbf{C}_{\mathbf{O}}({}^{\mathbf{O}}\omega)({}^{\mathbf{O}}V_r - {}^{\mathbf{O}}V)\\
+\mathbf{K}_{\mathbf{O}}({}^{\mathbf{O}}V_r - {}^{\mathbf{O}}V) \qquad (65)
\end{aligned}
$$

Further, the skew-symmetric property of $\mathbf{C}_{\mathbf{O}}({}^{\mathbf{O}}\omega)$ yields

$$({}^{\mathbf{O}}V_r - {}^{\mathbf{O}}V)^T\mathbf{C}({}^{\mathbf{O}}\omega)({}^{\mathbf{O}}V_r - {}^{\mathbf{O}}V) = 0 \qquad (66)$$

Now, if the non-negative accompanying function for the gripper tool object is chosen as

$$v_{\mathbf{O}} = \frac{1}{2}({}^{\mathbf{O}}V_r - {}^{\mathbf{O}}V)^T \mathbf{M}_{\mathbf{O}}({}^{\mathbf{O}}V_r - {}^{\mathbf{O}}V) + \frac{1}{2}\sum_{i=1}^{13}\frac{(\theta_{\mathbf{O}} - \widehat{\theta}_{\mathbf{O}})^2}{\rho_{\mathbf{O}}} \tag{67}$$

It follows from Eqs. (65)–(66) that the time derivative of $v_{\mathbf{O}}$ can be written as

$$\begin{aligned} \dot{v}_{\mathbf{O}} &\le ({}^{\mathbf{O}}V_r - {}^{\mathbf{O}}V)^T \mathbf{M}_{\mathbf{O}} \frac{d}{dt}({}^{\mathbf{O}}V_r - {}^{\mathbf{O}}V) \\ &\le ({}^{\mathbf{O}}V_r - {}^{\mathbf{O}}V)^T \Big[({}^{\mathbf{O}}F_r^* - {}^{\mathbf{O}}F^*) - \mathbf{C}({}^{\mathbf{O}}\omega)({}^{\mathbf{O}}V_r - {}^{\mathbf{O}}V) \\ &\quad - \mathbf{K}_{\mathbf{O}}({}^{\mathbf{O}}V_r - {}^{\mathbf{O}}V)\Big] \\ &\le -({}^{\mathbf{O}}V_r - {}^{\mathbf{O}}V)^T \mathbf{K}_{\mathbf{O}}({}^{\mathbf{O}}V_r - {}^{\mathbf{O}}V) \\ &\quad + ({}^{\mathbf{O}}V_r - {}^{\mathbf{O}}V)^T ({}^{\mathbf{O}}F_r^* - {}^{\mathbf{O}}F^*) \end{aligned} \tag{68}$$

Using Definition 2.16 in [16] and Eqs. (15), (17), (18), (37), (40), and (41), the last term in (68) can be derived as

$$\begin{aligned} &({}^{\mathbf{O}}V_r - {}^{\mathbf{O}}V)^T ({}^{\mathbf{O}}F_r^* - {}^{\mathbf{O}}F^*) \\ &= ({}^{\mathbf{O}}V_r - {}^{\mathbf{O}}V)^T {}^{\mathbf{O}}\mathbf{U}_{\mathbf{B}_4}({}^{\mathbf{B}_4}F_r - {}^{\mathbf{B}_4}F) \\ &- ({}^{\mathbf{O}}V_r - {}^{\mathbf{O}}V)^T {}^{\mathbf{O}}\mathbf{U}_{\mathbf{G}}({}^{\mathbf{G}}F_r - {}^{\mathbf{G}}F) \\ &= \Big[{}^{\mathbf{O}}\mathbf{U}_{\mathbf{B}_4}^T({}^{\mathbf{O}}V_r - {}^{\mathbf{O}}V)\Big]^T ({}^{\mathbf{B}_4}F_r - {}^{\mathbf{B}_4}F) \\ &= p_{\mathbf{B}_4} \end{aligned} \tag{69}$$

where p_4 is the virtual power flow of the gripper tool object. As Eqs. (18) and (41) denotes, there is no external force in free-space motions. For this reason, another virtual power flow is zero for the tool object. Finally, substituting Eq. (69) into Eq. (68) yields

$$\dot{v}_{\mathbf{O}} = -({}^{\mathbf{O}}V_r - {}^{\mathbf{O}}V)^T \mathbf{K}_{\mathbf{O}}({}^{\mathbf{O}}V_r - {}^{\mathbf{O}}V) + p_{\mathbf{B}_3} \tag{70}$$

Consider that the gripper tool object has one *driven* VCP associated with frame $\{\mathbf{B}_4\}$. Then, using (67) and (70) completes the proof of the *virtual stability* of the gripper tool object, in the sense of Definition 2.17 in [16], ensuring that ${}^{\mathbf{O}}V_r - {}^{\mathbf{O}}V \in L_2 \bigcap L_\infty$. ■

5.2 Virtual Stability of the Spherical Wrist

The following theorem Theorem 2, ensures that spherical wrist subsystems are *virtually stable* in the sense of Definition 2.17 in [16].

Theorem 2. *Let the spherical wrist be composed of three rigid links and three actuated revolute joints as, described in Fig. 2a, depicted by Eqs.* (8)–(14) *and* (19)–(29)*, and combined with its control Eqs.* (42)–(57)*. The studied subsystem is virtually stable, with its affiliated vectors* ${}^{\mathbf{B}j}V_r - {}^{\mathbf{B}j}V$, $\forall j \in \{0,1,2,3\}$ *being a virtual function in* L_2 *and* L_∞ *in view of Definition 2.17 in [16].*

Proof. If the non-negative accompanying function v_{sw} for the spherical wrist (see Fig. 2a) is chosen as

$$v_{sw} = v_{\mathbf{B}_0} + v_{\mathbf{B}_1} + v_{\mathbf{B}_2} + v_{\mathbf{B}_3} \tag{71}$$

where $v_{\mathbf{B}_0}$, $v_{\mathbf{B}_1}$, $v_{\mathbf{B}_2}$, and $v_{\mathbf{B}_3}$ denote the non-negative accompanying functions for the rigid links of the spherical wrist, and they are defined as

$$\begin{aligned} v_{\mathbf{B}_0} &= \frac{1}{2}({}^{\mathbf{B}_0}V_r - {}^{\mathbf{B}_0}V)^T \mathbf{M}_{\mathbf{B}_0}({}^{\mathbf{B}_0}V_r - {}^{\mathbf{B}_0}V) \\ &\quad + \frac{1}{2}\sum_{i=1}^{13}\frac{(\theta_{\mathbf{B}_{0i}} - \widehat{\theta}_{\mathbf{B}_{0i}})^2}{\rho_{\mathbf{B}_{0i}}} \end{aligned} \tag{72}$$

$$\begin{aligned} v_{\mathbf{B}_1} &= \frac{1}{2}({}^{\mathbf{B}_1}V_r - {}^{\mathbf{B}_1}V)^T \mathbf{M}_{\mathbf{B}_1}({}^{\mathbf{B}_1}V_r - {}^{\mathbf{B}_1}V) \\ &\quad + \frac{1}{2}\sum_{i=1}^{13}\frac{(\theta_{\mathbf{B}_{1i}} - \widehat{\theta}_{\mathbf{B}_{1i}})^2}{\rho_{\mathbf{B}_{1i}}} \end{aligned} \tag{73}$$

$$\begin{aligned} v_{\mathbf{B}_2} &= \frac{1}{2}({}^{\mathbf{B}_2}V_r - {}^{\mathbf{B}_2}V)^T \mathbf{M}_{\mathbf{B}_2}({}^{\mathbf{B}_2}V_r - {}^{\mathbf{B}_2}V) \\ &\quad + \frac{1}{2}\sum_{i=1}^{13}\frac{(\theta_{\mathbf{B}_{2i}} - \widehat{\theta}_{\mathbf{B}_{2i}})^2}{\rho_{\mathbf{B}_{2i}}} \end{aligned} \tag{74}$$

$$\begin{aligned} v_{\mathbf{B}_3} &= \frac{1}{2}({}^{\mathbf{B}_3}V_r - {}^{\mathbf{B}_3}V)^T \mathbf{M}_{\mathbf{B}_3}({}^{\mathbf{B}_3}V_r - {}^{\mathbf{B}_3}V) \\ &\quad + \frac{1}{2}\sum_{i=1}^{13}\frac{(\theta_{\mathbf{B}_{3i}} - \widehat{\theta}_{\mathbf{B}_{3i}})^2}{\rho_{\mathbf{B}_{3i}}} \end{aligned} \tag{75}$$

Similarly to Eqs. (65)–(68), the time derivatives of $v_{\mathbf{B}_0}$, $v_{\mathbf{B}_1}$, $v_{\mathbf{B}_2}$, and $v_{\mathbf{B}_3}$ can be derived as

$$\begin{aligned} \dot{v}_{\mathbf{B}_0} &\le ({}^{\mathbf{B}_0}V_r - {}^{\mathbf{B}_0}V)^T \mathbf{M}_{\mathbf{B}_0} \frac{d}{dt}({}^{\mathbf{B}_0}V_r - {}^{\mathbf{B}_0}V) \\ &\le -({}^{\mathbf{B}_0}V_r - {}^{\mathbf{B}_0}V)^T \mathbf{K}_{\mathbf{B}_0}({}^{\mathbf{B}_0}V_r - {}^{\mathbf{B}_0}V) \\ &\quad + ({}^{\mathbf{B}_0}V_r - {}^{\mathbf{B}_0}V)^T ({}^{\mathbf{B}_0}F_r^* - {}^{\mathbf{B}_0}F^*) \end{aligned} \tag{76}$$

$$\begin{aligned} \dot{v}_{\mathbf{B}_1} &\le ({}^{\mathbf{B}_1}V_r - {}^{\mathbf{B}_1}V)^T \mathbf{M}_{\mathbf{B}_1} \frac{d}{dt}({}^{\mathbf{B}_1}V_r - {}^{\mathbf{B}_1}V) \\ &\le -({}^{\mathbf{B}_1}V_r - {}^{\mathbf{B}_1}V)^T \mathbf{K}_{\mathbf{B}_1}({}^{\mathbf{B}_1}V_r - {}^{\mathbf{B}_1}V) \\ &\quad + ({}^{\mathbf{B}_1}V_r - {}^{\mathbf{B}_1}V)^T ({}^{\mathbf{B}_1}F_r^* - {}^{\mathbf{B}_1}F^*) \end{aligned} \tag{77}$$

$$\begin{aligned}\dot{v}_{\mathbf{B}_2} &\leq ({}^{\mathbf{B}_2}V_r - {}^{\mathbf{B}_2}V)^T \mathbf{M}_{\mathbf{B}_2} \frac{d}{dt} ({}^{\mathbf{B}_2}V_r - {}^{\mathbf{B}_2}V) \\ &\leq -({}^{\mathbf{B}_2}V_r - {}^{\mathbf{B}_2}V)^T \mathbf{K}_{\mathbf{B}_2} ({}^{\mathbf{B}_2}V_r - {}^{\mathbf{B}_2}V) \\ &\quad +({}^{\mathbf{B}_2}V_r - {}^{\mathbf{B}_2}V)^T ({}^{\mathbf{B}_2}F_r^* - {}^{\mathbf{B}_2}F^*) \end{aligned} \tag{78}$$

$$\begin{aligned}\dot{v}_{\mathbf{B}_3} &\leq ({}^{\mathbf{B}_3}V_r - {}^{\mathbf{B}_3}V)^T \mathbf{M}_{\mathbf{B}_3} \frac{d}{dt} ({}^{\mathbf{B}_3}V_r - {}^{\mathbf{B}_3}V) \\ &\leq -({}^{\mathbf{B}_3}V_r - {}^{\mathbf{B}_3}V)^T \mathbf{K}_{\mathbf{B}_3} ({}^{\mathbf{B}_3}V_r - {}^{\mathbf{B}_3}V) \\ &\quad +({}^{\mathbf{B}_3}V_r - {}^{\mathbf{B}_3}V)^T ({}^{\mathbf{B}_3}F_r^* - {}^{\mathbf{B}_3}F^*) \end{aligned} \tag{79}$$

Then, it follows from Definition 2.16 in [16] and Eqs. (8), (26), (30), (31), and (54), that the last term of Eq. (76) can be expressed as

$$\begin{aligned}&({}^{\mathbf{B}_0}V_r - {}^{\mathbf{B}_0}V)^T ({}^{\mathbf{B}_0}F_r^* - {}^{\mathbf{B}_0}F^*) \\ &\quad = ({}^{\mathbf{B}_0}V_r - {}^{\mathbf{B}_0}V)^T \left[({}^{\mathbf{B}_0}F_r - {}^{\mathbf{B}_0}F) - {}^{\mathbf{B}_0}\mathbf{U}_{\mathbf{B}_1}({}^{\mathbf{B}_1}F_r - {}^{\mathbf{B}_1}F)\right] \\ &\quad = p_{\mathbf{B}_0} - ({}^{\mathbf{B}_0}V_r - {}^{\mathbf{B}_0}V)^T\, {}^{\mathbf{B}_0}\mathbf{U}_{\mathbf{B}_1}({}^{\mathbf{B}_1}F_r - {}^{\mathbf{B}_1}F) \\ &\quad = p_{\mathbf{B}_0} - p_{\mathbf{B}_1} \end{aligned} \tag{80}$$

where $p_{\mathbf{B}_0}$ and $p_{\mathbf{B}_1}$ are *virtual power flow* terms, in view of Definition 2.16 in [16].

Similarly, the last term of Eq. (77) can be rewritten, according to Eqs. (9), (25), (29), (30), (31), (53), and (57), as

$$\begin{aligned}&({}^{\mathbf{B}_1}V_r - {}^{\mathbf{B}_1}V)^T ({}^{\mathbf{B}_1}F_r^* - {}^{\mathbf{B}_1}F^*) \\ &\quad = ({}^{\mathbf{B}_1}V_r - {}^{\mathbf{B}_1}V)^T \left[({}^{\mathbf{B}_1}F_r - {}^{\mathbf{B}_1}F) - {}^{\mathbf{B}_1}\mathbf{U}_{\mathbf{B}_2}({}^{\mathbf{B}_2}F_r - {}^{\mathbf{B}_2}F)\right] \\ &\quad = \left[{}^{\mathbf{B}_0}\mathbf{U}_{\mathbf{B}_1}^T({}^{\mathbf{B}_0}V_r - {}^{\mathbf{B}_0}V) + \mathbf{z}(\dot{q}_{1r} - \dot{q}_1)\right]^T ({}^{\mathbf{B}_1}F_r - {}^{\mathbf{B}_1}F) - p_{\mathbf{B}_2} \\ &\quad = ({}^{\mathbf{B}_0}V_r - {}^{\mathbf{B}_0}V)^T\, {}^{\mathbf{B}_0}\mathbf{U}_{\mathbf{B}_1}({}^{\mathbf{B}_1}F_r - {}^{\mathbf{B}_1}F) - p_{\mathbf{B}_2} \\ &\quad + \mathbf{z}^T(\dot{q}_{1r} - \dot{q}_1)\mathbf{z}u_1(f_{c1r} - f_c) \\ &\quad = p_{\mathbf{B}_1} - p_{\mathbf{B}_2} + (\dot{x}_{c1r} - \dot{x}_1)(f_{c1r} - f_{c1}) \end{aligned} \tag{81}$$

where $p_{\mathbf{B}_1}$ and $p_{\mathbf{B}_2}$ are *virtual power flow* terms. Further, the last term in Eq. (78), according to Eqs. (10), (24), (28), (31), (32), (53) and (56), as

$$\begin{aligned}&({}^{\mathbf{B}_2}V_r - {}^{\mathbf{B}_2}V)^T ({}^{\mathbf{B}_2}F_r^* - {}^{\mathbf{B}_2}F^*) \\ &\quad = ({}^{\mathbf{B}_2}V_r - {}^{\mathbf{B}_2}V)^T \left[({}^{\mathbf{B}_2}F_r - {}^{\mathbf{B}_2}F) - {}^{\mathbf{B}_2}\mathbf{U}_{\mathbf{B}_3}({}^{\mathbf{B}_3}F_r - {}^{\mathbf{B}_3}F)\right] \\ &\quad = \left[{}^{\mathbf{B}_1}\mathbf{U}_{\mathbf{B}_2}^T({}^{\mathbf{B}_1}V_r - {}^{\mathbf{B}_1}V) + \mathbf{z}(\dot{q}_{2r} - \dot{q}_2)\right]^T ({}^{\mathbf{B}_2}F_r - {}^{\mathbf{B}_2}F) \\ &\quad - ({}^{\mathbf{B}_2}V_r - {}^{\mathbf{B}_2}V)^T\, {}^{\mathbf{B}_2}\mathbf{U}_{\mathbf{B}_3}({}^{\mathbf{B}_3}F_r - {}^{\mathbf{B}_3}F) \\ &\quad = ({}^{\mathbf{B}_1}V_r - {}^{\mathbf{B}_1}V)^T\, {}^{\mathbf{B}_1}\mathbf{U}_{\mathbf{B}_2}({}^{\mathbf{B}_2}F_r - {}^{\mathbf{B}_2}F) \\ &\quad - ({}^{\mathbf{B}_2}V_r - {}^{\mathbf{B}_2}V)^T\, {}^{\mathbf{B}_2}\mathbf{U}_{\mathbf{B}_3}({}^{\mathbf{B}_3}F_r - {}^{\mathbf{B}_3}F) \\ &\quad + \mathbf{z}^T(\dot{q}_{2r} - \dot{q}_2)({}^{\mathbf{B}_2}F_r - {}^{\mathbf{B}_2}F) \\ &\quad = p_{\mathbf{B}_2} - p_{\mathbf{B}_3} + (\dot{x}_{c2r} - \dot{x}_{c2})(f_{c2r} - f_{c2}) \end{aligned} \tag{82}$$

where $p_{\mathbf{B}_2}$ and $p_{\mathbf{B}_3}$ are *virtual power flow* terms.

Finally, the last term of Eq. (79) can be derived to be, according to Eqs. (10), (11), (15), (23), (27), (32), (33), (37), (51), and (55), as

$$\begin{aligned}&({}^{\mathbf{B}_3}V_r - {}^{\mathbf{B}_3}V)^T ({}^{\mathbf{B}_3}F_r^* - {}^{\mathbf{B}_3}F^*) \\ &\quad = ({}^{\mathbf{B}_3}V_r - {}^{\mathbf{B}_3}V)^T \left[({}^{\mathbf{B}_3}F_r - {}^{\mathbf{B}_3}F) - {}^{\mathbf{B}_3}\mathbf{U}_{\mathbf{B}_4}({}^{\mathbf{B}_4}F_r - {}^{\mathbf{B}_4}F)\right] \\ &\quad = \left[{}^{\mathbf{B}_2}\mathbf{U}_{\mathbf{B}_3}^T({}^{\mathbf{B}_2}V_r - {}^{\mathbf{B}_2}V)^T + \mathbf{z}^T(\dot{q}_{3r} - \dot{q}_3)\right]^T ({}^{\mathbf{B}_3}F_r - {}^{\mathbf{B}_3}F) \\ &\quad - ({}^{\mathbf{B}_3}V_r - {}^{\mathbf{B}_3}V)^T\, {}^{\mathbf{B}_3}\mathbf{U}_{\mathbf{B}_4}({}^{\mathbf{B}_4}F_r - {}^{\mathbf{B}_4}F) \\ &\quad = p_{\mathbf{B}_3} + (\dot{x}_{c3r} - \dot{x}_{c3})(f_{c3r} - f_{c3}) \\ &\quad - ({}^{\mathbf{B}_3}V_r - {}^{\mathbf{B}_3}V)^T\, {}^{\mathbf{B}_3}\mathbf{U}_{\mathbf{B}_4}({}^{\mathbf{B}_4}F_r - {}^{\mathbf{B}_4}F) \\ &\quad = p_{\mathbf{B}_3} + (\dot{x}_{c3r} - \dot{x}_{c3})(f_{c3r} - f_{c3}) \\ &\quad - ({}^{\mathbf{B}_3}V_r - {}^{\mathbf{B}_3}V)^T\, {}^{\mathbf{B}_3}\mathbf{U}_{\mathbf{B}_4}({}^{\mathbf{B}_4}F_r - {}^{\mathbf{B}_4}F) \\ &\quad = p_{\mathbf{B}_3} - ({}^{\mathbf{B}_4}V_r - {}^{\mathbf{B}_4}V)^T ({}^{\mathbf{B}_4}F_r - {}^{\mathbf{B}_4}F) + (\dot{x}_{c3r} - \dot{x}_{c3})(f_{c3r} - f_{c3}) \\ &\quad = p_{\mathbf{B}_3} - p_{\mathbf{B}_4} + (\dot{x}_{c3r} - \dot{x}_{c3})(f_{c3r} - f_{c3}) \end{aligned} \tag{83}$$

where $p_{\mathbf{B}_3}$ and $p_{\mathbf{B}_4}$ are *virtual power flow* terms for third rigid actuated joint and the third rigid link.

It follows from Eq. (71) that the time derivation of v_{sw} can be rewritten, by using Eqs. (76)–(83), as

$$\begin{aligned}\dot{v}_{sw} &\leq \dot{v}_{\mathbf{B}_0} + \dot{v}_{\mathbf{B}_1} + \dot{v}_{\mathbf{B}_2} + \dot{v}_{\mathbf{B}_3} \\ &\leq -({}^{\mathbf{B}_0}V_r - {}^{\mathbf{B}_0}V)^T \mathbf{K}_{\mathbf{B}_0} ({}^{\mathbf{B}_0}V_r - {}^{\mathbf{B}_0}V) \\ &\quad -({}^{\mathbf{B}_1}V_r - {}^{\mathbf{B}_1}V)^T \mathbf{K}_{\mathbf{B}_1} ({}^{\mathbf{B}_1}V_r - {}^{\mathbf{B}_1}V) \\ &\quad -({}^{\mathbf{B}_2}V_r - {}^{\mathbf{B}_2}V)^T \mathbf{K}_{\mathbf{B}_2} ({}^{\mathbf{B}_2}V_r - {}^{\mathbf{B}_2}V) \\ &\quad -({}^{\mathbf{B}_3}V_r - {}^{\mathbf{B}_3}V)^T \mathbf{K}_{\mathbf{B}_3} ({}^{\mathbf{B}_3}V_r - {}^{\mathbf{B}_3}V) \\ &\quad +(\dot{x}_{c1r} - \dot{x}_1)(f_{c1r} - f_{c1}) + (\dot{x}_{c2r} - \dot{x}_2)(f_{c2r} - f_{c2}) \\ &\quad +(\dot{x}_{c3r} - \dot{x}_3)(f_{c3r} - f_{c3}) + p_{\mathbf{B}_0} - p_{\mathbf{B}_4} \end{aligned} \tag{84}$$

In Eq. (84), the appearance of $(\dot{x}_{c1r} - \dot{x}_{c1})(f_{c1r} - f_{c1})$, $(\dot{x}_{c2r} - \dot{x}_{c2})(f_{c2r} - f_{c2})$, and $(\dot{x}_{c3r} - \dot{x}_{c3})(f_{c3r} - f_{c3})$ prevents the virtual stability. The virtual stability analysis can be complemented by considering the hydraulic dynamics equations in [16] and [10] and corresponding stability analysis.

Consider that the spherical wrist has one *driven* VCP associated with frame $\{\mathbf{B}_0\}$ and one *driving* VCP associated with frame $\{\mathbf{B}_4\}$. Then, using (71) and (84) completes the proof of the *virtual stability* of the spherical wrist, in the sense of Definition 2.17 in [16], ensuring that ${}^{\mathbf{B}_j}V_r - {}^{\mathbf{B}_j}V \in L_2 \bigcap L_\infty \; \forall j \in \{0,1,2,3\}$. ■

5.3 Stability of the Entire System

The entire system is stable in view of Theorem 2.1 in [16] if all the VPFs are canceled out in the summation of the time derivative of all non-negative accompanying functions and all the subsystems are proved to be virtual stable. In view of Theorem 2.1 in [16], the stability of the entire system can be ensured, by analyzing the virtual stability of the subsystems. If all of the VPFs are canceled out in the summation of the time derivative of all the non-negative accompanying functions, in view of Lemma 2.3 in [16], and if all the subsystems are proved to be virtually stable, then the system is stable. The stability analysis for the manipulator arm (see Fig. 1) is specified in [18]. The stability analysis for the backlash compensation is given in [5].

6 EXPERIMENTAL RESULTS

The effectiveness and control performance of the proposed controller is presented with a full-scale commercial Hiab 033 hydraulic manipulator (see Fig. 1) with a hydraulically actuated spherical wrist. Experimental setup for the wrist mechanics consists of the following hardware components:

1. dSpace ds1005 with a sampling rate 500 Hz
2. Eckart E3150-360° (*open chain* 1 and *open chain* 3 in Fig. 3)
3. Eckart E3150-180° (*open chain* 2 in Fig. 3)
4. Bosch Rexroth NG6 size servo solenoid valve (40 l/min at Δp = 3.5 MPa per notch) for all wrist joints
5. IFM PA3521 pressure transmitters (range 25 MPa)
6. Fraba Incremental encoders (16384 inc/rev) for all wrist joint angles
7. A gripper tool with a mass of 90 kg
8. A 3-DOF spherical wrist mechanism with total mass 200 kg

The components for the manipulator arm are listed in [19].

In the experiment, the proposed controller for the spherical wrist was tested using a point-to-point quintic reference trajectory for the wrist orientation. Fig. 4 shows the designed orientation trajectory, when the manipulator tip position reference was fixed. The trajectory is designed so that the maximum control signal of the proposed nonlinear controller is about 70%. Fig. 5 shows the orientation errors of the wrist joint, when the proposed nonlinear controller was used and when the manipulator was driven with well-tuned p-controller. As Fig. 5 shows, the orientation errors of all the wrist joints were significantly lower than those with the p-controlled manipulator. In the experiment, the maximum angular velocity for the first wrist joint, it was $60^\circ/s$, for the second joint $20^\circ/s$, and for the third joint the maximum velocity was $60^\circ/s$. The spherical wrist consisted of serial connected rotary actuators; for this reason, the orientation error of every wrist joint affect the error at the tip of the wrist mechanism. In Fig. 5, the total orientation error is presented. As this shows, the dynamic total error was significantly lower with the proposed controller with the p-controller. In Fig. 5, the root-square-mean-error (RMSE) values to each wrist are presented in brackets. These values indicates that proposed controller provide better control performance compared to p-controller.

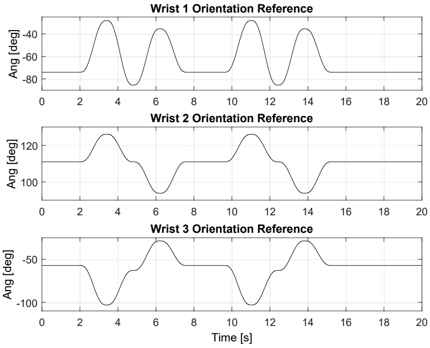

FIGURE 4. Orientation references for the wrist joints

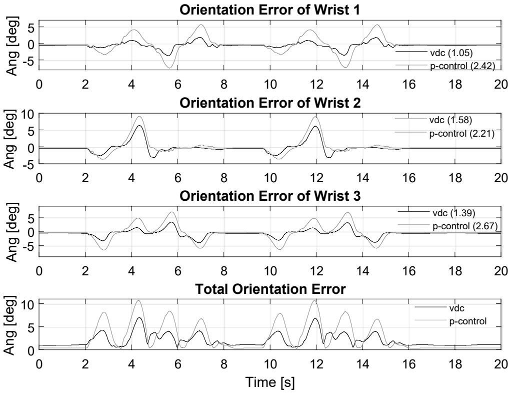

FIGURE 5. Wrist joint orientation errors with fixed crane tip position

Fig. 6 shows, the orientation errors of the spherical wrist joints then the manipulator tip was also moving. In this case, the maximum angular velocity for the first wrist joint, it was $40^\circ/s$, for the second joint, it was $20^\circ/s$ and for the third joint the maximum velocity $30^\circ/s$. As Fig. 6 shows the orientation error with the proposed nonlinear controller was lower than with p-controlled manipulator. Also, the RMSE values of the proposed controller was lower compared to p-controlled system. By comparing Fig. 5 and 6, it can be noticed that the angular velocities did not affect the total error of the proposed controller.

7 CONCLUSIONS

This paper focused on proposing an NMB controller with parameter adaptation for the hydraulic rotary actuated spherical wrist. The stability of the entire system was proven with a rigorous stability analysis. The experimental results with a full-size commercial manipulator arm with a 3-DOF spherical wrist verified the effectiveness of the proposed controller.

The proposed controller for the spherical wrist incorporated a previously designed state-of-the-art control for the hydraulic manipulator, which allowed to the VDC approach to be extended to cover a 6-DOF hydraulic manipulator. This study focused on

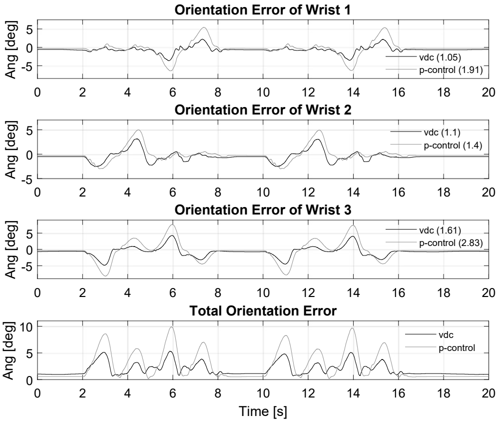

FIGURE 6. Wrist joint orientation errors

presenting the position control in a free-space. The 6-DOF manipulator controller will be extended to cover the contact force control in future studies.

REFERENCES

[1] Kraft TeleRobotics, 2019. *Undersea manipulator*. [online], accessed 12.07.2019, available: http://www.krafttelerobotics.com/products/predator.htm.

[2] Cyberntix, 2019. *Cybernetix's MAESTRO*. [online], accessed 12.07.2019, available: http://www.cybernetix.fr/en/portfolio/maestro-system/.

[3] Sivčev, S., Coleman, J., Omerdić, E., Dooly, G., and Toal, D., 2018. "Underwater manipulators: A review". *Ocean Engineering,* ***163***, pp. 431–450.

[4] Yao, J., Jiao, Z., Ma, D., and Yan, L., 2014. "High-accuracy tracking control of hydraulic rotary actuators with modeling uncertainties". *IEEE/ASME Trans. on Mech.,* ***19***(2), pp. 633–641.

[5] Mustalahti, P., and Mattila, J., 2018. "Nonlinear model-based controller design for a hydraulic rack and pinion gear actuator". In BATH/ASME 2018 Symp. on Fluid Power and Motion Control, ASME, pp. V001T01A020–V001T01A020.

[6] Heintze, J., Van Schothorst, G., Van der Weiden, A., and Teerhuis, P., 1993. "Modeling and control of an industrial hydraulic rotary vane actuator". In Proceedings of 32nd IEEE Conference on Decision and Control, IEEE, pp. 1913–1918.

[7] Tao, G., and Kokotovic, P. V., 1995. "Adaptive control of system with unknown output backlash". *IEEE Trans. on Automatic Control,* ***40***(2), pp. 326–330.

[8] Zhu, W.-H., and Piedboeuf, J.-C., 2005. "Adaptive output force tracking control of hydraulic cylinders with applications to robot manipulators". *Journal of dynamic systems, measurement, and control,* ***127***(2), pp. 206–217.

[9] Mattila, J., Koivumäki, J., Caldwell, D. G., and Semini, C., 2017. "A survey on control of hydraulic robotic manipulators with projection to future trends". *IEEE/ASME Trans. on Mechatronics,* ***22***(2), pp. 669–680.

[10] Koivumäki, J., and Mattila, J., 2015. "Stability-guaranteed force-sensorless contact force/motion control of heavy-duty hydraulic manipulators". *IEEE Trans. Robotics,* ***31***(4), pp. 918–935.

[11] Koivumäki, J., and Mattila, J., 2017. "Stability-guaranteed impedance control of hydraulic robotic manipulators". *IEEE/ASME Trans. Mechatronics,* ***22***(2), pp. 601–612.

[12] Koivumäki, J., and Mattila, J., 2017. "Stability-guaranteed impedance control of hydraulic robotic manipulators". *IEEE/ASME Trans. on Mechatronics,* ***22***(2), pp. 601–612.

[13] Koivumäki, J., Zhu, W.-H., and Mattila, J., 2019. "Energy-efficient and high-precision control of hydraulic robots". *Control Engineering Practice,* ***85***, pp. 176–193.

[14] Lampinen, S., Koivumäki, J., and Mattila, J., 2018. "Full-dynamics-based bilateral teleoperation of hydraulic robotic manipulators". In 2018 IEEE 14th International Conference on Automation Science and Engineering (CASE), IEEE, pp. 1343–1350.

[15] Suomalainen, M., Koivumäki, J., Lampinen, S., Kyrki, V., and Mattila, J., 2018. "Learning from demonstration for hydraulic manipulators". In 2018 IEEE/RSJ International Conference on Intelligent Robots and Systems (IROS), IEEE, pp. 3579–3586.

[16] Zhu, W.-H., 2010. *Virtual decomposition control: toward hyper degrees of freedom robots*, Vol. 60. Springer Science & Business Media.

[17] Zhu, W.-H., Xi, Y.-G., Zhang, Z.-J., Bien, Z., and De Schutter, J., 1997. "Virtual decomposition based control for generalized high dimensional robotic systems with complicated structure". *IEEE Trans. Robot. Autom.,* ***13***(3), pp. 411–436.

[18] Koivumäki, J., and Mattila, J., 2015. "High performance nonlinear motion/force controller design for redundant hydraulic construction crane automation". *Automation in Construction,* ***51***, pp. 59–77.

[19] Mustalahti, P., Koivumäki, J., and Mattila, J., 2017. "Stability-guaranteed anti-sway controller design for a redundant articulated hydraulic manipulator in the vertical plane". In ASME/BATH Symp. on Fluid Power and Motion Control, ASME, pp. V001T01A031–V001T01A031.

PUBLICATION
V

Position-Based Impedance Control Design for a Hydraulically Actuated Series Elastic Actuator

P. Mustalahti and J. Mattila

Energies, vol. 15, no. 7
DOI: 10.3390/en15072503

energies

Article

Position-Based Impedance Control Design for a Hydraulically Actuated Series Elastic Actuator

Pauli Mustalahti * and **Jouni Mattila**

Faculty of Engineering and Natural Sciences, Tampere University, 33720 Tampere, Finland; jouni.mattila@tuni.fi
* Correspondence: pauli.mustalahti@tuni.fi

Abstract: Series elastic actuators (SEAs) have become a common actuation method in torque-controlled electric lightweight arm applications that physically interact with the environment in assembly tasks. Compared to traditional actuators, SEAs can provide high force fidelity, shock tolerance, and force sensing for interaction control. Considering inherent system dynamics and the variable stiffness of the fluid, the control design for hydraulic SEAs (HSEAs) that lead into fifth-order system is a challenging task. As a novelty, a full state feedback controller design for the developed fifth-order HSEA system is presented to serve as an inner-loop controller to handle highly nonlinear dynamics behavior. In addition, as an outer-loop impedance controller for HSEAs in heavy-duty applications, the position-based impedance controller is designed to handle control of the HSEA system during the contact motion. Experimental results with a one-degree-of-freedom real-size experimental setup with a payload of 200 kilos demonstrates the effectiveness of the proposed HSEA control methods both in the free-space motion and in a contact impedance motion.

Keywords: elastic actuator; heavy duty manipulator; impedance control

Citation: Mustalahti, P.; Mattila, J. Position-Based Impedance Control Design for a Hydraulically Actuated Series Elastic Actuator. *Energies* **2022**, *15*, 2503. https://doi.org/10.3390/en15072503

Academic Editor: Wencheng Guo

Received: 7 March 2022
Accepted: 27 March 2022
Published: 29 March 2022

1. Introduction

In the future, the rapid development of robotics will enable the collaboration of humans and robots in factories and in our houses. A fundamental capability for these robots is safe, smooth, and accurate control in uncertain environments. Unpredictable interactions between environments and robots cause challenges for stable position control design, because environmental dynamics affect closed-loop systems. Thus, force control is needed to handle uncertain environmental dynamics. Force control methods have been subject to research for many years.

Series elastic actuators (SEAs) are widely used in torque-controlled lightweight electric applications [1–4]. Compared to traditional actuators, a SEA provides high force fidelity, shock tolerance, and force sensing [5] by placing a spring between the power output shaft of the actuator and the environment. SEAs have been developed, for example, for electric humanoid robots [6], teleoperation [7], and walking robots [8]. In addition, the hydraulic SEA (HSEA) for lightweight arms is presented in [9–11]. Compared with electric SEAs, HSEAs provide higher power-to-weight ratios but lower speed ratios. However, most of these studies have focused on lightweight output force cases. In this research, as a novelty, we focus on studying the design control architecture for SEAs in heavy-duty manipulation. In addition, selection of the spring stiffness for the HSEA system in heavy-duty applications is considered.

Impedance control methods for torque-controlled SEAs have been actively researched [12–15]. As explained in [13], a cascade control structure is used to isolated slow outer-loop controller from nonlinear dynamics of the controlled system by using fast inner-loop control structure. A disturbance observer-based control for SEA has been presented [12]. In addition, control stability in different environments has been studied [14]. Control design for a linear electric actuator is presented in [16], where high motor voltage with a drivetrain is used to produce continuous actuator force.

In [15], a force-controllable HSEA is modeled as a second-order system that consists of an integrator (cylinder model) and a first-order delay (servo-valve model). Thus, the nonlinear dynamics of the fluid are neglected. Considering the inherent system dynamics and the variable stiffness of the fluid, HSEAs lead into a fifth-order model. As demonstrated in [17], full model-based control methods provide high control performance with heavy-duty hydraulic systems compared to other methods. In this study, we focus on analyzing a fifth-order model of an HSEA to design a full state feedback controller to handle the nonlinear dynamic behavior of hydraulics. The proposed state-feedback controller is used as an inner-loop controller to provide high control performance for the HSEA system. In [18–20], performance analyses and simulation results with HSEA for a heavy-duty load are given, however the experimental results are still missing. The experimental results with higher load mass are presented in [21]. However, considering the real-size heavy-duty manipulator, the used load mass is still low.

As presented in [22,23], the outer-loop controller can be implemented using a cylinder position error to describe the interaction force between the cylinder and the environment. In this study, as an novelty, we design the position-based impedance controller for the HSEA. The proposed impedance controller is used as an outer-level controller. Considering the fast dynamics of the spring and the slower dynamics of the hydraulics, a control architecture with a fast inner-loop controller and a slower outer-level controller is needed to handle control of the HSEA system. The experimental results are used to verify the control performance of the proposed control architecture for the HSEA system.

This paper is organized as follows. Section 2 introduces the linear modeling of the HSEA and the inner-loop state feedback controller. In Section 3, the outer-loop position-based impedance controller is presented. The experimental results with a one-degree-of-freedom (DOF) real-size experimental setup are given in Section 4. Finally, conclusions are given in Section 5.

2. Modeling of the Hydraulic Series Elastic Actuator

SEAs use a spring in series with an actuator to decouple the actuator from the environment. As illustrated in Figure 1, the HSEA consists of a hydraulic cylinder with a mechanical spring and a hydraulic servo-valve. In Figure 1, the spring output force is symmetric in both directions to the symmetry of the spring stiffness. Therefore, the cylinder contact force can be estimated by measuring the spring compression. The hydraulic cylinder force can also be estimated via cylinder chamber pressures and cylinder areas. As Figure 1 shows, a 1-DOF HSEA is studied in a linear test case. Therefore, gravitational force does not affect the spring compression. In this study, spring compression, cylinder chamber pressures are measured, and cylinder position is measured. The supply pressure for the HSEA is 20 MPa.

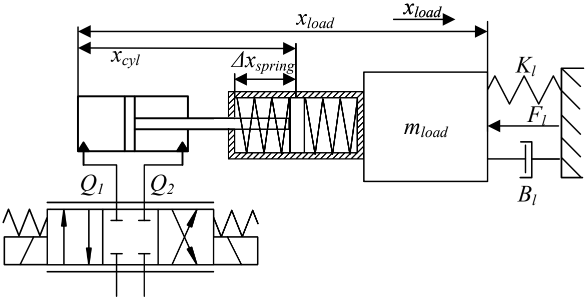

Figure 1. Schematic diagram of a HSEA.

In this study, the main focus is on designing a linear state feedback controller for the HSEA in Figure 1, to be used as an inner-loop controller for a outer-loop position-based impedance control. First, the fifth-order linear model for the HSEA is presented. Then, the state feedback controller for the system is defined. Finally, the selection of a spring for the HSEA is given.

2.1. State-Space Model for the HSEA

The linear model equations for the HSEA in Figure 1 can be derived by assuming that the hydraulic cylinder is symmetrical. Thus, the flow equations for a hydraulic servo-valve can be written as

$$Q_1 = A\dot{x}_{cyl} + C_v p_l + \frac{V_0}{B_{eff}}\dot{p}_1 \tag{1}$$

$$Q_2 = A\dot{x}_{cyl} + C_v p_l - \frac{V_0}{B_{eff}}\dot{p}_2 \tag{2}$$

where A is the area of a symmetrical cylinder, B_{eff} is an effective bulk modulus, V_0 is half of the total volume of the hydraulic cylinder, C_v is the total leakage coefficient of a piston, $\dot{x}_{cyl}$ is the cylinder velocity, p_1 and p_2 are cylinder chamber pressures, $\dot{p}_1$ and $\dot{p}_2$ are the derivatives of cylinder pressures in both chambers, and $p_l = p_1 - p_2$ is the pressure difference in the cylinder.

The flow continuity Equations (1) and (2) can be linearized, by assuming that $Q = Q_1 = Q_2$, as

$$Q = K_q x_v - K_c p_l \Rightarrow \\ \begin{cases} K_q x_v - K_c p_l = \dot{x}_{cyl} A + C_v p_l + \frac{V_0}{B_{eff}}\dot{p}_1 \\ K_q x_v - K_c p_l = \dot{x}_{cyl} A + C_v p_l - \frac{V_0}{B_{eff}}\dot{p}_2 \end{cases} \tag{3}$$

Here, x_v is the spool position of the hydraulic valve, K_q is the servo-valve flow gain, and K_c is the valve flow-pressure gain. In Equation (3), the servo-valve flow gain and valve flow pressure gain are used to linearize the flow-continuity equations. These gains can be defined by taking partial derivation of Equations (1) and (2):

$$K_q = \frac{\partial Q}{\partial x_v} \tag{4}$$

$$K_c = \frac{\partial Q}{\partial p_l} \tag{5}$$

Therefore, Equation (3) can be simplified as

$$\dot{p}_l = -\frac{2AB_{eff}}{V_0}\dot{x}_{cyl} - \frac{2K_{ce}B_{eff}}{V_0}p_l + \frac{2K_q B_{eff}}{V_0}x_v \tag{6}$$

where $K_{ce} = K_c + C_v$ is the total leakage coefficient in the cylinder.

Considering the HSEA in Figure 1, the dynamics equations for the system can be written as

$$m_l\ddot{x}_{load} + B_l\dot{x}_{load} + (K_s + K_l)x_{load} - K_s x_{cyl} + F_l = 0 \tag{7}$$

$$m_{cyl}\ddot{x}_{cyl} + B_{cyl}\dot{x}_{cyl} + K_s x_{cyl} - K_s x_{load} - Ap_l = 0 \tag{8}$$

where m_{cyl} is the mass of the piston, m_l is the load mass, x_{load} is the load position, F_l is the load contact force, B_l and B_{cyl} are the viscous damping coefficients of the load and the piston, K_s is the spring stiffness, and K_l is the spring stiffness of a load. In actual applications, the external load force and the damping of the environment are often absent. Therefore, coefficients K_l and B_l are neglected in this study.

Now, the state parameters for the HSEA can be defined by using Equations (3)–(8) as

$$x = [x_1\ x_2\ x_3\ x_4\ x_5] = [x_{load}\ x_{cyl}\ \dot{x}_{load}\ \dot{x}_{cyl}\ p_l] \tag{9}$$

Then, the state-space equations for the HSEA can be written as

$$\begin{aligned} x_1 &= x_3 \\ x_2 &= x_4 \\ x_3 &= -\tfrac{K_s}{m_l} x_1 + \tfrac{K_s}{m_l} x_2 \\ x_4 &= -\tfrac{K_s}{m_{cyl}} x_1 + \tfrac{K_s}{m_{cyl}} x_2 - \tfrac{B_{cyl}}{m_{cyl}} x_4 + \tfrac{A}{m_{cyl}} x_5 \\ x_5 &= -\tfrac{2B_{eff}A}{V_0} x_4 - \tfrac{2B_{eff}K_{ce}}{V_0} x_5 + \tfrac{2B_{eff}K_q}{V_0} u \end{aligned} \tag{10}$$

where *u* is the control voltage to the hydraulic valve. In the hydraulic servo-valve, the spool position follows directly from the control voltage. Finally, Equation (10) can be rewritten as

$$A = \begin{bmatrix} 0 & 0 & 1 & 0 & 0 \\ 0 & 0 & 0 & 1 & 0 \\ -\tfrac{K_s}{m_l} & \tfrac{K_s}{m_l} & 0 & 0 & 0 \\ -\tfrac{K_s}{m_{cyl}} & \tfrac{K_s}{m_{cyl}} & 0 & -\tfrac{B_{cyl}}{m_{cyl}} & \tfrac{A}{m_{cyl}} \\ 0 & 0 & 0 & -\tfrac{2B_{eff}A}{V_0} & -\tfrac{2B_{eff}K_{ce}}{V_0} \end{bmatrix} \tag{11}$$

$$B = \begin{bmatrix} 0 \\ 0 \\ 0 \\ 0 \\ \tfrac{2B_{eff}K_q}{V_0} \end{bmatrix} \tag{12}$$

2.2. State Feedback Controller Design for the HSEA

According to Equations (10)–(12), the full state feedback controller for the HSEA can be presented based on the work in [24] as

$$u = K_1(x_{load_{ref}} - x_1) - K_2(x_{ref} - x_2) + K_3x_3 - K_4x_4 - K_5x_5 \tag{13}$$

where the state feedback gains K_1, K_2, K_3, K_4, and K_5 are tuned such that the position error of the cylinder is minimized. In Equation (13), $x_{load_{ref}}$ is desired position for load, which is provided as a reference trajectory to control system. Considering the fifth-order model for the HSEA in Equation (12), the proposed full-state feedback controller can be used to handle the dynamics of the HSEA system. The effectiveness of the proposed controller is verified by the experimental results.

2.3. Stiffness and Natural Frequency of the HSEA

As Figure 1 illustrated, the HSEA consists of a normal spring connected in series to a hydraulic spring. By connecting elastic springs in a series, the effective stiffness reduces. Thus, the system's equivalent stiffness can be presented as

$$\frac{1}{K_{sys}} = \frac{1}{K_s} + \frac{1}{K_{hyd}} \tag{14}$$

where K_{sys} is the system stiffness, K_{hyd} is the hydraulic spring stiffness, and K_s is the spring stiffness of normal. In Equation (14), the hydraulic stiffness can be defined by assuming that the pipes' volumes are small compared to the cylinder chamber volume. The minimum hydraulic stiffness occurs when the cylinder piston is centered. Therefore, the stiffness can be calculated as

$$K_{hyd} = \frac{4 * B_{eff} * A^2}{V_t} \tag{15}$$

The natural frequency of the HSEA can be presented by using Equations (14) and (15) as

$$\omega_n = \sqrt{\frac{K_{sys}}{m_l}} \tag{16}$$

As reported in [5,8], increasing the equivalent spring stiffness of the SEA increases the force bandwidth. On the other hand, minimizing the non-linearities requires a low spring stiffness. Simultaneously, increasing spring stiffness also increases the system's natural frequency. The purpose of the SEA is improving the contact-force control. Thus, the spring stiffness for the normal spring needs to be lower than the hydraulic stiffness. Considering heavy-duty manipulators with a low natural frequency (e.g., excavators and forwarders), the hydraulic resonance frequency is between 0.5 and 10 Hz. The selection of spring stiffness is a compromise for smooth response and force bandwidth.

The selected spring stiffness is illustrated in Figure 2. The selected spring stiffness is not linear due to the pre-tension length of the spring. The modeling parameters for the studied HSEA are presented in Table 1. Now, by substituting these parameters into Equations (14)–(16), we find that the value of the natural frequency is about 7.95 Hz.

Table 1. Parameter values for the HSEA.

Symbol	Value
d_{cyl}	32×10^{-3} m
d_{piston}	18×10^{-3} m
m_l	200 kg
l_{cyl}	0.4 m
B_{eff}	900 MPa
m_{cyl}	2 kg
C_v	1.16×10^{-12} m ^{5}/Ns
K_q	6.7×10^{-4} m^2/s
K_c	2.5×10^{-12} m^5/Ns

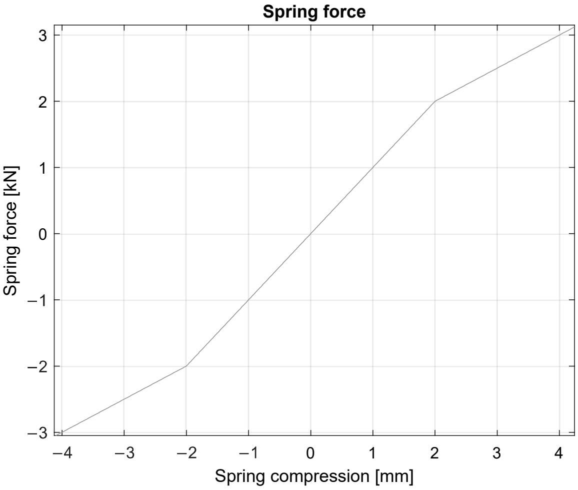

Figure 2. Spring force as a function of spring compression. Adapted with permission from [25]. Copyright 2020 IEEE.

3. Position-Based Impedance Control Design

Hydraulic manipulators are used in many industrial tasks to move heavy loads. Their grip on different objects inevitably causes interaction with the environment. Here, high contact forces may stress a manipulator or an object's mechanical structure. Therefore, impedance control design for these manipulators is needed. One method for implementing this for the HSEA is to use a position-based impedance controller using the cylinder position error to describe the cylinder contact force.

In Figure 1, the actual cylinder piston position is given by the cylinder piston position and the spring compression. Thus, the actual cylinder position can be calculated as

$$x_a = x_{cyl} + \Delta x_{spring} \tag{17}$$

where x_{cyl} is a measured cylinder piston position and Δx_{spring} is a spring compression. Now, the cylinder contact force can be estimated by calculating the position difference between a desired cylinder position and a measured position as

$$f_e = K_s(x_r - x_a) \tag{18}$$

where K_s is a spring stiffness, x_r is a desired cylinder position, and f_e is a contact force. The relation between a suitable position reference related to force error can be presented as

$$x_f = f_r - f_e \tag{19}$$

where f_r is the desired contact force. In this study, f_r is set to zero to minimize contact force.

The inverse dynamics control law with force measurement can be presented [22] as

$$\ddot{x}_e = {M_d}^{-1}(-B_d\dot{x}_e + K_d(x_e - x_f)) \tag{20}$$

where M_d, B_d, and K_d are the mass, damping, and stiffness matrices for the contact force dynamics, respectively, and x_e is the contact compression. In Equation (20), the contact dynamics stiffness matrix is assumed to be same as the spring stiffness. Along the vertical direction, the contact dynamics can be presented as

$$M_d = \frac{K_d}{\omega_n^2} \tag{21}$$

$$B_d = \zeta(2\sqrt{K_d M_d}) \tag{22}$$

where ω_n is the natural frequency of the system and ζ is the defined damping factor.

Now, the position reference for an inner-loop controller can be written as

$$x_{ref} = x_r - x_e \tag{23}$$

where x_r is a desired load position, which is usually provided as an reference trajectory for the control system.

Finally, the proposed position-based impedance controller in Equations (18)–(20) can be presented with the block diagram in Figure 3. Now, the connection between the outer impedance controller and the inner state-feedback controller is shown in Figure 4. In Figure 4, the desired reference x_r for a load position is generated with a point-to-point quintic reference trajectory. As Figure 4 demonstrates, in this study, we assume that all state variables for state-feedback controller can be measured.

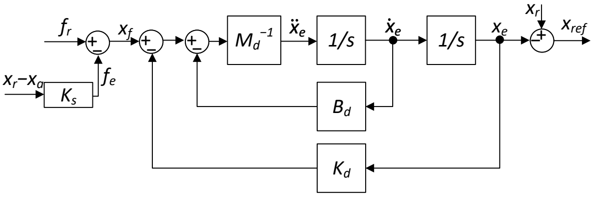

Figure 3. Block diagram for the position-based impedance controller.

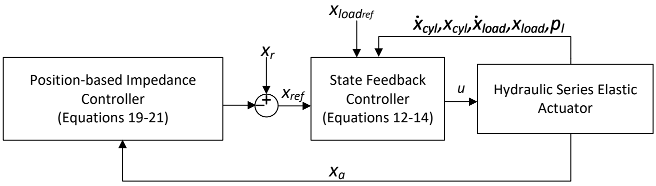

Figure 4. Control system block diagram.

4. Experimental Results

The effectiveness of the proposed position-based impedance controller is verified by a full-scale 1-DOF experimental setup, which is presented in Figure 5. The experimental setup consists of the following hardware components:

1. Industrial PC Beckhoff CX2030 with a sampling rate of 1000 Hz
2. Hydraulic cylinder with the dimensions ϕ32/18–400
3. Bosch Rexroth NG6 size servo solenoid valve (40 L/min at Δp = 3.5 MPa per notch)
4. Druck UNIK5000 pressure transmitter (range 25 MPa) for all pressures
5. MTS linear position sensor (range 0.015 m) for a spring compression
6. Heidenhain linear position sensor (range 0.54 m) for a cylinder position
7. Load mass 200 kg
8. Shell Tellus VG32 Hydraulic oil

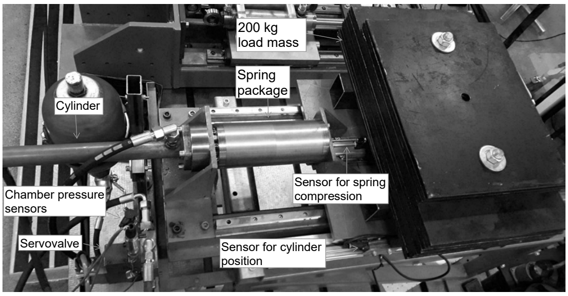

Figure 5. HSEA experimental setup.

In the experiments, the spring compression and cylinder position were measured using linear incremental position sensors. The hydraulic diagram for the experimental setup is presented in Figure 6. The supply pressure for the HSEA from the pump and the pressure relief were set to 20 MPa during the experiments.

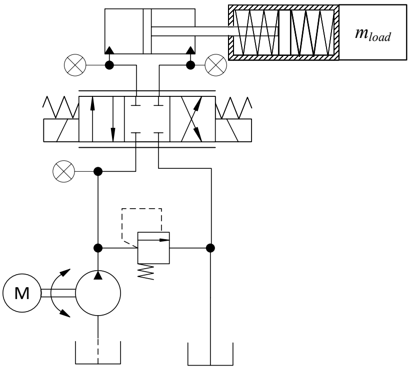

Figure 6. Hydraulic diagram for the experimental setup.

4.1. HSEA in a Free-Space Motion

First, the performance of the proposed controller was verified under free-space motion. Considering the HSEA system with heavy load, during a free-space motion, accelerations of the load could cause spring compression. In this case, we verify that the proposed controller can handle control of the HSEA system without contact motions and that proposed spring package can used to estimate the contact force.

In the HSEA, the system dynamics comprise slow system dynamics and fast spring dynamics simultaneously. Therefore, the fast inner-loop controller needs to handle the spring dynamics. In Figure 7, the HSEA was controlled using a step-like input for the cylinder position reference. As Figure 7 shows, the load pressure term in a state-feedback controller could be used to damp the oscillation of the spring. The corresponding spring compression is presented in Figure 8. As Figures 7 and 8 show, the spring compression's effects on the cylinder could be decreased using the proposed inner-loop controller. Considering the fast dynamics of the spring in Figure 8, the control results in Figure 7 verify that full-state feedback can be use to improve the control performance of the HSEA system. For this reason, a full model-based inner loop controller is needed to handle dynamics of the fifth-order HSEA system.

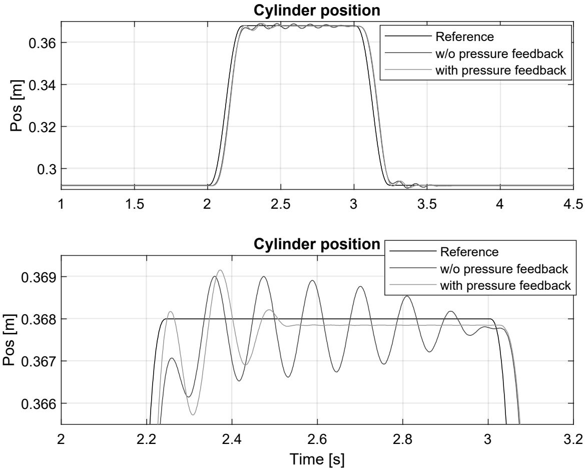

Figure 7. Cylinder position under free-space motion.

Figure 9 shows the results with the step-like position reference in free-space motion. The trajectory was designed so that valve control would be about 80% of its maximum. As Figure 9 shows, the proposed impedance controller affects the reference trajectory in a free-space motion due to spring compression. Even so, the system's steady-state errors and compression were low, as demonstrated in Equation (14) which shows spring stiffness effect in relation to the total stiffness of the HSEA system. For this reason, the selection of the spring stiffness affect the system dynamics. As presented in Section 2.3, the spring selection should do according to the natural frequency of the system. Now, Figure 9 shows the selected spring stiffness thus selected achieves a high steady-state control performance when the total system stiffness is lower than that without the spring.

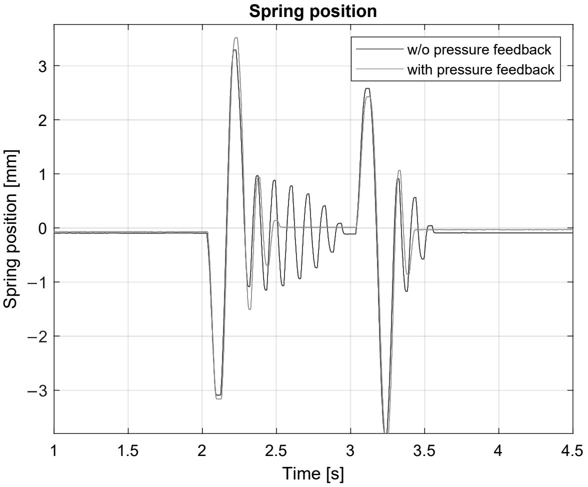

Figure 8. Spring compression in a free-space motion.

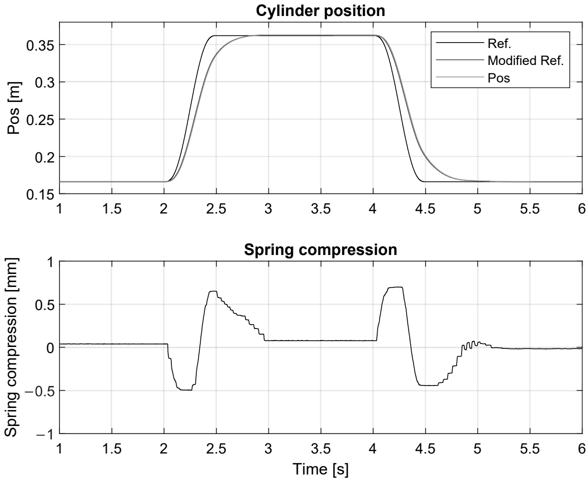

Figure 9. Cylinder position and spring compression in a free-space motion.

An SEA enables us to measure the cylinder force by using spring compression. In Figure 10, the cylinder force via spring stiffness (see Figure 2) and cylinder chamber pressures are presented when the impedance controller is not enabled. As Figure 10 shows, the spring force provides quite a smooth force measuring output. The cylinder force oscillates more during the transient motion. Moreover, cylinder friction and valve leakages affect the cylinder force. Considering, heavy-duty hydraulic systems, the cylinder force is typically estimated by using cylinder chamber pressures. Due to noisy pressure signals, it is typical that the estimated load force is noisy, which making force control of these kinds of systems difficult task. For these reason, measuring spring compression in HSEA systems allows contact force to be estimated without any force sensors.

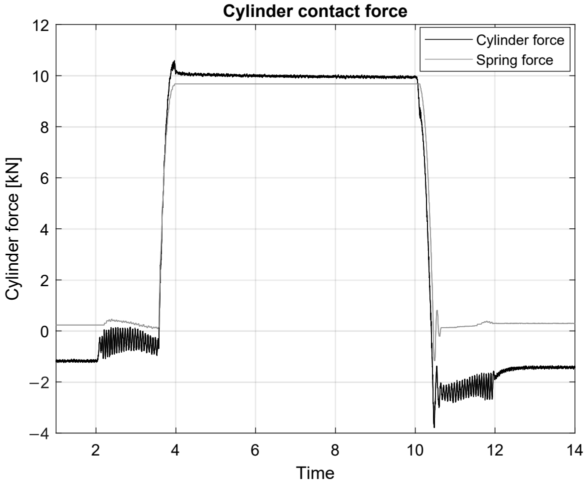

Figure 10. Spring force and cylinder pressure in a contact.

4.2. HSEA in a Contact Impedance Control Motion

The effectiveness of the proposed controller under contact impedance motion was verified by driving a cylinder against a rigid obstacle. Figure 11 displays a desired cylinder position reference, the position reference modified by impedance control (see Equation (23)), and the actual position during the impedance motion. The reference trajectory was designed so that the cylinder would be in contact with the environment for a period of ~7 s. As Figure 11 shows, the proposed controller could effectively compensate for the effect of the contact with the environment. The proposed controller's effect on the cylinder's contact force is presented in Figure 12 with the same reference as in Figure 11. As Figure 12 shows, the proposed controller could significantly decrease the cylinder contact force.

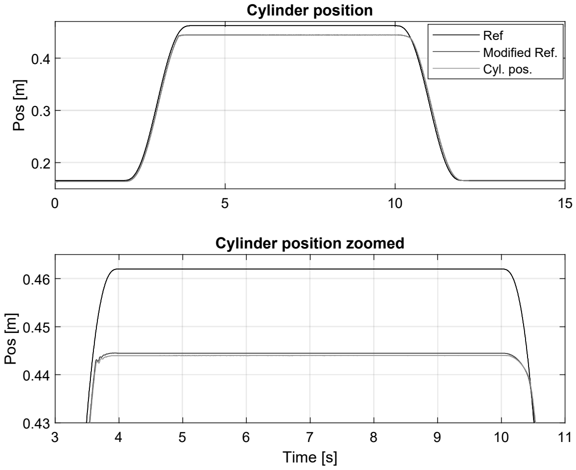

Figure 11. Cylinder position under contact motion.

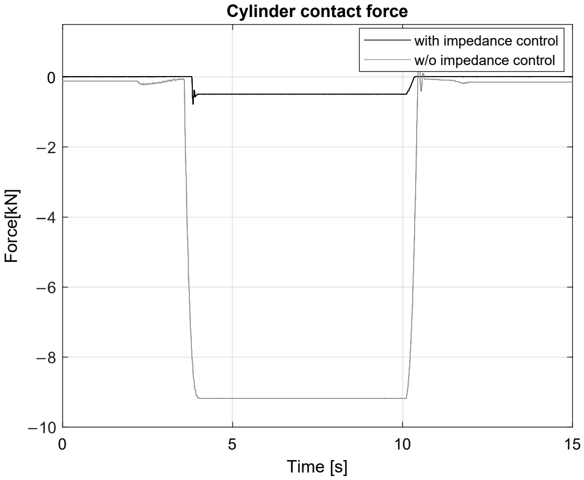

Figure 12. Spring compression with and without impedance control.

Finally, the effectiveness of the proposed controller is verified with various stiffness parameters in Equations (21) and (22). In Figure 13, the proposed control law in Equation (20) was tested with different contact force dynamics parameters, and it is shown that the proposed controller could also be used to compensate contact force effects in an environment with different contact stiffness. As the experimental results in Figure 13 demonstrate, the proposed HSEA system is robust against different environment stiffness.

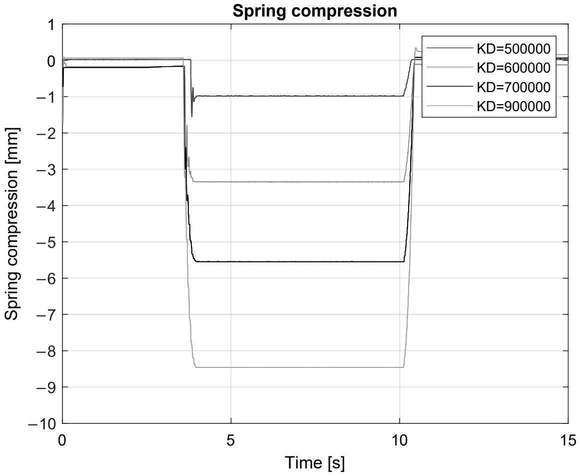

Figure 13. Spring compression with a different stiffness.

5. Conclusions

This paper focuses on studying HSEAs for heavy-duty manipulation applications. As a novelty, the full state-feedback controller for the fifth-order HSEA system is presented. Second, the proposed state-feedback controller is combined with the position-based impedance control to handle HSEA system control during contact motion. The effectiveness of the proposed state-feedback controller is verified in free-space motion. As the experimental results show, the proposed full state-feedback controller can effectively handle the controlling of the fifth-order system. The experimental results also verify that the proposed position-based impedance control enables significantly decreasing the contact force of HSEA system during the contact motion. In general, the experimental results show that the proposed controller structure can efficiently handle control of a highly non-linear HSEA system with a heavy load in free-space and contact motions. In addition, the spring stiffness selection is presented in this paper and the experimental results verify that selected spring stiffness is working with heavy loads. These experimental results provide a baseline for our future studies, in which we intend to study the proposed HSEA with a position-based impedance controller will be studied with a real-size multi-DOF hydraulic manipulator. Moreover, the gravitational force effects on an HSEA will be studied.

Author Contributions: Conceptualization, P.M.; methodology, P.M.; software, P.M.; validation, P.M.; formal analysis, P.M.; investigation, P.M.; resources, P.M.; data curation, P.M.; writing—original draft preparation, P.M.; writing—review and editing, P.M.; visualization, P.M.; supervision, J.M.; project administration, J.M.; funding acquisition, J.M. All authors have read and agreed to the published version of the manuscript.

Funding: This research received no external funding.

Institutional Review Board Statement: Not Applicable.

Informed Consent Statement: Not Applicable.

Data Availability Statement: This study did not report any data. Further data can be provided upon email request to the corresponding author.

Conflicts of Interest: The authors declare no conflicts of interest.

Nomenclature

SEA	Series Elastic Actuator
HSEA	Hydraulic Series Elastic Actuator
DOF	Degrees of Freedom
A	Cylinder area (m^2)
V_0	Half of the total cylinder volume (m^3)
x_{cyl}	Cylinder length (m)
$\dot{x}_{cyl}$	Cylinder velocity (m/s)
d_{cyl}	Cylinder diameter (m)
d_{piston}	Cylinder piston diameter (m)
m_l	Load mass (kg)
l_{cyl}	Cylinder stroke (m)
B_{eff}	Cylinder bulk modulus (MPa)
B_l	Viscous damping coefficients of load (N/m/s)
x_v	Spool position of the hydraulic valve (m)
K_q	Servo-valve flow gain (m^2/s)
K_c	Valve flow-pressure gain (m^5/Ns)
K_{ce}	Total leakage coefficient of a cylinder m^5/(Ns)
p_1	Cylinder A chamber pressure (MPa)
p_2	Cylinder B chamber pressure (MPa)
p_l	Cylinder chambers pressure difference (MPa)
F_l	Load contact force (N)
m_{cyl}	Cylinder mass (kg)
C_v	Total leakage coefficient of a piston m^5/(Ns)
B_{cyl}	Viscous damping coefficients of piston (N/m/s)
Δx_{spring}	Spring compression (m)
x_{load}	Load position (m)
$x_{load_{ref}}$	Desired position for load (m)
$\dot{x}_{load}$	Load velocity (m/s)
K_{sys}	System total spring stiffness (N/m)

K_{hyd}	Hydraulic system spring stiffness (N/m)
K_s	Spring stiffness (N/m)
x_f	Relation between a suitable position reference related to force error
f_r	Desired contact force (N)
f_e	Contact force (N)
u	Valve control voltage (V)
M_d	Mass matrix
B_d	Damping matrix
K_d	Stiffness matrix
ω_n	Natural frequency of the system (rad/s)
ζ	Damping factor

References

1. Albu-Schäffer, A.; Ott, C.; Hirzinger, G. A unified passivity-based control framework for position, torque and impedance control of flexible joint robots. *Int. J. Robot. Res.* **2007**, *26*, 23–39. [CrossRef]
2. Loughlin, C.; Albu-Schäffer, A.; Haddadin, S.; Ott, C.; Stemmer, A.; Wimböck, T.; Hirzinger, G. The DLR lightweight robot: Design and control concepts for robots in human environments. *Ind. Robot. Int. J.* **2007**, *34*, 376–385. [CrossRef]
3. Albu-Schaffer, A.; Ott, C.; Frese, U.; Hirzinger, G. Cartesian impedance control of redundant robots: Recent results with the DLR-light-weight-arms. In Proceedings of the 2003 IEEE International Conference on Robotics and Automation (Cat. No. 03CH37422), Taipei, Taiwan, 14–19 September 2003; Volume 3, pp. 3704–3709. [CrossRef]
4. Chen, T.; Casas, R.; Lum, P.S. An Elbow Exoskeleton for Upper Limb Rehabilitation with Series Elastic Actuator and Cable-Driven Differential. *IEEE Trans. Robot.* **2019**, *35*, 1464–1474. [CrossRef] [PubMed]
5. Pratt, G.A.; Williamson, M.M. Series elastic actuators. In Proceedings of the 1995 IEEE/RSJ International Conference on Intelligent Robots and Systems, Human Robot Interaction and Cooperative Robots, Pittsburgh, PA, USA, 5–9 August 1995; Volume 1, pp. 399–406. [CrossRef]
6. Lee, B.; Knabe, C.; Orekhov, V.; Hong, D. Design of a human-like range of motion hip joint for humanoid robots. In Proceedings of the ASME 2014 International Design Engineering Technical Conferences and Computers and Information in Engineering Conference, Buffalo, NY, USA, 17–20 August 2014. [CrossRef]
7. Budolak, D.; Ben-Tzvi, P. Series elastic actuation for improved transparency in time delayed haptic teleoperation. *Mechatronics* **2019**, *63*, 102278. [CrossRef]
8. Robinson, D.W.; Pratt, J.E.; Paluska, D.J.; Pratt, G.A. Series elastic actuator development for a biomimetic walking robot. In Proceedings of the 1999 IEEE/ASME International Conference on Advanced Intelligent Mechatronics (Cat. No. 99TH8399), Atlanta, GA, USA, 19–23 September 1999; pp. 561–568. [CrossRef]
9. Pratt, J.; Krupp, B.; Morse, C. Series elastic actuators for high fidelity force control. *Ind. Robot. Int. J.* **2002**, *29*, 234–241. [CrossRef]
10. Pratt, J.E.; Krupp, B.T. Series elastic actuators for legged robots. In Proceedings of the Unmanned Ground Vehicle Technology VI, International Society for Optics and Photonics, Orlando, FL, USA, 13–15 April 2014; Volume 5422, pp. 135–144. [CrossRef]
11. Kaminaga, H.; Otsuki, S.; Nakamura, Y. Development of high-power and backdrivable linear electro-hydrostatic actuator. In Proceedings of the 2014 IEEE-RAS International Conference on Humanoid Robots, Atlanta, GA, USA, 18–20 November 2014; pp. 973–978. [CrossRef]
12. Oh, S.; Kong, K. High-precision robust force control of a series elastic actuator. *IEEE/ASME Trans. Mechatron.* **2016**, *22*, 71–80. [CrossRef]
13. Zhao, Y.; Paine, N.; Jorgensen, S.J.; Sentis, L. Impedance control and performance measure of series elastic actuators. *IEEE Trans. Ind. Electron.* **2017**, *65*, 2817–2827. [CrossRef]
14. Calanca, A.; Fiorini, P. Understanding environment-adaptive force control of series elastic actuators. *IEEE/ASME Trans. Mechatron.* **2018**, *23*, 413–423. [CrossRef]
15. Robinson, D.W.; Pratt, G.A. Force controllable hydro-elastic actuator. In Proceedings of the 2000 ICRA. Millennium Conference. IEEE International Conference on Robotics and Automation. Symposia Proceedings (Cat. No. 00CH37065), San Francisco, CA, USA, 24–28 April 2000; Volume 2, pp. 1321–1327. [CrossRef]
16. Paine, N.; Oh, S.; Sentis, L. Design and control considerations for high-performance series elastic actuators. *IEEE/ASME Trans. Mechatron.* **2013**, *19*, 1080–1091. [CrossRef]
17. Mattila, J.; Koivumäki, J.; Caldwell, D.G.; Semini, C. A survey on control of hydraulic robotic manipulators with projection to future trends. *IEEE/ASME Trans. Mechatron.* **2017**, *22*, 669–680. [CrossRef]
18. Cao, X.; Aref, M.M.; Mattila, J. Design and Control of a Flexible Joint as a Hydraulic Series Elastic Actuator for Manipulation Applications. In Proceedings of the 2019 IEEE International Conference on Cybernetics and Intelligent Systems (CIS) and IEEE Conference on Robotics, Automation and Mechatronics (RAM), Bangkok, Thailand, 18–20 November 2019; pp. 553–558. [CrossRef]

19. Zhong, H.; Li, X.; Gao, L.; Dong, H. Position Control of Hydraulic Series Elastic Actuator with Parameter Self-Optimization. In Proceedings of the 2019 IEEE 4th International Conference on Advanced Robotics and Mechatronics (ICARM), Toyonaka, Japan, 3–5 July 2019; pp. 42–46. [CrossRef]
20. Zhong, H.; Li, X.; Gao, L. Adaptive Delay Compensation for Admittance Control of Hydraulic Series Elastic Actuator. In Proceedings of the 2020 IEEE 16th International Conference on Automation Science and Engineering (CASE), Hong Kong, China, 20–21 August 2020; pp. 384–389. [CrossRef]
21. Zhong, H.; Li, X.; Gao, L.; Dong, H. Development of Admittance Control Method with Parameter Self-optimization for Hydraulic Series Elastic Actuator. *Int. J. Control Autom. Syst.* **2021**, *19*, 2357–2372. [CrossRef]
22. Sciavicco, L.; Siciliano, B. *Modelling and Control of Robot Manipulators*; Springer Science & Business Media: London, UK, 2012. [CrossRef]
23. Kaixin, S.; Cong, Z.; YueHua, C.; Jing, W.; Qing, W.; HongXu, M. Impedance control of hydraulic series elastic actuation. In Proceedings of the 2020 Chinese Automation Congress (CAC), Shanghai, China, 6–8 November 2020; pp. 2393–2398. [CrossRef]
24. Dorf, R.C.; Bishop, R.H. *Modern Control Systems*; Pearson: Upper Saddle River, NJ, USA, 2011.
25. Mustalahti, P.; Mattila, J. Impedance Control of Hydraulic Series Elastic Actuator with a Model-Based Control Design. In Proceedings of the 2020 IEEE/ASME International Conference on Advanced Intelligent Mechatronics (AIM), Boston, MA, USA, 6–9 July 2020; pp. 966–971. [CrossRef]

PUBLICATION
VI

Impedance Control of Hydraulic Series Elastic Actuator with a Model-Based Control Design

P. Mustalahti and J. Mattila

In *2020 IEEE/ASME International Conference on Advanced Intelligent Mechatronics (AIM)*,
IEEE, Jul. 2020
DOI: 10.1109/AIM43001.2020.9158817

Impedance Control of Hydraulic Series Elastic Actuator with a Model-Based Control Design

Pauli Mustalahti and Jouni Mattila

Abstract— **Traditional mechanical actuators are designed with a high stiffness, which increases the system bandwidth. The operation of stiff actuator in uncertain environments is a challenging task due to physical interactions with the environment. Series elastic actuators (SEAs) have become the prominent method for decreasing stiffness between power output shafts and the environment in electric torque-controlled light arm applications. Compared to lightweight arms, the hydraulic actuated SEAs (HSEAs) can provide a much higher power-to-weight ratio. However, the control design for an HSEA is a challenging task due to the high non-linear dynamics of hydraulic systems. In this study, a novel subsystem-dynamics-based controller for an HSEA is designed using the virtual decomposition control (VDC) approach as a framework. The designed controller is incorporated as an inner-loop controller for previously designed a novel impedance controller. The one degrees-of-freedom (DOF) experimental setup is used to verify the control performance of the proposed controller.**

I. INTRODUCTION

In the future, the collaboration of humans and robots will become common in workplaces, homes, and service environments as the field of robotics rapidly advances. Human-robot collaboration requires safe, smooth control, and high-performing robots. One major challenge for the stable position control design is that in uncertain environments, the controller can be affected by unpredictable physical interactions with the environment. Therefore, force control is needed to handle environment dynamics in a closed-loop control.

Series elastic actuators (SEAs) have become a fundamental method in torque-controlled lightweight arm (LWA) in electric applications [1]–[4]. SEAs use a mechanical spring to decouple power output shafts from the environment. This provides force sensing, impact tolerance, and force fidelity for the mechanical actuator. SEAs have been used in different robot applications such as electric humanoid robots [5], [6] and walking robots [7]. Electric SEAs provide a rapid movement with a light load mass and actuator output power. Compared to electric SEAs, the HSEA systems provide a higher power-to-weight ratio and a lower speed ratio. The HSEA for light-duty manipulation is presented in [8], [9]. As presented in [8], the major challenges of the HSEAs in LWA are lack of back-driveability and a low maximum speed. Furthermore, creating a high performance control design for the HSEA systems is a challenging task due to significant nonlinearities of the hydraulic dynamics.

Impedance control for torque-controlled LWA is still an active research topic [10]–[14]. In [10], [14], the disturbance observer based impedance control is presented. In [11] the cascade control is used to decouple the slow outer-loop controller from the fast inner-loop dynamics. The control stability with different environments has been studied [12]. Control design for a linear electric actuator is presented in [15], where high motor voltage with drivetrain is used to produce continuous actuator force. In [16], the position-based impedance controller for the hydraulic drive unit of a legged robot is presented. The most of proposed impedance control methods are verified with torque-controlled LWA.

In this study, we investigated to study control for the HSEA targeted to heavy-duty applications with the payload of 200 kilos. As reported in [17], the nonlinear model-based control methods can provide high control performance with hydraulic manipulators. In previous studies [18]–[20], virtual decomposition control (VDC) shown to lead to state-of-the-art control performance with heavy-duty hydraulic manipulators. In this study, the main focus is to design model-based controller for the HSEA by exploiting the control design a principles of the VDC approach. The proposed controller is incorporated with a novel impedance controller [19].

The paper is organized as follows. First, in Section II the foundation of the VDC approach are presented. The kinematics and dynamics modeling of the HSEA in a view of VDC approach are presented in Section III. The corresponding control equations for the studied system are defined in Section IV. In Section V, the impedance controller for the HSEA is given. Finally, the experimental results are presented in a Section VI, and conclusions are given in Section VII.

II. MATHEMATICAL FOUNDATION

In this section, the necessary mathematical foundations of the VDC approach are introduced. Assume that there is an orthogonal three-dimensional coordinate frame $\{\mathbf{A}\}$ attached to the rigid body. Then, it follows from [21] that the linear/angular velocity vector in coordinate frame $\{\mathbf{A}\}$ can be defined as ${}^{\mathbf{A}}V = [{}^{\mathbf{A}}\mathbf{v} \;\; {}^{\mathbf{A}}\omega]^T$. In vector ${}^{\mathbf{A}}V$, ${}^{\mathbf{A}}\mathbf{v} \in \mathbb{R}^3$ denotes the linear velocity vector, and ${}^{\mathbf{A}}\omega \in \mathbb{R}^3$ denotes the angular velocity vector. Furthermore, the force/moment vector, in coordinate frame $\{\mathbf{A}\}$ can be written as ${}^{\mathbf{A}}F = [{}^{\mathbf{A}}\mathbf{f} \;\; {}^{\mathbf{A}}\mathbf{m}]^T$. In this vector, ${}^{\mathbf{A}}\mathbf{f} \in \mathbb{R}^3$ denotes the force vector and ${}^{\mathbf{A}}\mathbf{m} \in \mathbb{R}^3$ denotes the moment vector. For the two fixed successive frames $\{\mathbf{A}\}$ and $\{\mathbf{B}\}$, the following restrictions hold:

$${}^{\mathbf{B}}V = {}^{\mathbf{A}}\mathbf{U}_{\mathbf{B}}^{T}\,{}^{\mathbf{A}}V \tag{1}$$

$${}^{\mathbf{A}}F = {}^{\mathbf{A}}\mathbf{U}_{\mathbf{B}}\,{}^{\mathbf{B}}F, \tag{2}$$

where ${}^{\mathbf{A}}\mathbf{U}_{\mathbf{B}} \in \mathbb{R}^{6\times 6}$ denotes the force/moment transformation between two fixed coordinate frames.

Pauli Mustalahti and Jouni Mattila are with the Faculty of Engineering and Natural Sciences, Tampere University, Tampere, Finland. Emails: {pauli.mustalahti, jouni.mattila}@tuni.fi

In view of [21], the dynamics in coordinate frame $\{\mathbf{A}\}$ can be expressed as

$$ {}^{\mathbf{A}}F^{*} = \mathbf{M_A}\frac{d}{dt}({}^{\mathbf{A}}V) + \mathbf{C_A}({}^{\mathbf{A}}\omega){}^{\mathbf{A}}V + \mathbf{G_A} \tag{3} $$

where $\mathbf{M}_A \in \mathbb{R}^{6\times6}$ is the mass matrix, $\mathbf{C_A}({}^{\mathbf{A}}\omega) \in \mathbb{R}^{6\times6}$ represents the Coriolis and centrifugal terms, ${}^{\mathbf{A}}F^{*} \in \mathbb{R}^{6}$ is the net force/moment vector, and $\mathbf{G_A} \in \mathbb{R}^{6}$ is the gravity vector.

The linear parameterization expression for the required rigid body dynamics in a control design, can be written as

$$ \mathbf{Y_A}\boldsymbol{\theta}_\mathbf{A} \overset{\text{def}}{=} \mathbf{M_A}\frac{d}{dt}({}^{\mathbf{A}}V_{\text{r}}) + \mathbf{C_A}({}^{\mathbf{A}}\omega){}^{\mathbf{A}}V_{\text{r}} + \mathbf{G_A}. \tag{4} $$

In Eq. (4), the regressor matrix $\mathbf{Y}_A \in \mathbb{R}^{6\times13}$ and parameter vector $\boldsymbol{\theta}_\mathbf{A} \in \mathbb{R}^{13}$ are specified in [21].

Finally, the required net force/moment vector for the *rigid links* can be presented as

$$ {}^{\mathbf{A}}F_r^{*} = \mathbf{Y_A}\boldsymbol{\theta}_\mathbf{A} + K_\mathbf{A}({}^{\mathbf{A}}V_r - {}^{\mathbf{A}}V) \tag{5} $$

where $K_\mathbf{A}$ denotes the velocity feedback control gain.

III. KINEMATICS AND DYNAMICS MODEL FOR THE HSEA

In SEA actuators, the spring is used to decouple the actuator from the environment. Typically, the HSEA consists of a hydraulic cylinder, which is connected in a series with a spring and a control servo-valve. The one degrees-of-freedom (DOF) prototype for an HSEA is illustrated in Fig. 1, where the spring stiffness is designed to be symmetric in both directions. One method to estimate a cylinder force is to use chamber pressures and cylinder areas. Normally, the cylinder chamber pressures provide inaccurate estimation for the cylinder force due to noise of the signals. In contrast, in the HSEA, with the known spring stiffness and spring compression, the spring can be used as a force sensor. The spring placement between the output power shaft and the load enables to sensing of external forces from the load side.

In this study, the main focus is to design a model-based controller for the HSEA using the VDC approach as a framework. This approach provides a dynamics subsystem model-based control design method for complex robot systems [22]. The current state-of-the-art control performance of heavy-duty hydraulic manipulators has been reached with the VDC approach, as reported in [17]. The HSEA in Fig. 1 has studied in heavy-duty applications with a load mass up to 200 kg.

The three main steps of the VDC approach are virtual decomposition of the entire system, coordinate frame attachment to subsystems, and simple oriented graph (SOG) presentation. In this section, the main steps are presented in detail and then the kinematics and dynamics modeling for the HSEA in Fig. 1 are given.

A. Virtual Decomposition of the HSEA

First, the entire system needs to be virtually decomposed into subsystems by placing conceptual *virtual cutting points* (VCPs) in the studied system. VCP comprose directed separation points the between successive subsystems for the six-dimensional force/moment relation to these subsystems. A VCP is simultaneously interpreted driving for one subsystem and driven the VCP for another. The driven VCP is a point to which the force/moment vector is exerted, and the driving VCP is a point from which the force/moment vector is exerted. Virtual decomposition for the HSEA is expressed in Fig. 2b. As a results, the entire system can be modeled with two subsystem, which are called the *object* and *open chain*.

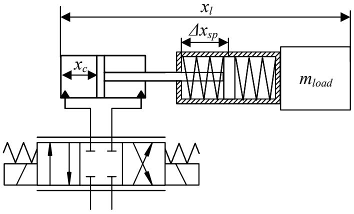

Fig. 1. Prototype for the HSEA

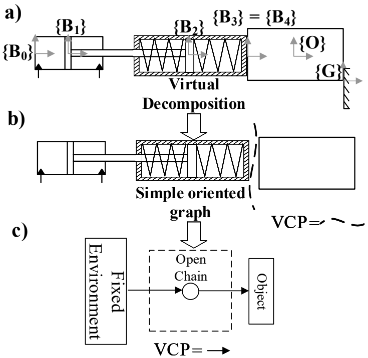

Fig. 2. Virtual decomposition of the HSEA

The dynamics between subsystems in a virtual decomposition system can be representing as an SOG [21]. The SOG represents the rigid links as nodes and the force/moment directions as directed edges. The SOG for the HSEA is given in Fig. 2c, where the subsystem of the hydraulic cylinder with a spring is represented by a dashed line.

The kinematic and dynamics of the subsystems can be modeled by allocating fixed coordinate frames to the subsystems. The used coordinate frames for the HSEA are presented in Fig. 2a. All coordinate frames in Fig. 2a are attached so that the z-axis point out from the paper. The frame $\mathbf{B}_0$ is fixed to cylinder base, $\mathbf{B}_1$ is fixed to cylinder piston, frame $\mathbf{B}_2$ is fixed to spring connecting point and $\mathbf{B}_3$ at the end of the cylinder. Frame $\mathbf{O}$ is fixed to load center of the mass and $\mathbf{G}$ at the end of the load.

B. Kinematics Equations for the HSEA

According to Eq. (1), the linear/angular velocity vectors in cylinder coordinate frames in Fig. 2a can be written as

$$ \begin{aligned} {}^{\mathbf{B}_1}V &= {}^{\mathbf{B}_0}\mathbf{U}_{\mathbf{B}_1}^{T}\,{}^{\mathbf{B}_0}V + \mathbf{z}\dot{x}_c & (6) \\ {}^{\mathbf{B}_2}V &= {}^{\mathbf{B}_1}\mathbf{U}_{\mathbf{B}_2}^{T}\,{}^{\mathbf{B}_1}V & (7) \\ {}^{\mathbf{B}_3}V &= {}^{\mathbf{B}_0}\mathbf{U}_{\mathbf{B}_3}^{T}\,{}^{\mathbf{B}_0}V + \mathbf{z}\dot{x}_l & (8) \end{aligned} $$

where $\mathbf{z} = [1\ 0\ 0\ 0\ 0\ 0]^T$, $\dot{x}_c$ is the cylinder piston velocity, and $\dot{x}_l$ is the load velocity. In Eq. (6), the linear/angular velocity vector ${}^{\mathbf{B}_0}V$ = $[0\ 0\ 0\ 0\ 0\ 0]^T$ because in this paper, the base frame position is fixed. As Fig. 2 demonstrates, the cylinder is connected in a series with spring. Therefore, the cylinder velocity can be calculated as

$$\dot{x}_c = \dot{x}_l + \dot{x}_{sp} \tag{9}$$

where $\dot{x}_l$ is the measured load velocity and $\dot{x}_{sp}$ is the spring velocity.

C. Kinematics of the Load

The kinematic model for the load object can be defined according to Eq. (1) and Fig. 2a as

$$ {}^{\mathbf{O}}V = {}^{\mathbf{B}_4}\mathbf{U}_{\mathbf{O}}^{T}\,{}^{\mathbf{B}_4}V = {}^{\mathbf{G}}\mathbf{U}_{\mathbf{O}}^{T}\,{}^{\mathbf{G}}V. \tag{10}$$

Velocity vector ${}^{\mathbf{G}}V$ describes the velocity of the object.

D. Dynamics of the Load Object

The load object force/moment vector can be written according to Eq. (3) as

$$ {}^{\mathbf{O}}F^{*} = \mathbf{M}_{\mathbf{O}}\frac{d}{dt}({}^{\mathbf{O}}V) + \mathbf{C}_{\mathbf{O}}({}^{\mathbf{O}}\omega){}^{\mathbf{O}}V + \mathbf{G}_{\mathbf{O}}. \tag{11}$$

On the other hand,

$$ {}^{\mathbf{O}}F^{*} = {}^{\mathbf{O}}\mathbf{U}_{\mathbf{B}_4}{}^{\mathbf{B}_4}F - {}^{\mathbf{O}}\mathbf{U}_{\mathbf{G}}{}^{\mathbf{G}}F \tag{12}$$

holds for the load object. Force vector ${}^{\mathbf{G}}F$ describes the external contact force between the object and environment.

E. Dynamics of the HSEA Open Chain

The dynamics relations for the HSEA *open chain* can be written, in view of Eq. 3, as

$$\begin{aligned}
{}^{\mathbf{B}_0}F^{*} &= \mathbf{M}_{\mathbf{B}_1}\frac{d}{dt}({}^{\mathbf{B}_1}V) + \mathbf{C}_{\mathbf{B}_1}({}^{\mathbf{B}_1}\omega){}^{\mathbf{B}_1}V + \mathbf{G}_{\mathbf{B}_1} && (13)\\
{}^{\mathbf{B}_1}F^{*} &= \mathbf{M}_{\mathbf{B}_2}\frac{d}{dt}({}^{\mathbf{B}_2}V) + \mathbf{C}_{\mathbf{B}_2}({}^{\mathbf{B}_2}\omega){}^{\mathbf{B}_2}V + \mathbf{G}_{\mathbf{B}_2} && (14)\\
{}^{\mathbf{B}_2}F^{*} &= \mathbf{M}_{\mathbf{B}_3}\frac{d}{dt}({}^{\mathbf{B}_3}V) + \mathbf{C}_{\mathbf{B}_3}({}^{\mathbf{B}_3}\omega){}^{\mathbf{B}_3}V + \mathbf{G}_{\mathbf{B}_3}. && (15)
\end{aligned}$$

Therefore, the total force/moment vectors in coordinate frames can be written as

$$\begin{aligned}
{}^{\mathbf{B}_2}F &= {}^{\mathbf{B}_2}F^{*} + {}^{\mathbf{B}_2}\mathbf{U}_{\mathbf{B}_3}{}^{\mathbf{B}_3}F && (16)\\
{}^{\mathbf{B}_1}F &= {}^{\mathbf{B}_1}F^{*} + {}^{\mathbf{B}_1}\mathbf{U}_{\mathbf{B}_2}{}^{\mathbf{B}_2}F && (17)\\
{}^{\mathbf{B}_0}F &= {}^{\mathbf{B}_0}F^{*} + {}^{\mathbf{B}_0}\mathbf{U}_{\mathbf{B}_1}{}^{\mathbf{B}_1}F. && (18)
\end{aligned}$$

Now, the hydraulic cylinder force in coordinate frame $\mathbf{B}_1$ can be presented from Eq. (17) as

$$ f_c = \mathbf{z}^{\mathbf{B}_1}F \tag{19}$$

where $\mathbf{z}$ = $[1\ 0\ 0\ 0\ 0\ 0]$.

IV. CONTROL EQUATIONS DESIGN FOR THE HSEA

Next, the control equations for the subsystems in Fig. 2b are presented. As Fig. 2 showed, the control system includes a hydraulic cylinder and a servo-valve. The control equations for the hydraulic servo-valve with fluid dynamics are specified closely in [18] and [21] with corresponding control equations. In view of the VDC approach, these modular equations can be incorporated into the control design when kinematics and dynamics equations are defined as in accordance with the approach. In the framework of the VDC, the format of required velocity includes the desired velocity and one or more terms, which are related to control errors. In the control design, control equations are designed by calculating required kinematics and dynamics equations in every coordinate frame in Fig. 2a.

A. Required Kinematics of the HSEA

The required linear/angular velocities for the HSEA *open chain* can be presented as follows, in view of Eqs. 6–8

$$\begin{aligned}
{}^{\mathbf{B}_1}V_r &= {}^{\mathbf{B}_0}\mathbf{U}_{\mathbf{B}_1}^{T}\,{}^{\mathbf{B}_0}V_r + \mathbf{z}\dot{x}_{cr} && (20)\\
{}^{\mathbf{B}_2}V_r &= {}^{\mathbf{B}_1}\mathbf{U}_{\mathbf{B}_2}^{T}\,{}^{\mathbf{B}_1}V_r && (21)\\
{}^{\mathbf{B}_3}V_r &= {}^{\mathbf{B}_0}\mathbf{U}_{\mathbf{B}_3}^{T}\,{}^{\mathbf{B}_0}V_r + \mathbf{z}\dot{x}_{lr} && (22)
\end{aligned}$$

where $\mathbf{z}$ = $[1\ 0\ 0\ 0\ 0\ 0]^T$, $\dot{x}_{lr}$ is the load velocity, and $\dot{x}_{cr}$ is the required cylinder piston velocity.

B. Required Kinematics of the Load

The load object's required kinematics can be specified, considering Eq. (10), as

$$ {}^{\mathbf{O}}V_r = {}^{\mathbf{B}_4}\mathbf{U}_{\mathbf{O}}^{T}\,{}^{\mathbf{B}_4}V_r = {}^{\mathbf{G}}\mathbf{U}_{\mathbf{O}}^{T}\,{}^{\mathbf{G}}V_r. \tag{23}$$

The velocity vector ${}^{\mathbf{G}}V_r$ describes the required velocity of the object.

C. Required Dynamics of the Load Object

The required net force/moment vector of the load object can be written, by reusing Eq. (5), as

$$ {}^{\mathbf{O}}F_r^{*} = \mathbf{Y}_{\mathbf{O}}\theta_{\mathbf{O}} + \mathbf{K}_{\mathbf{O}}({}^{\mathbf{O}}V_r - {}^{\mathbf{O}}V). \tag{24}$$

So, by using Eq. (12), the net force/moment vector in frame $\{\mathbf{B}_4\}$ can be presented as

$$ {}^{\mathbf{B}_4}F_r^{*} = {}^{\mathbf{B}_4}\mathbf{U}_{\mathbf{O}}{}^{\mathbf{B}_4}F_r - {}^{\mathbf{B}_4}\mathbf{U}_{\mathbf{G}}{}^{\mathbf{G}}F_r. \tag{25}$$

The force vector ${}^{\mathbf{G}}F_r$ describes the required external force vector between object and environment.

D. Required Dynamics of the HSEA

According to the required kinematics model for the HSEA *open chain* in Eqs. (20)–(22) and according Eq. (5), the required net force/moment vectors for rigid links can be defined as

$$\begin{aligned}
{}^{\mathbf{B}_0}F_r^{*} &= \mathbf{Y}_{\mathbf{B}_0}\theta_{\mathbf{B}_0} + \mathbf{K}_{\mathbf{B}_0}({}^{\mathbf{B}_0}V_r - {}^{\mathbf{B}_0}V) && (26)\\
{}^{\mathbf{B}_1}F_r^{*} &= \mathbf{Y}_{\mathbf{B}_1}\theta_{\mathbf{B}_1} + \mathbf{K}_{\mathbf{B}_1}({}^{\mathbf{B}_1}V_r - {}^{\mathbf{B}_1}V) && (27)\\
{}^{\mathbf{B}_2}F_r^{*} &= \mathbf{Y}_{\mathbf{B}_2}\theta_{\mathbf{B}_2} + \mathbf{K}_{\mathbf{B}_2}({}^{\mathbf{B}_2}V_r - {}^{\mathbf{B}_2}V). && (28)
\end{aligned}$$

Then, it follows from Eqs. (5), (26), and (28) that the force/moment vectors for the HSEA *open chain* can be defined as

$$\begin{aligned} {}^{\mathbf{B}_2}F_r &= {}^{\mathbf{B}_2}F_r^* + {}^{\mathbf{B}_2}\mathbf{U}_{\mathbf{B}_3}{}^{\mathbf{B}_3}F_r && (29) \\ {}^{\mathbf{B}_1}F_r &= {}^{\mathbf{B}_1}F_r^* + {}^{\mathbf{B}_1}\mathbf{U}_{\mathbf{B}_2}{}^{\mathbf{B}_2}F_r && (30) \\ {}^{\mathbf{B}_0}F_r &= {}^{\mathbf{B}_0}F_r^* + {}^{\mathbf{B}_0}\mathbf{U}_{\mathbf{B}_1}{}^{\mathbf{B}_1}F_r. && (31) \end{aligned}$$

Finally, the required linear cylinder force can be calculated from Eq. (30)

$$f_{cr} = \mathbf{z}^{\mathbf{B}_1}F_r \tag{32}$$

where $\mathbf{z}$ = [1 0 0 0 0 0].

V. IMPEDANCE CONTROLLER FOR THE HSEA

HSEA actuators provide a high power-to-weight ratio compared to electric SEAs. Therefore, HSEAs are suitable for moving heavy loads in many industrial tasks. Interactions between the environment and manipulator with a high contact force may stress mechanical structure. For this reason, the impedance control designs for HSEAs have been an active research subject over the past decade. A novel impedance control method in a Cartesian space for heavy-duty hydraulic manipulators the framework of the VDC approach is presented in [23]. In this study, the impedance control method is incorporated in the control design.

Fig. 1 shows that the HSEA consists of a spring, which is connected in the series with a hydraulic spring. By connecting two elastic springs in a series, the effective stiffness of the system is reduced. In this study, the selected spring stiffness is illustrated in Fig. 3. As Fig. 3 shows, the spring stiffness is not linear due to pretension of the spring. The selection of the spring is presented with more details in [24]. The contact force of the HSEA can be estimated by using spring stiffness and measured spring compression. Therefore, the contact force can be calculated as

$$\begin{aligned} & f_e = \eta(x_{sp})(\eta(x_{pr-x_{sp}})\eta(x_{sp})k_1x_{sp}+ \\ & \eta(x_{sp}-x_{pr})k_2+2k_1)-\eta((-x_{sp})(\eta(x_{pr}+x_{sp}) \\ & \eta(-x_{sp})k_1(-x_{sp})+\eta(-x_{sp}-x_pr)k_2+2k_1) \qquad (33) \end{aligned}$$

where k_1 and k_2 are the slope gains for the spring stiffness, x_{pr} is a pretension area, x_{sp} is the spring compression, and f_e is a contact force. The switching function is

$$\eta(x) = \frac{\tanh([x-x_o]/c_\eta)+1}{2} \tag{34}$$

where x_o is a sufficiently small offset constant parameter, and c_η is a sufficiently small constant.

Now, the control law for a target impedance can be presented, in view of [25], as

$$f_d - f_e = M_d(\ddot{x}_l - \ddot{x}_{ld}) + K_d(\dot{x}_l - \dot{x}_{dl}) + K_x(x_l - x_{dl}) \tag{35}$$

where M_d is inertia gain, K_d is the damping gain, and K_x is the stiffness gain of the target impedance. In this study, the dynamics parameters M_d, K_d and K_x are scalars because only 1-DOF contact force is studied. In Eq. (35), x_l, $\dot{x}_l$ and $\ddot{x}_l$ represent the measured position, velocity, and acceleration of the load, and x_{dl}, $\dot{x}_{dl}$ and $\ddot{x}_{dl}$ are the desired values respectively. In Eq. (35) the desired force is selected to be $f_d = 0$. The dynamics of the environment can be modeled as pure damping and stiffness to make the model manageable for the control. Now, the impedance control law can be rewritten as

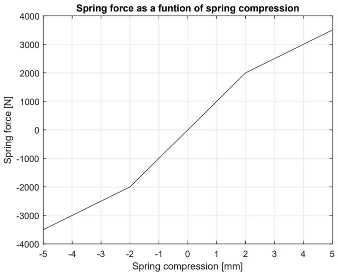

Fig. 3. Spring force as a function of spring compression

$$f_d - f_e = K_d(\dot{x}_l - \dot{x}_{dl}) + K_x(x_l - x_{dl}). \tag{36}$$

As specified in [23], by assuming that a stiffness and a damping gain are selected so that their magnitudes are not subject to unstable behavior and that desired target impedance is attainable, the impedance control law in Eq. (36) can be rewritten as

$$\dot{x}_r = \dot{x}_{dl} + D_x(x_{dl} - x_l) + D_d(f_d - f_e) \tag{37}$$

where $\dot{x}_r$ is a required velocity, D_x is a stiffness gain, and D_d is a damping gain. The required velocity $\dot{x}_r$ is a unique property of the VDC approach, which generally consists of a desired velocity and control error related terms. The required velocity serves as a reference trajectory to the system. In Eq. (37), the D_x and D_d are scalar gains, which are defined as

$$\begin{aligned} D_d &= K_d^{-1} && (38) \\ D_x &= K_xK_d^{-1}. && (39) \end{aligned}$$

The impedance control law in Eq. (37) is equal to Eq. (36) only if gains D_x and D_d are defined as in Eqs. (38)–(39) more detail in [26]. As Eq. (37) shows, this impedance control method provides a parallel force and position control.

Now, velocity vectors in Eq. (10) and Eq. (23) and force vectors in Eq. (12) and Eq. (25) in coordinate frame $\mathbf{G}$ (see Fig. 2a) can be defined as

$$\begin{aligned} {}^{\mathbf{G}}V = \mathbf{z}\dot{x}_l \quad {}^{\mathbf{G}}V_r = \mathbf{z}\dot{x}_r && (40) \\ {}^{\mathbf{G}}F = \mathbf{z}f_e \quad {}^{\mathbf{G}}F_r = \mathbf{z}f_r. && (41) \end{aligned}$$

where $\mathbf{z}$ = $[1\ 0\ 0\ 0\ 0\ 0]^T$.

VI. EXPERIMENTAL RESULTS

In this section, the control of the proposed controller was verified with a 1-DOF full-scale experimental setup, which is presented in Fig. 4. In the setup, the real-time control interface was implemented with a Beckhoff CX2030 controller with a sampling rate of 1000 Hz. The size of the hydraulic cylinder was ϕ32/18-400. The cylinder was

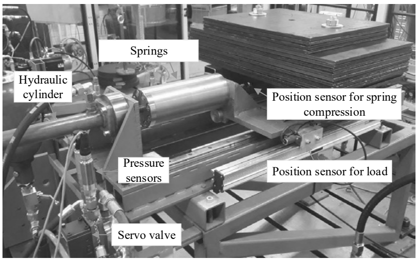

Fig. 4. 1-DOF HSEA experimental setup

controlled by using an NG6 size servo solenoid valve with a nominal flow rate of 40 l/min at 3.5 MPa per control notch. The cylinder chamber pressures were measured with UNIK 5000 pressure transmitters with a measuring range of 25 MPa. The supply pressure of the setup was set to 20 MPa. The spring compression was measured using an MTS linear position sensor with a measurement range of 0.015 m and load position was measured with a Heidenhein linear position sensor with a measurement range of a 0.54 m. The used load mass was 200 kg. The used spring stiffness (see. Fig.3) was 1000 N/mm in pretension area and 500 N/mm after that.

In both experiments, the proposed controller was tested by using a point-to-point quintic reference trajectory designed for the load position. The damping and the stiffness gains of the impedance control (see Eq. (37)) were set as a compromise between a system damping and a settling time. In the experiments, gains in Eq. (38) and Eq. (39) was set to $D_x = 5 \times 10^{-5}$ and $D_d = 1.75$.

In the first experiment, the load was driven to contact with a stiff environment. The load position during the contact motion is presented in Fig. 5. The contact point in Fig. 5 was set to 0.496 m, which was reached 4 s. As Fig. 5 shows, the proposed controller efficiently limits the load position in a contact motion. The load position errors without contact are about 1.4 mm and 1.8 mm for the positive and negative directions, respectively. Contact with the environment caused a peak for the position error, and the static error during contact was 1.5 mm. The static error contact force results from a parallel force and position control. Fig. 6, the cylinder position during the contact motion is presented. As Fig. 6 demonstrates, the maximum position error of the hydraulic cylinder for position direction is about 1.2 mm , and for the negative direction it is about 1.6 mm.

As Eq. (37) shows, in the case of the proposed impedance controller, the contact force is included to load the velocity reference with a position error term. In Fig. 7, the contact force effects to the load velocity reference are presented. As Fig. 7 shows, the contact at time 4 s efficiently drops the load reference velocity when the contact force and position error start to rise.

In both experiments, the contact force was estimated using Eq. (33). Fig. 8 demonstrates, the contact force with and without the proposed impedance controller. As Fig. 8 shows, the proposed impedance controller significantly decreases the actuator's contact force with the environment.

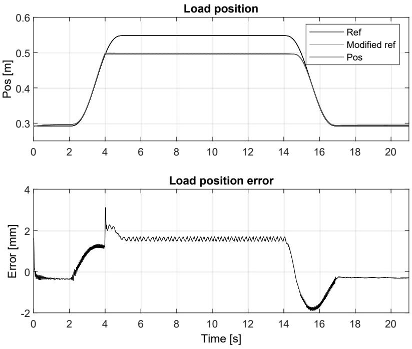

Fig. 5. Load position during the contact motion with stiff environment

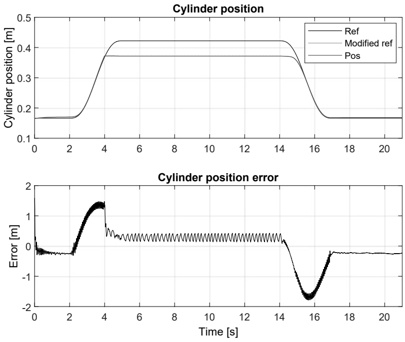

Fig. 6. Cylinder position during the contact motion with stiff environment

In the second experiment, the load was put into contact with a soft environment. The load position during the contact motion is presented in Fig. 9. The contact point in Fig. 9 was set to 0.466 m, which was reached at time 3.8 s. Compared to Fig. 5, which represents a stiff environment, in Fig. 9 with the soft environment the static error is a litter higher. Still, the proposed controller can be limited efficiently by the load position during the contact motion.

The experimental results verifies that proposed impedance control method can efficiently damps the contact between the HSEA system and stiff and soft environment.

VII. CONCLUSIONS

This paper focused on proposing a model-based controller design for HSEAs. The target impedance control for an HSEA is also presented by incorporating the proposed controller as an inner-loop controller with a previously designed impedance control method. Experimental results with a real-size 1-DOF experimental setup verified that the proposed controller can efficiently control the contact force between the actuator and the environment. In future research, the proposed controller will be studied in a real world multi-DOF hydraulic manipulator.

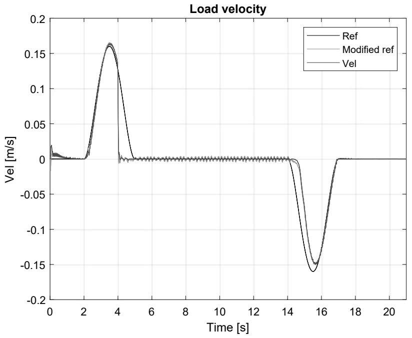

Fig. 7. Load velocity during the contact motion with stiff environment

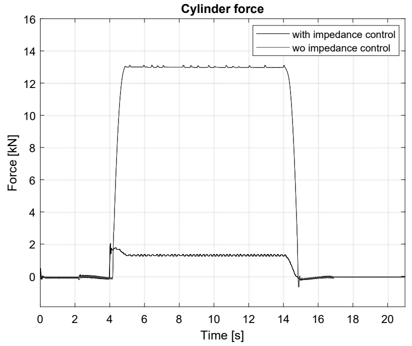

Fig. 8. Cylinder force with and without impedance control

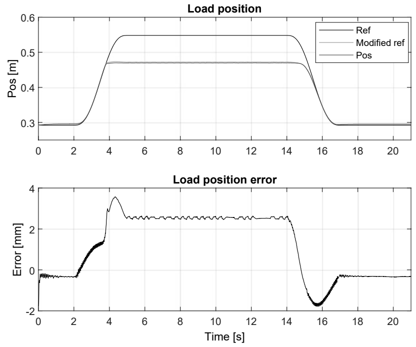

Fig. 9. Load position during the contact motion with soft environment

REFERENCES

[1] A. Albu-Schäffer, C. Ott, and G. Hirzinger, "A unified passivity-based control framework for position, torque and impedance control of flexible joint robots," *The international journal of robotics research*, vol. 26, no. 1, pp. 23–39, 2007.

[2] C. Loughlin, A. Albu-Schäffer, S. Haddadin, C. Ott, A. Stemmer, T. Wimböck, and G. Hirzinger, "The dlr lightweight robot: design and control concepts for robots in human environments," *Industrial Robot: an international journal*, 2007.

[3] A. Albu-Schaffer, C. Ott, U. Frese, and G. Hirzinger, "Cartesian impedance control of redundant robots: Recent results with the dlr-light-weight-arms," in *International Conference on Robotics and Automation*, vol. 3. IEEE, 2003, pp. 3704–3709.

[4] C. Lee, S. Kwak, J. Kwak, and S. Oh, "Generalization of series elastic actuator configurations and dynamic behavior comparison," in *Actuators*, vol. 6, no. 3. Multidisciplinary Digital Publishing Institute, 2017, p. 26.

[5] B. Lee, C. Knabe, V. Orekhov, and D. Hong, "Design of a human-like range of motion hip joint for humanoid robots," in *International Design Engineering Technical Conferences and Computers and Information in Engineering Conference*. ASME, 2014.

[6] W. Takano, H. Kanayama, T. Takahashi, T. Moridaira, and Y. Nakamura, "A data-driven approach to probabilistic impedance control for humanoid robots," *Robotics and Autonomous Systems*, vol. 124, p. 103353, 2020.

[7] D. W. Robinson, J. E. Pratt, D. J. Paluska, and G. A. Pratt, "Series elastic actuator development for a biomimetic walking robot," in *International Conference on Advanced Intelligent Mechatronics*. IEEE, 1999, pp. 561–568.

[8] J. Pratt, B. Krupp, and C. Morse, "Series elastic actuators for high fidelity force control," *Ind. Robot: An International Journal*, 2002.

[9] J. E. Pratt and B. T. Krupp, "Series elastic actuators for legged robots," in *Unmanned Ground Vehicle Technology Vi*, vol. 5422. International Society for Optics and Photonics, 2004, pp. 135–144.

[10] S. Oh and K. Kong, "High-precision robust force control of a series elastic actuator," *IEEE/ASME Trans. on Mechatronics*, vol. 22, no. 1, pp. 71–80, 2016.

[11] Y. Zhao, N. Paine, S. J. Jorgensen, and L. Sentis, "Impedance control and performance measure of series elastic actuators," *IEEE Trans. on Industrial Electronics*, vol. 65, no. 3, pp. 2817–2827, 2017.

[12] A. Calanca and P. Fiorini, "Understanding environment-adaptive force control of series elastic actuators," *IEEE/ASME Trans. on Mechatronics*, vol. 23, no. 1, pp. 413–423, 2018.

[13] D. W. Robinson and G. A. Pratt, "Force controllable hydro-elastic actuator," in *Proceedings 2000 ICRA. Millennium Conference. IEEE International Conference on Robotics and Automation.*, vol. 2. IEEE, 2000, pp. 1321–1327.

[14] A. Flores-Abad, M. Nandayapa, and M. A. Garcia-Teran, "Force sensorless impedance control for a space robot to capture a satellite for on-orbit servicing," in *Aerospace Conference*.

[15] N. Paine, S. Oh, and L. Sentis, "Design and control considerations for high-performance series elastic actuators," *IEEE/ASME Trans. on Mechatronics*, vol. 19, no. 3, pp. 1080–1091, 2013.

[16] K.-x. Ba, G.-l. Ma, B. Yu, Z.-g. Jin, Z.-p. Huang, J.-x. Zhang, and X.-d. Kong, "A nonlinear model-based variable impedance parameters control for position-based impedance control system of hydraulic drive unit," *Int. Journal of Control, Automation and Systems*, pp. 1–12.

[17] J. Mattila, J. Koivumäki, D. G. Caldwell, and C. Semini, "A survey on control of hydraulic robotic manipulators with projection to future trends," *IEEE/ASME Trans. on Mech.*, vol. 22, no. 2, pp. 669–680, 2017.

[18] J. Koivumäki and J. Mattila, "Stability-guaranteed force-sensorless contact force/motion control of heavy-duty hydraulic manipulators," *IEEE Trans. Robotics*, vol. 31, no. 4, pp. 918–935, 2015.

[19] ——, "Stability-guaranteed impedance control of hydraulic robotic manipulators," *IEEE/ASME Trans. on Mechatronics*, vol. 22, no. 2, pp. 601–612, 2017.

[20] J. Koivumäki, W.-H. Zhu, and J. Mattila, "Energy-efficient and high-precision control of hydraulic robots," *Control Engineering Practice*, vol. 85, pp. 176–193, 2019.

[21] W.-H. Zhu, *Virtual decomposition control: toward hyper degrees of freedom robots*. Springer Science & Business Media, 2010, vol. 60.

[22] W.-H. Zhu, Y.-G. Xi, Z.-J. Zhang, Z. Bien, and J. De Schutter, "Virtual decomposition based control for generalized high dimensional robotic systems with complicated structure," *IEEE Trans. Robot. Autom.*, vol. 13, no. 3, pp. 411–436, 1997.

[23] J. Koivumäki and J. Mattila, "Stability-guaranteed impedance control of hydraulic robotic manipulators," *IEEE/ASME Trans. Mechatronics*, vol. 22, no. 2, pp. 601–612, 2017.

[24] X. Cao, M. M. Aref, and J. Mattila, "Design and control of a flexible joint as a hydraulic series elastic actuator for manipulator application," 2019, [Accepted].

[25] H. Neville, "Impedance control: An approach to manipulation: Part i–iii," *Trans. of ASME Journal of Dynamic System, Measurement, and Control*, vol. 107, p. 1, 1985.

[26] J. Koivumäki and J. Mattila, "Adaptive and nonlinear control of discharge pressure for variable displacement axial piston pumps," *ASME J. Dyn. Syst., Meas., Control*, vol. 139, no. 10, 2017.